CALIBRATING NMR RESPONSE TO CAPILLARY PRESSURE CURVES IN FINE GRAINED LITHOLOGIES: PRETTY HILL FORMATION, OTWAY BASIN

Thesis submitted for the degree of
Master of Science
(Petroleum Geology & Geophysics)

ALI AL-GHAMDI

Australian School of Petroleum,
The University of Adelaide

August 2006

Statement of Authenticity

I declare that this thesis does not incorporate without acknowledgement any material previously submitted for a degree or diploma in any university; and that to the best of my knowledge it does not contain any materials previously published or written by another person except where due reference is made in the text.

I give consent to this copy of my thesis, when deposited in the University Library, being made available for loan and photocopying, subject to the provisions of the Copyright Act 1968.

Ali Al-Ghamdi

August 2006

ABSTRACT

Nuclear magnetic resonance (NMR) tools are commonly used in formation evaluation. NMR T2 distribution data have been used by previous authors to build down-hole pseudo capillary pressure curves in reservoir quality rocks. The objective of this study is to generate NMR-derived down-hole pseudo capillary pressure curves in very fine grained lithologies in order to determine whether it is possible to estimate capillary displacement pressures and thereby sealing capacity.

NMR T2 relaxation time distributions of flood plain facies at Redman-1 well in Otway Basin, SE of South Australia, were converted to pseudo capillary pressure curves. The generated curves were compared to mercury injection capillary pressure (MICP) curves. The petrophysical properties and mineralogy of 11 flood plain samples were analyzed using the following measurement techniques: MICP, Scanning Electron Microscopy (SEM), core porosity and permeability, X-Ray Diffraction (XRD), optical microscopy of thin section and X-Ray Fluorescence XRF.

Displacement pressures were calculated from pseudo capillary pressure curves and compared with actual MICP curves at different saturations percentages of non-wetting phase. The best percentage in displacement pressure estimation is the 20% saturation with correlation coefficient of 0.59. Statistically, the correlation coefficient of the 20% saturation is too low for meaningful calibration.

The reason for the lack of robust calibration is related to the actual properties of the rock: the Redman-1 flood plain samples have high iron contents (Fe2O3 content ranges between 5.21-7.16 wt%) with correspondingly increased magnetic susceptibility and elevated internal field gradients. The iron is mainly associated with chlorite and biotite in the samples studied. The NMR T2 response is affected significantly by the internal magnetic field gradient which depends on the magnitude of the

magnetic susceptibility. Surface relaxivity changes and high pore to throat size ratio also contribute to the difference between the two measurements.

Study conclusions are that T2 response in high iron content rock is affected by many factors such as magnetic susceptibility, surface relaxivity and aspect ratio. Therefore, using the NMR response to estimate capillary displacement pressures in iron-rich, fine grained rocks is not recommended. However, further studies in rocks of low magnetic susceptibility might yield more significant correlations.

TABLE OF CONTENTS

Acknowledgments

I would like to acknowledge;

- Saudi Aramco for sponsoring my M.Sc. studies.
- Origin Energy and PIRSA for access to log and core data.
- My supervisors: Professor John Kaldi (ASP), Dr. Peter Boult (PIRSA) and Dr. Peter Tingate (ASP).
- Staff and student at Australian School of Petroleum for their assistance, in particular, Dr. Ric Daniel.

Finally, I would like to thank my wife and family for their constant support during my studies.

CHAPTER 1
INTRODUCTION

1.1 Background

Nuclear magnetic resonance (NMR) is an important tool in formation evaluation for measuring lithology-independent porosity and estimating permeability. It is also a hydrocarbon identification tool. The NMR T2 distribution is approximately equivalent to a pore size distribution which is acquired every ≈15.2cm (6in). The T2 distribution curve has been converted to a continuous down-hole pseudo capillary pressure curve to delineate reservoir rocks in many previous studies. The down-hole pseudo capillary pressure curve can be used to estimate height above free water level, water saturation and displacement pressure. This is very important information for reservoir development. Also, the pattern of T2 used for facies distribution.

Mercury injection capillary pressure (MICP) measurement is used in seal evaluation to identify the pressure required to displace the wetting phase, and to determine pore throat size. Sealing capacity can be calculated from the displacement pressure in seal and reservoirs samples and also the fluid properties. MICP measurements are commonly obtained on scattered core and cutting samples which might not truly represent the different vertical facies. In addition, clay rich samples are subject to fracturing and alteration from their *in situ* conditions when brought to surface and stored, which makes MICP analysis difficult.

Reservoir pseudo capillary pressure (Pc) curves have been derived from NMR response successfully in many previous studies (e.g. Marschall et al, 1995; Lowden et al, 1998; Boult et al, 1999; Glorioso et al, 2003). NMR pseudo Pc curves were derived by calibrating the NMR T2 distribution to laboratory capillary pressure data in reservoir intervals. In Redman-1, cumulative T2 relaxation curves have been calibrated to capillary pressure

curves from core analysis of the Pretty Hill Sandstone reservoir (Boult et al., 1999). A good displacement pressure (Pd) estimation from the T2 distribution was reached by applying the appropriate effective surface relaxivity (ρe) factor (Figure 2.9). This technique enables direct water saturation calculation from the NMR log given height above free water level (FWL) determination.

The work by Boult et al (1999) did not include the fine grained (seal) lithology intervals. This study investigates the possibility of estimating displacement pressure (Pd) via pseudo capillary pressure curves derived from seal lithologies. If displacement pressure (Pd) can be estimated from T2 distribution in seal lithologies, the need for acquiring MICP measurements will be minimized. Moreover, seal capacity measurement will be available for the entire seal interval with a vertical resolution of a few inches.

If this methodology could be applied successfully in fine grained rocks, a continuous pseudo capillary pressure curve at every ≈15.2cm (6in) could be obtained over seal intervals. Also, measurements could be made at in *situ conditions* and the extra cost for laboratory measurement could be avoided when data from the NMR tool are available.

1.2 Project Aims

The main aim of this project was to use the Redman-1 core to undertake a detailed assessment of whether NMR T2 data could be used for estimating displacement pressures from down-hole pseudo capillary pressure curves in siliciclastic seal lithologies. This has been achieved by calibrating the NMR T2 distribution with actual mercury injection capillary pressure (MICP) curves in porous reservoir intervals in previous studies (e.g., Boult et al., 1999; Glorioso et al., 2003). A similar methodology was applied to intervals which have small pores to investigate how the NMR T2 distribution behaves between very small pores and to determine if it can be used to determine pore throat size accurately.

The calibration aimed to give a better understanding of the behavior of T2 distribution in very fine lithologies, and how it can be applied to estimate capillary pressure. Moreover, if the calibration was adequate in estimating the displacement pressure, it could then be applied to evaluating seal capacities in such rocks as the Laira Formation, whose lowermost section comprises a floodplain shale facies.

The main study tasks were to;

- generate pseudo capillary pressure from T2 distribution in very fine grained lithologies;
- calibrate NMR T2 pseudo capillary pressure curves with actual laboratory MICP curves;
- examine the accuracy of the estimated capillary pressure from T2 pseudo capillary pressure in a micro-pore system.

- understand the contribution of clay bound water to NMR response in fine grained lithologies and how far the calibration could account for the difference between the two measurements.
- identify the effect of mineralogy and clay types on T2 behavior in flood plain facies.

1.3 Structure of the Thesis

The thesis starts with an introduction to the NMR tool and the theory of pore size measurements. Then, a description is given of the different laboratory measurements used to identify the petrophysical and mineralogical characteristics of the Redman-1 samples. Chapter Four presents the petrology of the Redman-1 core using different techniques such as core descriptions, thin sections, XRD and XRF analyses. Petrophysical properties and the methodology of obtaining pseudo capillary pressure curves for the fine grained samples is described in Chapter Five. The calibration between the two measurements, NMR T2 and MICP curves, is presented with an interpretation of statistical confidence. The different factors which might affect the NMR response in such a lithology are discussed in the following chapter. Finally, conclusions from this study and recommendations for further investigations using NMR are presented.

CHAPTER TWO
NMR, CAPILLARITY AND GEOLOGICAL REVIEW

2.1 NMR Principles

The principle of the nuclear magnetic resonance (NMR) tool is based on measurements of the relaxation of pore fluids to provide formation evaluation and petrophysical data including porosity, irreducible water saturation, permeability and pore-size distributions (Coates et al., 1999). NMR measurements record the behavior of hydrogen protons in the pore space of the formation. Thus, fluids containing hydrogen (water, oil and gas) are visible to the tool; the latest generation of NMR tools can even detect the hydrogen protons on clay surfaces. NMR porosity measurement does not include the hydrogen which is part of the matrix composition of the rock; therefore it provides a lithology and clay-independent total porosity value.

Nuclear magnetic resonance (NMR) signals from hydrogen protons were discovered in 1946 by Purcell and Bloch (Kenyon et al, 1995) and in the 1950s were recognized by the oil and gas industry as a potential tool in formation evaluation. In the late 1950s, NMR measurements became developed further to provide information on formation pore fluids and pore structure (Allen et al, 2000). The first NMR log was run in 1960, measuring the signal from protons precessing (spinning) in the Earth's magnetic field (Brown and Gamson, 1960).

More advances in NMR measurements and interpretation occurred in the 1960s and late 1970s, including:

- the development of a relationship between relaxation time and permeability of sandstones developed by Seevers (1966),

- the concept of a free fluid index and new methods to measure permeability using NMR introduced by Timur (1968), and
- the relationship between pore size, fluid and matrix was introduced in 1969 by Loren and Robinson (Kenyon et al, 1995).

Now, NMR can give information, not only on the saturation of fluids in the rocks, but also on the pore size distributions of different rock types (Coates et al., 1999).

2.1.1 Physics of Nuclear Magnetic Resonance

NMR measurement uses a static magnetic field to polarize the hydrogen protons that are randomly oriented in the formation fluids. The constant magnetic field (Bo) of the tool aligns or polarizes the spin axes of the protons in the longitudinal direction which is the direction of B_0 (Fig 2.1 A). Then an oscillating magnetic field, B_1, is applied to tip the proton spin axes to 90° of the transverse plane, perpendicular to longitudinal direction. When the oscillating field is subsequently removed, the protons begin dephasing and tipping back, or relaxing, toward their equilibrium position, parallel to B_0 direction (Fig 2.1 B), aligned to the initial static magnetic field (Kenyon et al, 1995). Dephasing time for protons to return to the initial or longitudinal direction called longitudinal relaxation (T1).

Thus, the net magnetization decreases as the dephasing progresses. The tool measures radiofrequency quantity, which protons radiate during relaxation process, in the transverse direction as a decaying T2 signal. This signal is called a spin echo. 180° pulse sequences are used repeatedly to generate a series of so-called spin-echo trains. The entire pulse sequence, which is composed of 90° pulse and followed by long series of 180° pulses (Figure 2.1 C-F), is called a CPMG sequence (after its inventors Carr, Purcell, Meiboom, and Gill). CPMG sequences increase strength of the

radiofrequency decay in order to minimize noise contribution to the signal. The decay in amplitude of the spin-echo train is recorded versus time and forms the raw NMR data (Figure 2.2).

The number of hydrogen nuclei associated with the fluids in the pores within the sensitive volume is proportional to the initial amplitude of the spin-echo train. Thus, this initial amplitude is calibrated to give porosity. The accuracy of the raw reported porosity depends on a sufficiently long polarization time (TW) to achieve complete polarization and a sufficiently short inter-echo spacing (TE) to record the decays from extremely small pores (clay pores). TE is the time between the individual echoes in an echo train whereas TW is the time between the end of the measurement of one echo train and the beginning of the next echo train. Both the inter-echo spacing and polarization time can be adjusted to vary the resolution content of the acquired data.

There are some properties of the pore fluids that may affect the echo trains. Those properties are the hydrogen index (HI), which is the density of hydrogen atoms in the fluid; the longitudinal relaxation time (T_1), which is an indication of the longitudinal relaxation speed of aligned proton in the fluids; transverse relaxation time (T_2), which is an indication of the transversely oriented relaxation speed of aligned proton in the fluids; and diffusivity (D) which is a measure of the extent to which molecules move at random in the fluid (Kenyon et al, 1995).

2.1.2 NMR T2 Distribution

The amplitude of the spin-echo train decay can be calculated accurately by the sum of decaying exponentials, each of them with a different decay constant. The set of all the decay constants forms the decay spectrum or transverse-relaxation-time (T_2) distribution. The spin-echo train decay data

can be converted to a T_2 distribution using the mathematical process of inversion.

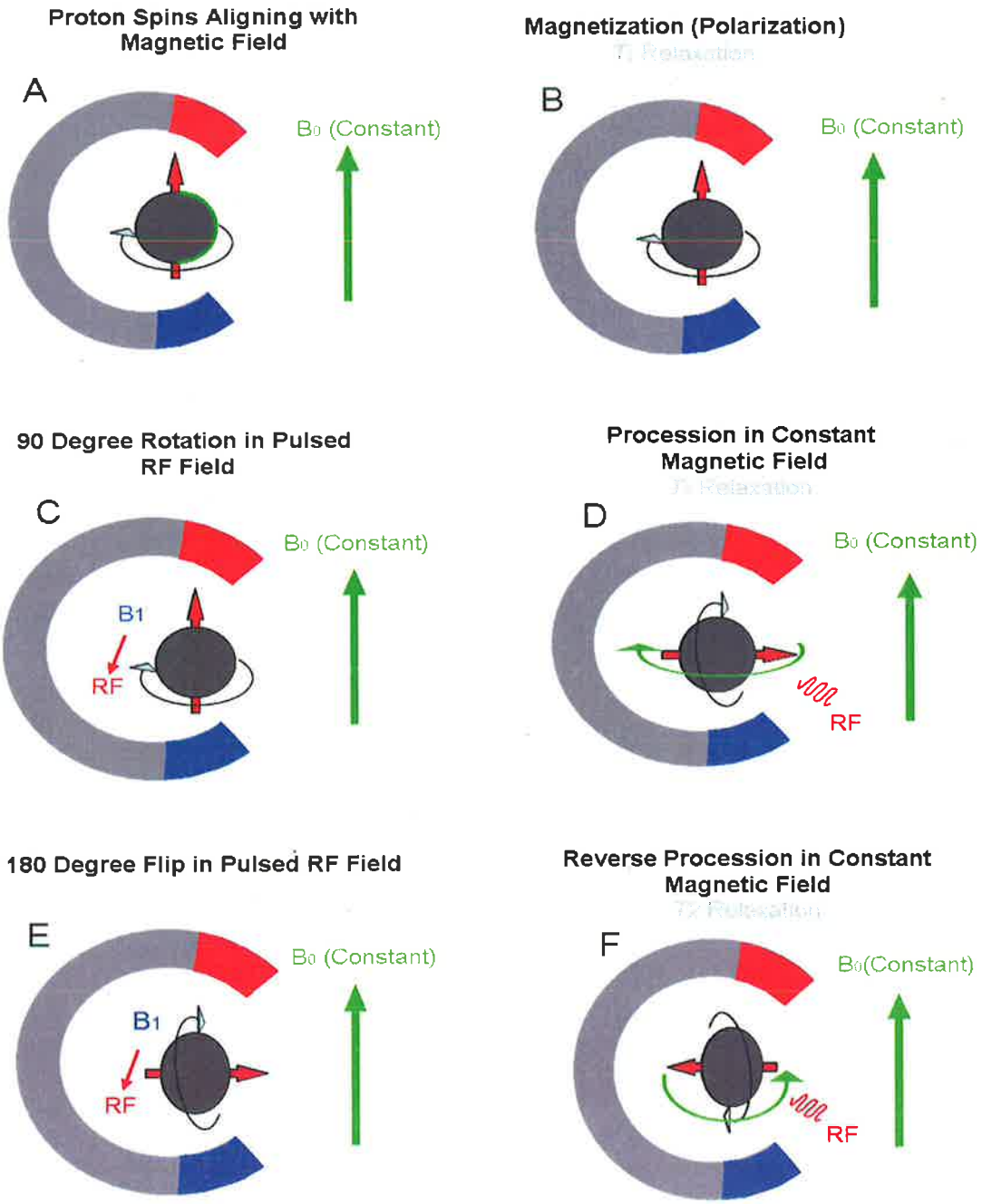

Figure 2.1 Demonstration of transverse plane and how spins are manipulated to acquire relaxation time. A and B are the process to obtain the longitudinal relaxation (T1), where C to F show the process in CPMG process to manipulate hydrogen nuclei in order to get T2 and minimize the B_0 effect.

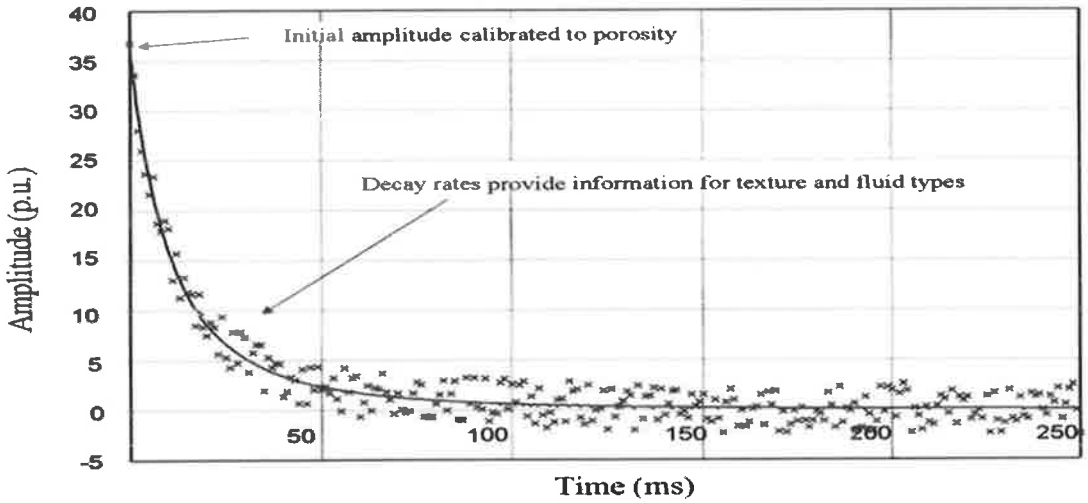

Figure 2.2 Typical decay of a spin echo train illustrated as porosity unit (p.u) in Y axis versus time (m.s) in X axis (modified from Coates et al, 1999).

Although calibration adjustments are necessary, the porosity can be related to the area under the T_2 distribution curve. In water-saturated rocks, it can be proven mathematically that the decay curve associated with a single pore will be a single exponent with a decay constant proportional to pore size; that is, small pores have small T_2 values and large pores have large T_2 values (Brownstein and Tarr, 1979; Kenyon, 1992).

Figure 2.3 shows the T_2 distribution that was derived from the spin-echo train in Figure 2.2. Rock samples will have a distribution of pore sizes at any depth in the well-bore; hence, the multi-exponential decay represents the distribution of pore sizes at that depth, with each T_2 value corresponding to a different pore size (Figure 2.4).

2.1.3 Relaxation Mechanisms

One of the most important requirements for the proper application of NMR in formation evaluation is to understand the nature of NMR relaxation of fluids in rock pores. The values of T1 and T2 are affected by the physical and chemical properties of the fluids, the uniformity of the static magnetic

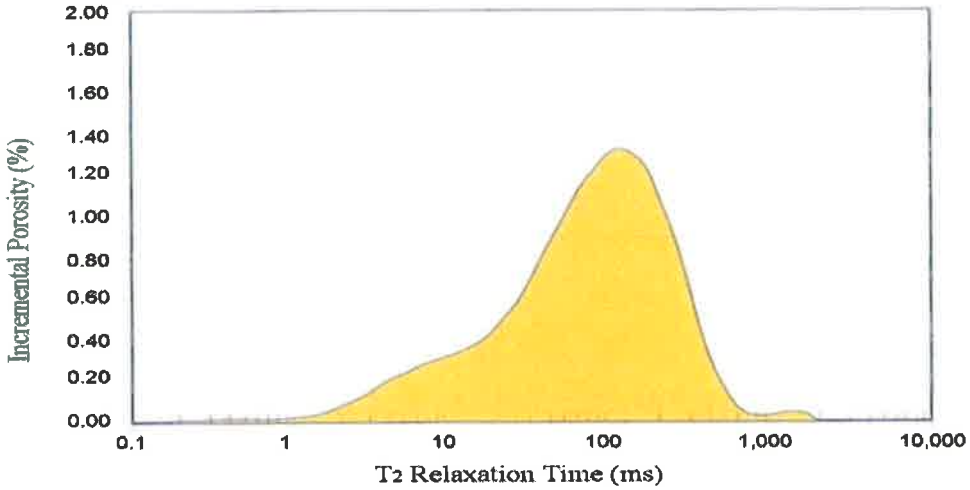

Figure 2.3 Typical NMR T2 distribution for reservoir rock (coates et al, 1999).

field, the variations in pore sizes, the differences between the magnetic susceptibility of pore fluids and rock grains, the fluid viscosity and diffusion, and the presence of paramagnetic impurity ions on the pore walls (Kleinberg and Horsfield, 1990).

For fluids in rock pores three independent relaxation mechanisms are involved (Kleinberg et al., 1994):

- Grain surface relaxation, which affect both T1 and T2 relaxation
- Bulk relaxation, which affect both T1 and T2 relaxation
- Relaxation by molecular diffusion in magnetic field gradients, which only affects T2 relaxation.

Relaxation processes act in parallel. Thus their rates are additive (Kleinberg et al.,1994).

$$\left(\frac{1}{T_2}\right)_{total} = \left(\frac{1}{T_2}\right)_S + \left(\frac{1}{T_2}\right)_B + \left(\frac{1}{T_2}\right)_D \qquad \text{(Eq.2.1)}$$

In this equation (1/T2) S is the surface contribution, (1/T2) B is the bulk contribution and (1/T2) D is the diffusion in field gradient contribution. Similarly for T1 with excluding the diffusion effect,

$$\left(\frac{1}{T_1}\right)_{total} = \left(\frac{1}{T_1}\right)_S + \left(\frac{1}{T_1}\right)_B \qquad \text{(Eq.2.2)}$$

The surface relaxation mechanism will usually be dominant for the wetting phase, and the bulk relaxation mechanism will dominate for the non-wetting phase.

2.1.3.1 Grain Surface Relaxation

Molecules in fluids are in constant motion (Brownian motion) and diffuse about a pore space, hitting the grain surface several times during one NMR measurement. When this happens two interactions may occur. First, hydrogen protons can transfer nuclear spin energy to the grain surface allowing realignment with the static magnetic field, B_0. This contributes to longitudinal relaxation, T_1. Second, protons may be irreversibly dephased, contributing to transverse relaxation, T_2 (Kleinberg and Horsfield, 1990). It has been shown that in most rocks, grain-surface relaxation is the most important influence on T_1 and T_2. The ability of grain surfaces to relax protons is called surface relaxivity, ρ (Kleinberg and Horsfield, 1990). Different surfaces are not equally effective in relaxing hydrogen protons.

Sandstones are about three times more efficient in relaxing pore water than carbonates. Also rocks with a high content of iron or other magnetic minerals have larger than usual values of surface relaxivity and, therefore, shorter T2 relaxation times. Pore size also plays an important role in

surface relaxation. The speed of relaxation depends on how frequently protons can collide with the surface and this depends on the surface-to-volume ratio (S/V). Proton collisions are less frequent in large pores as they have a smaller S/V ratio (Figure 2.4). Therefore, relaxation times are relatively longer. Similarly, small pores have larger S/V and shorter relaxation times (Sen et al., 1990).

For a single pore, the nuclear spin magnetization decays exponentially, so the signal amplitude as a function of time in a T2 experiment decays with a characteristic time constant. Therefore (Kenyon et al., 1995),

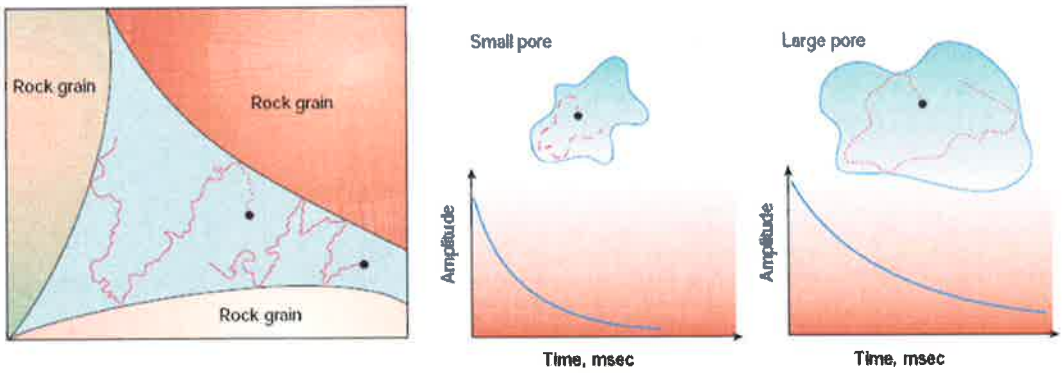

Figure 2.4 Grain surface relaxation. Small pores have faster decay, short T2, and large pores have slower decay, long T2, (Kenyon et al, 1995).

$$\frac{1}{T_2} \cong \rho_2 \left(\frac{S}{V} \right)_{Pore} \qquad \text{(Eq.2.3)}$$

Similarly,

$$\frac{1}{T_1} \cong \rho_1 \left(\frac{S}{V} \right)_{Pore} \qquad \text{(Eq.2.4)}$$

Where,

ρ_2 = T_2 surface relaxibity (T_2 relaxing strength of the grain surfaces)

ρ_1 = T_1 surface relaxibity (T_2 relaxing strength of the grain surfaces)

$(S/V)_{pore}$ = Ratio of pore surface to fluid volume

2.1.3.2 Bulk Fluid Relaxation

Even if grain surfaces and internal field gradients are absent, relaxation occurs in the bulk fluid. Bulk relaxation is caused by the collision between fluid protons and controlled by physical properties, viscosity and chemical composition of the fluids. It can often be neglected in 100% water saturated rock, but it is important when water is in very large pores, such as in vuggy carbonates, and, therefore hydrogen protons rarely contact a surface. Bulk relaxation is also important when hydrocarbons are present. The non-wetting phase does not contact the pore surface, and so it cannot be relaxed by the surface relaxation mechanism. Also, increasing fluid viscosity shortens bulk relaxation times (Sen et al., 1990; Morris et al., 1994).

A bulk relaxation correction must be made when the mud filtrate contains ions of chromium, manganese, iron, nickel or other paramagnetic ions. A sample of mud filtrate can be measured at the well site to calculate the correction.

2.1.3.3 Molecular Diffusion Relaxation

When there are gradients in the static magnetic field, molecular motion increases proton dephasing and hence increases the T_2 relaxation rate ($1/T_2$). The movements of molecules into a region in which the strength of the magnetic field is different can cause this dephasing. Therefore, hydrogen

nuclei relax faster in particular regions due to the inhomogeneties in the static field gradients. Small diffusion effects can be eliminated when the echo spacing (TE) is decreased. This internal field gradient can increase when there is a magnetic susceptibility between the fluids and grain surfaces and it can be sometime uncontrollable. Diffusion has no influence on T_1 relaxation rate ($1/T_1$). In the absence of B_0 gradients, molecular diffusion does not enhance NMR relaxation (Bendel, 1990).

2.1.4 Multi-Exponential Decay

Since the pore space in most reservoirs contains more than one fluid, the spin echo-train does not decay with a single T_2 value but instead with a distribution of T_2 values that are described by Kenyon (1989) in the following equation:

$$B(t) = \sum B_i(0) e^{-\frac{1}{T_{2i}}} \qquad \text{(Eq.2.5)}$$

Where,

$B(t)$ = Measured Magnetization at time t

$B_i(0)$ = Initial magnetization from the i_{th} component of relaxation

T_{2i} = Decay constant of the i_{th} component of transverse relaxation

The summation is for the entire sample, all pores and all different types of fluid.

If a single pore contains 100% water, then that pore will have a single T_2 distribution that will depend on its size, and its spin-echo train will exhibit a single exponential decay. In contrast, if there are multiple pores with 100% water saturation, then there will be multiple T_2 values that correspond to each pore and which depend on the pore sizes. Thus, their composite spin-echo train will exhibit multi-exponential decay (Figure 2.5).

2.2 NMR Application in Formation Evaluation

NMR relaxation measurements can be extremely useful in the extraction of petrophysical information if optimally applied. There have been numerous applications of NMR logging in formation evaluation for the estimation of hydrocarbon reserves and their producibility (e.g. Kenyon et al., 1989; Glorioso et al., 2003). Currently, the most frequently used applications are: (1) porosity estimation, (2) permeability prediction, (3) pore size distribution, (4) irreducible water saturation determination, (5) residual oil estimation, (6) hydrocarbon typing and oil viscosity estimation (Kenyon, 1992).

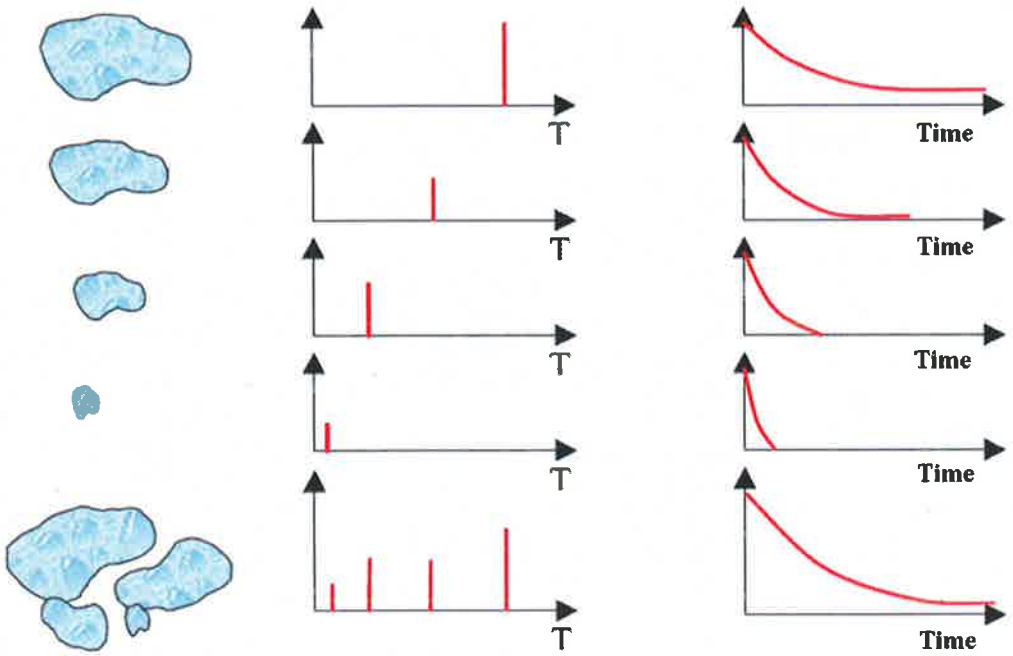

Figure 2.5 Multi exponential decay character of a porous medium with different pore sizes and a single wetting phase (modified from Coates et al, 1999).

2.3 NMR Pore Size Distribution

The pore-size distribution from NMR logging is a significant application in formation evaluation. The data processing to determine the T_2 distribution is called echo-fitting or mapping, and is a mathematical inversion process. Through echo- fitting, the echo amplitude as a function of time is mapped to porosity as a function of T_2 (Figure 2.6). Normally, the T_2 distribution of rocks is a continuous function. However, to simplify fitting the echo train, the mapping process uses a multi-exponential model that assumes that the T_2 distribution consists of discrete relaxation times T_{2i} with corresponding components Φ_i. The values of T_{2i} are pre-selected (for example, 0.5, 1, 2, 4, 8, 16, 32, 64, 128, 256, 512, 1024 ms...), and the mapping process focuses on determining the porosity components of each distribution (Coates et al., 1999). The T_2 value of a single pore is related to the surface-to-volume ratio of the pore, when the rock is 100% water saturated, which is a measure of the size of the pore. Therefore, the T_2 distribution of all pores in the rock sample will represent the pore-size distribution of the sample (Coates et al., 1999).

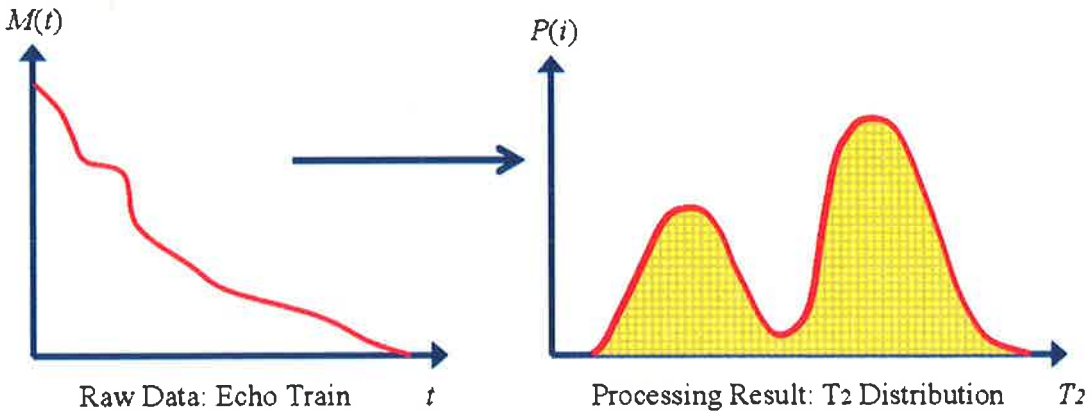

Figure 2.6 Echo train is used in the echo fitting as input, amplitude (M) versus time (t), until the T2 distribution can be mapped as porosity output, porosity (P) versus time (T2), (modified from Coates et al, 1999).

Rocks generally have a distribution of pore sizes, each with their own value of the S/V. The total magnetization is the sum of the signal coming from each pore. The sum of the volumes of all the pores is equal to the fluid volume of the rock. In other words, the total signal is proportional to porosity and the overall decay is the sum of the individual decays, which reflects the pore-size distribution. NMR measurements of porosity and pore size distribution are the key elements of NMR interpretation (Kleinberg et al., 1994).

Many studies have shown that the NMR pore-size distributions and distributions obtained from capillary pressure measurements are related (Marschall et al., 1995). The only difference between them is that the NMR distribution responds to the size of the pore bodies, whereas the distribution from capillary pressure measurements responds to the size of the pore throats for each pressure. The effective surface relaxivity (ρe) is introduced to account for the fact that the distributions respond to different characteristics of the medium. Figure 2.7 compares both distributions and shows that when shifting the effective surface relaxivity (ρe), the pore size distribution from mercury injection data closely overlays the NMR T2 distribution. Thus, effective surface relaxivity (ρe) is proportional to the product of intrinsic surface relaxivity (ρ) and the ratio of pore throat size to pore body size (Marschall et al., 1995).

The NMR data reveals a pore size distribution for sandstone and carbonate not only when the zone is 100% water-saturated but also when hydrocarbons are present. NMR data delineates fine-grained sands from coarse-grained sands (Sen et al., 1990). This information is useful in determining reservoir quality and depositional environments.

2.4 Capillary Pressure (Pc)

The coexistence of two or more immiscible fluids within the voids of a porous medium, such as a reservoir rock, gives rise to buoyancy forces which drive fluid movement. Buoyancy force is created due to the density difference between the non-wetting phase (hydrocarbon) and wetting phase (water). The grain-static resistance force to hydrocarbon movement in a porous rock is termed capillary pressure (Pc). Capillary pressure is controlled by the radius of the pore throats of the rock, the interfacial tension between the non-wetting phase and the wetting phase and the wettability (expressed as the contact angle of hydrocarbon and water against the pore wall), (Schowalter, 1979). The pressure required to move hydrocarbon through water-saturated porous rock is called the displacement pressure.

Capillary pressure (Pc) measurements are important for the characterization of a hydrocarbon reservoir. Also, Pc measurements enable calculation of seal capacity by knowing the displacement pressure of both reservoir and seal rocks. A plot of capillary pressure vs. saturation can be used to understand the distribution of fluids in a reservoir. These curves also help determine the irreducible water saturation of a reservoir rock and the entry pressure of fluid into a water saturated reservoir. These parameters will help in the estimation of reserves.

2.4.1.1 Mercury Porosimetry and Pore Size Distribution

Mercury porosimetry or mercury/air capillary pressure curves are commonly used to measure the distribution of pore throat sizes in a rock sample. A clean rock sample that may be irregular in shape (e.g., a drill cutting or a core) is evacuated of air, placed in a low and then a high-pressure vessel and mercury is introduced into the vessels. The volume of mercury that goes into the sample is precisely measured while the pressure is increased incrementally.

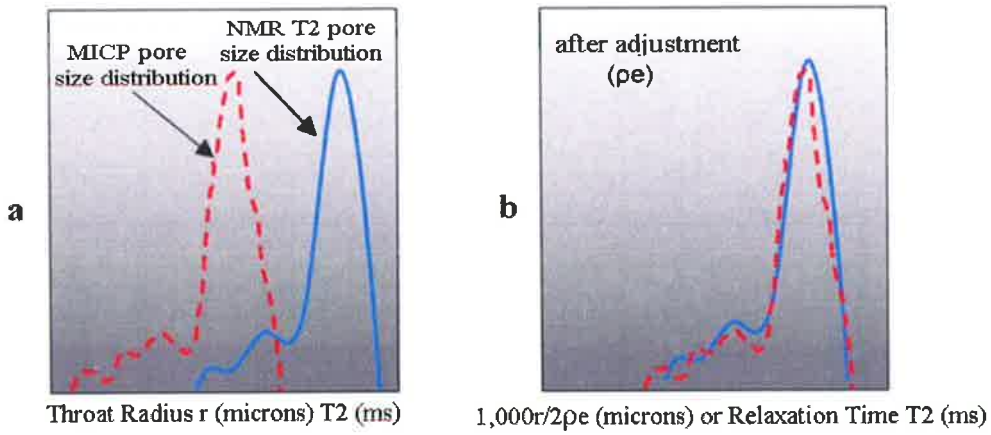

Figure 2.7 Schematic comparison between NMR T2 distribution and MICP pore size distribution. (a) Shows the similarity between two measured curves and (b) shows the excellent calibration between them after relaxivity adjustment, as discussed in text, (modified from Coates et al, 1999).

First, the volume of mercury fills the void space in the vessel which will determine the bulk volume of the sample. Then, with increasing pressure, some mercury volume will fill the surface irregularities of the sample. This is known as "conformance".

The first volume of mercury to enter the rock will be at a pressure called the capillary entry pressure. The displacement pressure is the pressure required for the mercury to actually enter the largest pores in the rock (rather than fill surface roughness). This can be expressed by the following simple equation (Purcell, 1949)

$$P_{Hg} = \frac{2\sigma_{Hg/air} * (-\cos\theta)}{r_{pore}} \qquad \text{(Eq.2.6)}$$

Where,

P_{Hg} is the mercury pressure (dynes/cm2)

σ is the mercury surface tension (dynes/cm)

θ is the mercury/air contact angle

r_{pore} is the pore throat radius (cm)

A typical value for mercury surface tension (σ) is 485 dynes/cm. The contact angle θ between clean mercury and sample pores varies with rock composition and rugosity; however, 140° is generally accepted by industry (Augsburg et al, 1998).

The relation between the mercury pressure and the pore throat size is illustrated in the following reversible relationship, Equation (2.6) becomes:

$$r_{pore} = \frac{107.6}{Pc} \qquad \text{(Eq.2.7)}$$

Where r_{pore} is in cm and P_c is in psi

This equation treats a pore throat as having a pore radius of a perfect cylinder, rather than the tortuous shape of most rock pores. The mercury pressure is increased in small increments and the volume of mercury that enters is recorded. As the mercury pressure is increased, mercury enters pores that are accessible via smaller and smaller pore throats. The plot of mercury pressure versus mercury volume is called the mercury/air capillary pressure curve. The mercury volume may be normalized by the total pore volume of the sample to be expressed as saturation. Usually, $(1-S_{Hg})$ is plotted on the x axis to represent the capillary pressure and saturation of the wetting phase is plotted on the other (y) coordinate. These measurements are automated and are done on a routine basis using standard laboratory MICP equipment.

Additional information can be determined about the pore structure by a sequence of mercury injection and withdrawal steps. The injection (green)

curve in Figure 2.8 represents pores that are filled with mercury during mercury intrusion to increasingly higher pressures. The withdrawal (blue) curve represents the mercury that remain as the pressure is reduced to zero. The hysteresis in saturation during withdrawal process is because of trapping non-wetting phase (disconnected drops of mercury) in the pore bodies. The mercury trapped inside the pore space is illustrated in Figure 2.9.

Capillary pressure curves are also affected by the different clay types. Rocks with similar grain size and sorting but different types of dispersed clays have different pore structure. The discrete particle clays (e.g. kaolinite) act as individual grains and have little effect on the permeability and the capillary pressure curve. Swelling clay such as smectite can affect the permeability, pore volume and thereby the capillary pressure curve especially if the rock is exposed to water. Pore lining chlorite and pore bridging illite decrease the pore throat radius and thus greatly increase the capillary pressure and reduce the permeability (Jorden and Campbell, 1984).

2.4.2 Seal Capacity Determination

Evaluating any hydrocarbon accumulation prospect should include full understanding of seal capacity which refers to the maximum hydrocarbon column a lithology can support (Kaldi and Atkinson, 1997). Therefore, seal capacity increases in fine grained lithology which has smaller pore and throat sizes. Seal capacity is determined by performing mercury injection capillary pressure (MICP) analyses on both reservoir and seal samples.

The laboratory (air/mercury) system in MICP analysis should be converted to the reservoir system (brine/hydrocarbon) before the measurements are applied to the field situation (discussed in detail in methodology section 3.3.1). The most important part of the MICP measurements in terms of seal capacity is the displacement pressure (Pd) of both reservoir (r) and seal (s)

rocks. The displacement pressures (Pd) of both type rocks are applied in the following equation 2.8 to calculate sealing capacity;

$$H_{\max} = \frac{P_{ds} - P_{dr}}{0.433 * (\rho_w - \rho_{hc})} \qquad \text{(Eq.2.8)}$$

Where,

Hmax = Maximum hydrocarbon column can be sealed (in ft)

P_{ds} and P_{dr} : Brine/Hydrocarbon displacement pressure of the seal and reservoir rock (in psi).

ρ_w and ρ_{hc} : Densities of the reservoir fluids, water and hydrocarbon (in g/cm^3).

2.5 NMR and Displacement Pressure Estimation

NMR T2 measures pore body size while mercury injection capillary pressure (MICP) measures pore throat size. There is a general relationship between pore body and throat size in clastic rock and therefore pore to throat size ratio can be derived. Pore to throat size ratio and relaxivity, in T2 response, can be combined in one empirical scale factor (called effective surface relaxivity (ρe) earlier) to adjust the T2 distribution. This adjustment was successfully applied in previous studies by using the following equation (Figure 2.10);

$$P_c = \frac{\rho_e}{T_{2s}} \qquad \text{(Eq.2.9)}$$

Where,

Pc = Capillary pressure (in psi)

T_{2S}= Surface grain relaxation time (in ms), which dominate T_2 response in 100% water saturation

ρ_e = Effective surface relaxivity factor (combining surface relaxivity and pore/throat size ratio)

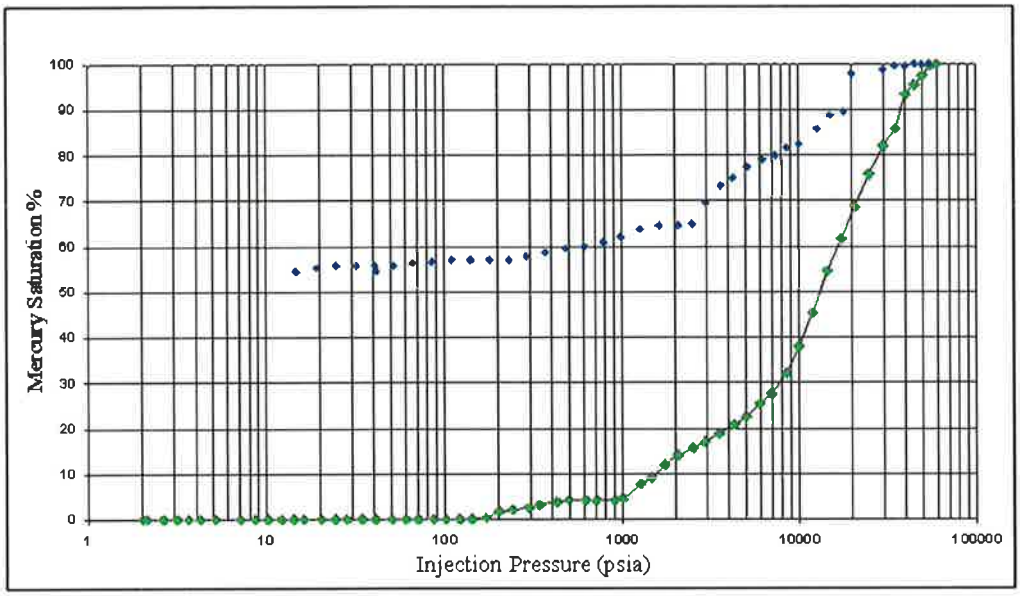

Figure 2.8 Mercury injection and withdrawal capillary pressure curve in very fined grained sandstone. The green curve represents the injection (drainage) and the blue one represents withdrawal (imbibition).

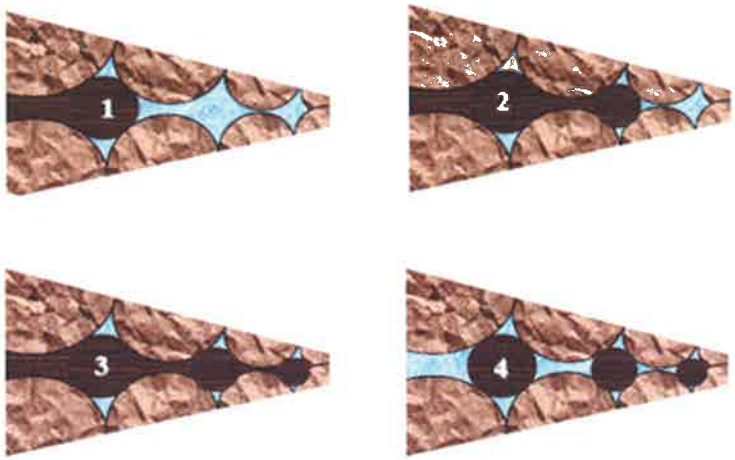

Figure 2.9 Sequences of Mercury Injection and withdrawal (modified from Stegemeier, 1977).

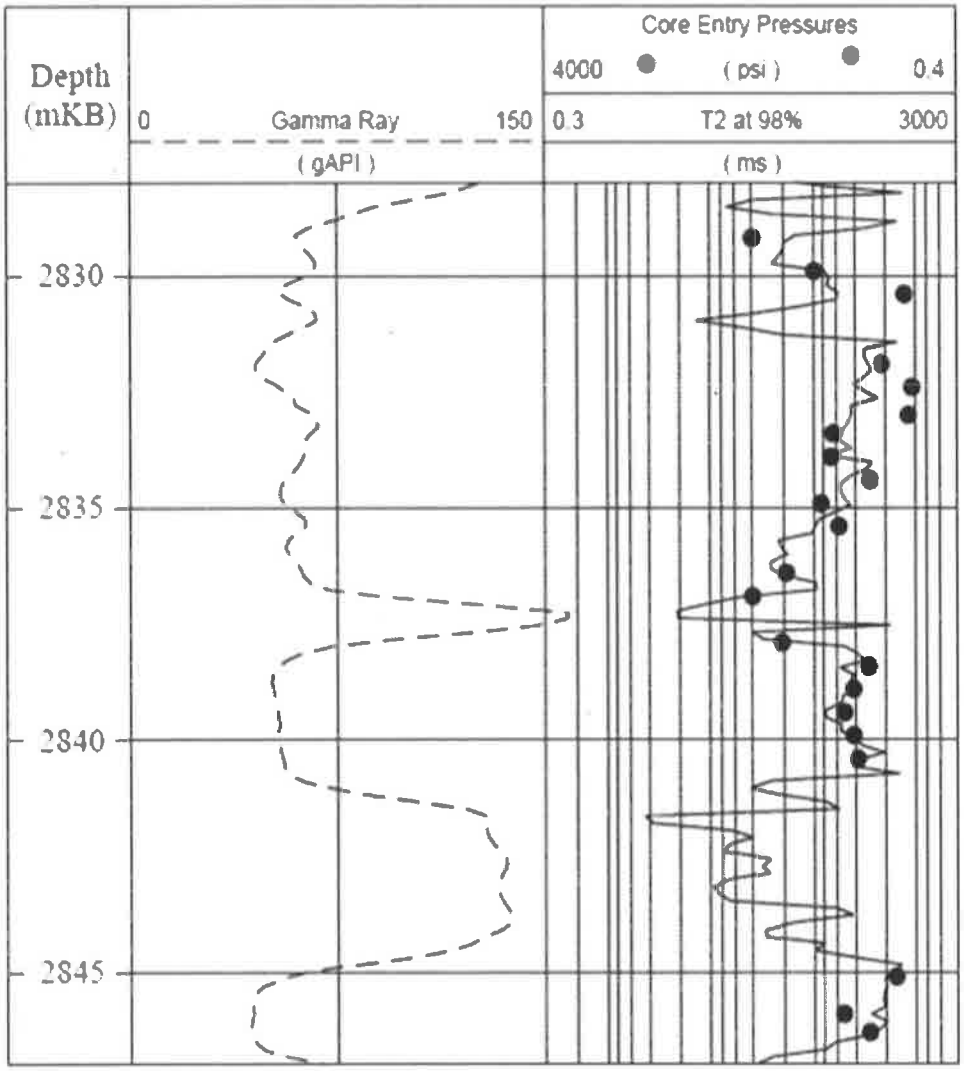

Figure 2.10 Correlation between CoreEval entry pressure and calculated entry pressure at 98% non-wetting phase (NWP) saturation of the T2 distribution in Redman-1. T2 estimates displacement pressure quite well over on the reservoir interval (modified from Boult et al, 1999).

2.6 Geological Overview of the Penola Trough

The Redman Field is located within PEL 32 to the southeast of South Australia in the Penola Trough of the onshore Otway Basin (Figure 2.11). It is approximately 2.5 km northwest of the Katnook gas field. The Otway Basin formed during rifting between Australia and Antarctica in the Late Jurassic and Early Cretaceous.

The Penola Trough is a garben initiated in the early stage of the rifting of the Otway Basin (Lovibond et al, 1995). The Casterton Formation and Crayfish Group were deposited in the Late Jurassic and Early Cretaceous. In the late Early Cretaceous (Aptian-Albian), the area was uplifted and erosion took place at the top of the Crayfish Group. During this erosion, rifting occurred south of the Tartwaup Hingeline axis. The Penola Trough is dominated by a NW-SE trending half graben, particularly in South Australia. The major NW-SE trending Kalangadoo fault system bounds the Penola Trough to the south (Cockshell et al, 1995).

The commercial reservoirs in the Penola Trough are in the Crayfish Group sandstones. In Redman-1 the primary reservoir is the Pretty Hill Sandstone, deposited in the Early Cretaceous above the Casterton Formation (Figure 2.12). An unconformity separates the Pretty Hill Formation and Casterton Formation where an upper boundary is gradational with Laira Formation (Morton et al, 1995).

The Crayfish Group in PEL 32 consists of interbedded sandstones, siltstones and mudstones. This interbedded succession indicates a fluvial-lacustrine environment. The thickness of these sediments is variable throughout the basin because of the subsidence and faulting process (Morton et al, 1995). The Crayfish Group is divided into three formations which are: the Pretty Hill Formation, Laira Formation and Katnook Sandstone.

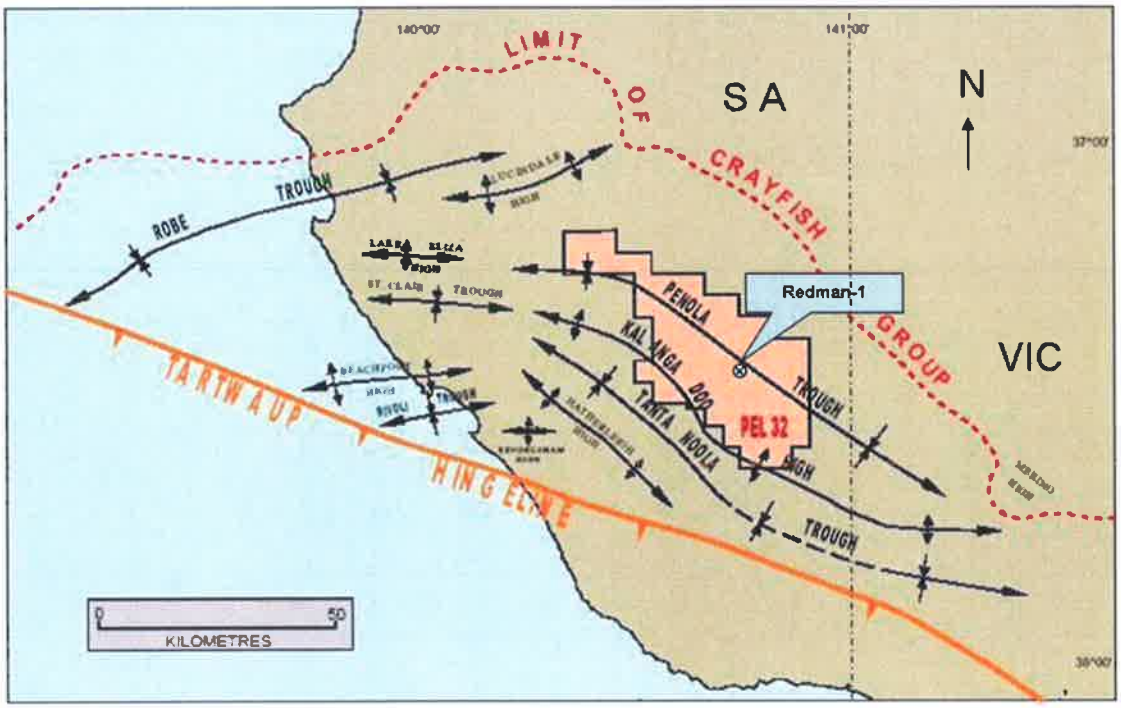

Figure 2.11 Location and structural map of Otway Basin in South Australia (modified from Redman-1 well completion report, Boral Energy Resources 1999).

The Pretty Hill Formation is the oldest formation of the Crayfish Group within the Otway Basin. It extends from the lower Berriasian to Baarmian in age and occurs from *C.australiensis* to lower *F.wonthaggiensis* spore pollen zones inclusively. The Pretty Hill Formation consists of interbedded fine to medium grained sandstone with siltstone and shale interbeds.

The Pretty Hill Formation has a variable lithology across the Otway Basin and consists of sandstones with different degrees of siltstones, clay and detrital composition (Little, 1996). It has six members in the stratigraphic column in PEL 32 area which are, from the bottom to top, Australiensis shale unit, McEachern Sst., Lower Sawpit shale, Sawpit Sst., Upper Sawpit shale and finally Pretty Hill Sst. (Figure 2.12).

The Laira Formation is Barremian to early Aptian in age and occurs in the upper *F.wonthaggiensis* spore pollen zone. It consists of siltstone and claystone deposited in a lacustrine environment with minor fluvial fine-

grained sandstone interbeds (Little, 1996). The formation is best developed in the Penola Trough area with gradational and slightly diachronous lower boundary with Pretty Hill Sst (Morton et al, 1995). In some areas, the Laira Formation was deposited unconformablely on basement. The thickness of this formation is variable from one area to another and the observed thickness ranges from 132 m to 888 m.

The Laira Formation acts as regional seal to Penola Trough reservoirs. This formation has the lowest seal potential risk of the Penola Tough strata and is considered the cap seal for six hydrocarbon accumulation which are charged to spill point (Jones et al, 2000).

The Katnook Sandstone is the uppermost sandy succession in the Crayfish Group, above the Laira Formation, and was defined by Morton (1990) as the equivalent to Unit D of Kopsen and Scholefield's (1990) nomenclature. It was deposited in the Barremian and upper *F. wonthaggiensis* spore pollen zone. This unit consists of fine to medium sandstone interbedded with micaceous siltstone. In some areas, it is absent due to erosion or facies change since it was deposited in a low sinuosity meandering fluvial to distal braided fluvial environment (Morton, 1990).

The Katnook Sandstone has a variable thickness throughout the Otway Basin and it thins towards the west and the north. It has a gradational and strongly diachronous lower boundary with the Laira Formation. The Katnook Sandstone contains significant hydrocarbon accumulations in the Penola Trough. The Katnook Field is a gas field, which produces from a gentle structural dome of Katnook Sandstone and Windermere Sandstone reservoir. The Eumeralla Formation, a silty claystone, is the cap seal for this hydrocarbon accumulation.

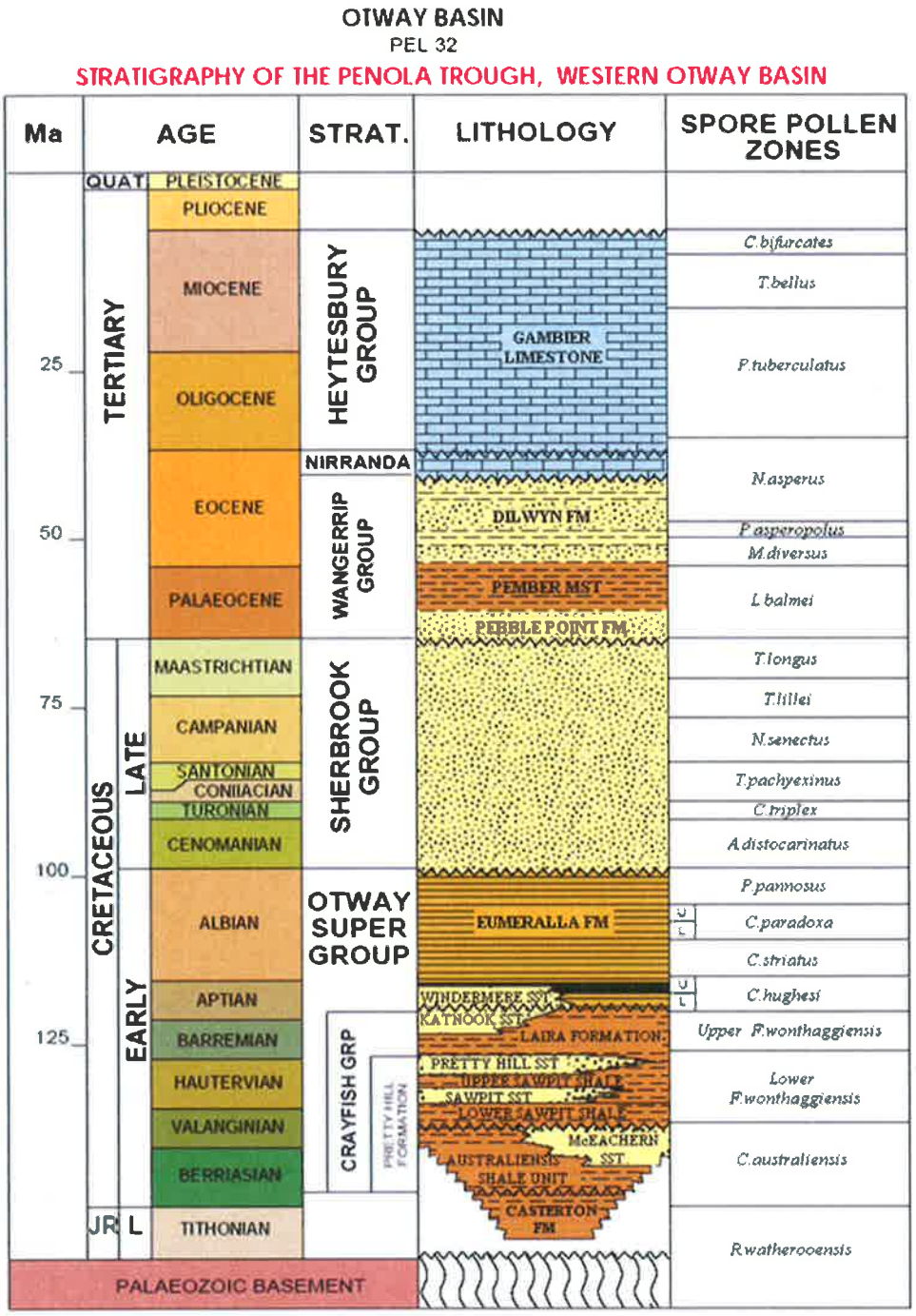

Fig. 2.12 Stratigraphic column of western (PEL 32) Otway Basin (modified from Redman-1 well completion report, Boral Energy Resources 1999).

CHAPTER THREE
PETROPHYSICAL AND MINERALOGICAL MEASUREMENTS

3.1 Introduction

Redman-1 core was cut in 1998 from the Pretty Hill Sandstone reservoir in the Penola Trough of Otway Basin. The 18m core (2828.81m - 2846.76m) consists of a 9m channel facies, a 4.5m bar facies and a 4.5m floodplain facies. In previous work, conventional core analysis was performed on 30 core plugs in the porous intervals and then more special core analyses (CorEVAL) were conducted on a subset of 22 samples. In this study, nine core plugs were cut in the floodplain facies and two other core plugs were obtained from the previous dataset. This chapter explains in detail the core sample selection and preparation and describes each petrophysical and mineralogical laboratory technique used.

3.2 Sample Selection and Preparation

A total of 11 samples were selected from the floodplain facies in Redman-1 core for analyses. Samples were selected on the basis of grain size and sorting (Figure. 3.1). eight new core plugs (1½" diameter, 2" length) were cut dry from the 2/3 of the core to prevent clay swelling by water adsorption. These core plugs were cut horizontal, parallel to bedding orientation. All core plugs were dried in an oven at 80° C to dehydrate the sample.

Off-cut samples were taken from the core for MICP, SEM, XRD, XRF and thin sections. The following laboratory techniques were performed on these samples:

- Mercury injection capillary pressure (MICP) = 11 samples
- Scanning Electron Microscope (SEM) = 11 samples

- X-Ray Diffraction (XRD) = 11 samples
- X-Ray Fluorescence (XRF) = 11 samples
- Porosity and Permeability = 9 core plugs samples
- Thin Sections = 3 samples

Porosity and permeability measurements were performed on just 9 core plug samples. The other two could not be measured because of either core plug fractures or there was not enough sample to cut a core plug.

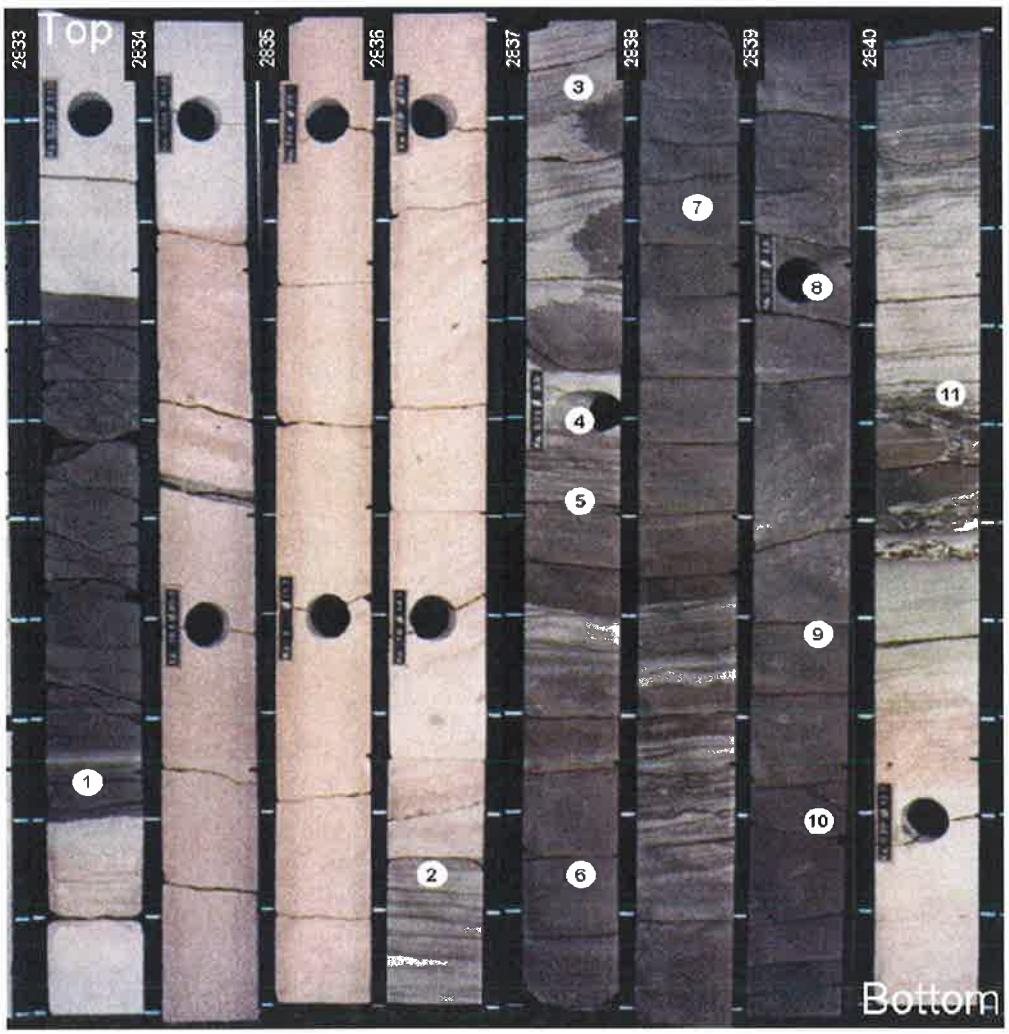

Figure 3.1 Redman-1 core image from 2833 to 2841m (2836.81-2844.81m log-depth) where the flood plain facies is dominant. The project samples are illustrated here (modified from Redman-1 well completion report, Boral Energy Resources 1999).

3.3 Pore Measurement Techniques

Different techniques were used in the mineralogical and petrophysical description of the 11 samples to ensure good characterization of the fine grained rocks. These measurements include MICP, SEM, porosity and permeability, XRD, XRF, thin section description and point counting.

3.3.1 Mercury Injection Capillary Pressure (MICP)

Mercury Injection Capillary Pressure is based on the physical principle that non-wetting liquid, such as mercury, will not penetrate pores until adequate pressure is applied to force it to enter the pore systems. The Washburn equation (Equation 3.1) gives the relationship between the applied pressure and the pore size (Washburn, 1921).

$$\mathbf{PD = -4\,\gamma\cos\theta} \qquad \text{(Eq.3.1)}$$

P applied pressure,

D Pore throat diameter,

γ surface tension of mercury

θ contact angle between mercury and the pore wall.

Mercury intrusion volume is calculated continuously while pressure gradually increases. MICP results are controlled by the size and distribution of pore throats which characterize different rock types.

The Micromeritics Autopore 9410 mercury injection porosimeter machine was used to measure capillary pressure on all the 11 samples (Figure 3.2). This machine is composed of two systems, one for low pressure runs and the other for high pressure runs. A sample is initially run in the low pressure system and followed quickly by the high pressure run to enable the mercury to penetrate the smallest pore throats.

The low pressure system consists of two sample ports, vacuum pump, a mercury reservoir and associated mercury fill chamber, an air pump, a

pressure sensor and the associated valves (Figure 3.3). The high pressure system consists of a high pressure port, a pump, a variac, pressure sensor and the associate valves (Figure 3.4). The high pressure system can operate to pressure of 60,000 psia (Bentley, 2000). The Autopore 9410 instrument is connected by cable to a desktop computer which controls the instrument and records all measurements including mercury intrusion, pressure and sample weight.

All samples were dried and weighed before being loaded into the penetrometer which was then sealed and placed in the low pressure port of Autopore 9410 machine. A vacuum pump was used to evacuate the sample to 0.5 torr. The vacuum was held for approximately five minutes, and the mercury was pumped from the reservoir to fill the chamber and the penetrometer. Continuous mercury intrusion and pressure readings were taken gradually from 2 psia to 40 psia in the low pressure system. The sample was then returned to atmospheric pressure, removed from the penetrometer and weighed.

The sample was then placed into the high pressure penetrometer port. The high pressure run was started at 45 psia and stepwise mercury intrusion and pressure readings were taken until the pressure reached 60,000 psia. The pressure was then decreased back to atmospheric pressure with 20 second equilibration to each pressure increment.

MICP data are displayed in excel worksheets and diagrams, Appendix-A. All mercury saturation data were normalized to take out the conformance effect which represents the mercury volume required to fill the surface irregularity of the sample. Then, pore throat size distribution can be displayed by plotting capillary pressure versus mercury intrusion volume. The distribution can be displayed as an incremental or cumulative capillary pressure curve when incremental or cumulative mercury volume are used respectively. The pore throat diameter was calculated using the Washburn

equation (Eq.3.1) since all the terms in that equation are known except pore throat diameter.

The MICP laboratory measurements should be converted to reservoir conditions to be applied in any calculation or calibration. The conversion simply converts the data from air/mercury capillary pressure to a brine/hydrocarbon capillary pressure. The conversion was performed by knowing the interfacial tension and the contact angle of both side air/mercury and brine/hydrocarbon using Equation 3.2 (Purcell, 1949).

$$Pc_{b/hc} = Pc_{a/m} * \frac{\sigma_{b/hc} * \theta_{b/hc}}{\sigma_{a/m} * \theta_{a/m}} \qquad \text{(Eq.3.2)}$$

Where,

$Pc_{b/hc}$ = Capillary pressure at reservoir condition (Brine/Hydrocarbon)

$Pc_{a/m}$ = Capillary pressure at laboratory condition (Air/Mercury)

$\sigma_{b/hc}$ = Interfacial tension at reservoir condition (Brine/Hydrocarbon)

$\theta_{b/hc}$ = Contact angle (wettability) at reservoir condition (Brine/Hydrocarbon)

$\sigma_{a/m}$ = Interfacial tension at laboratory condition (Air/Mercury)

$\theta_{a/m}$ = Contact angle (wettability) at laboratory condition (Air/Mercury)

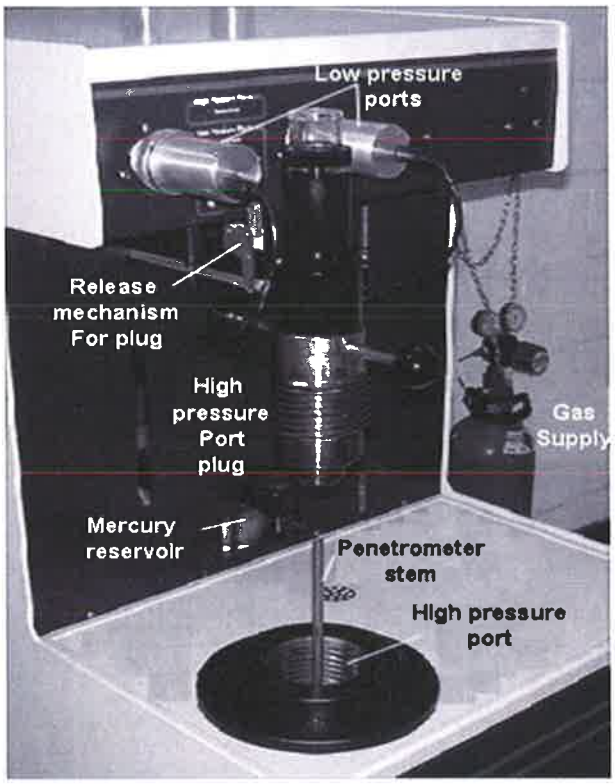

Figure 3.2 Micromeritics Autopore 9410 mercury injection porosimeter (modified from Bentley, 2000).

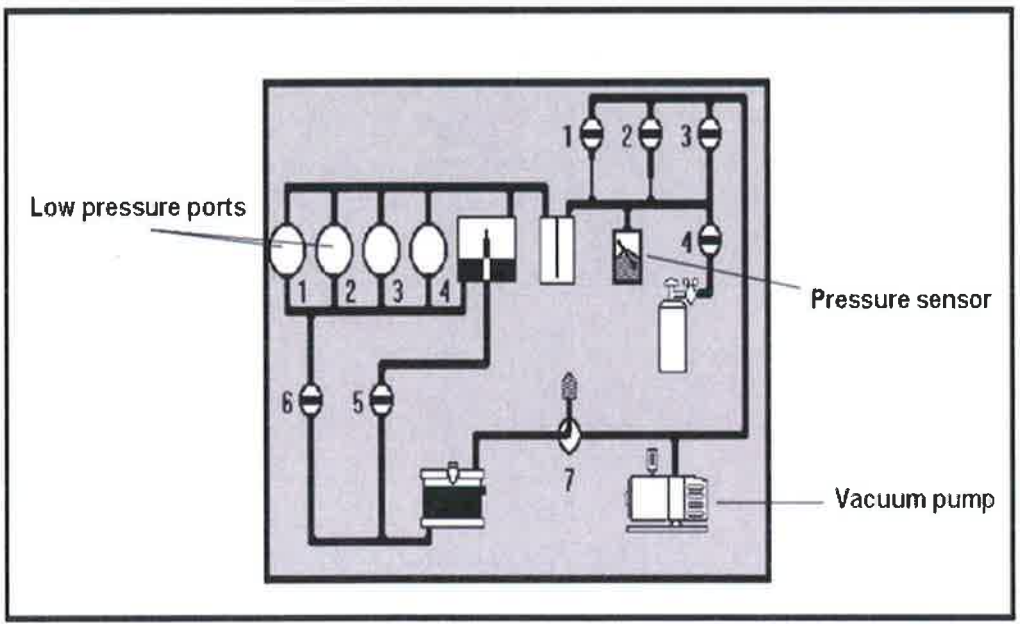

Figure 3.3 Schematic of low pressure section in Micromeritics Autopore 9410 mercury injection porosimeter (modified from Bentley, 2000).

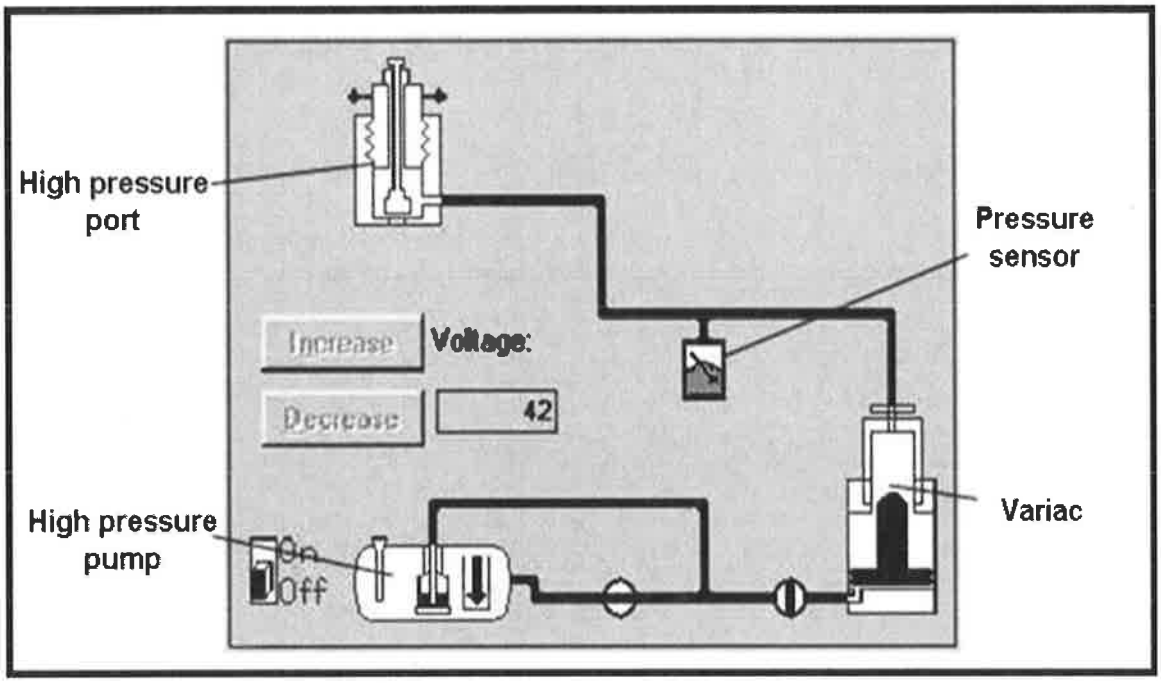

Figure 3.4 Schematic of high pressure section in Micromeritics Autopore 9410 mercury injection porosimeter (modified from Bentley, 2000).

3.3.2 Scanning Electron Microscopy (SEM)

Scanning Electron Microscopy (SEM) was used to visualize the texture, mineralogy and pore system of the samples. The tool produces a stream of electrons with accelerating voltage between 10-30 kv. Once the electron beam hits the surface of the sample, some electrons reflect as backscattered electrons (BSE) and some are emitted as low energy secondary electrons (SE). BSE and SE are collected by a scintillator which sends a pulse of light when electrons from the sample are detected. This light emitted is converted to an electrical signal and amplified by the photomultiplier (Trewin, 1988). These electrical signals are converted to an image and the contrast in the image is due to the general topography and orientation of the sample, chemistry of the sample surface and difference in the electrical properties of the sample.

At every depth interval 2 small blocks (0.5cm by 0.5cm) were cut, one parallel and the other perpendicular to the bedding surface. These 22 samples (11 depth interval) were coated with 2nm thick carbon/gold. Initially a *Philips XL20* was used to obtain the pore geometry, clay types and textural information from secondary electrons (SE). A 10-15 kv accelerating voltage was applied to produce better images. Also, X-Ray diffraction with *XL20* was used to identify chemical composition of some minerals.

An *XL30* also was used to acquire higher SE magnification images with better resolution for particular samples. For polished thin sections, BSE and SE were used in the *XL30* to identify the texture and chemical differences of three thin sections. The *XL30* was also used for other samples which were covered with epoxy material to determine how far this material penetrated the samples. A 10-15 kv accelerating voltage was also used in this tool.

Backscattered electrons (BSE) image were performed on the thin sections using Philips XL30. Thin sections were polished to obtain better image by using BSE in Philips XL30. BSE image provide better identification of the chemical contrast between grains especially when perthite existed in the samples.

3.3.3 Porosity and Permeability Measurements

Porosity and permeability were determined by routine core analysis. The porosity analysis was measured using helium whereas permeability was measured by air on 9 core plugs of Redman-1.

For porosity measurements, the plugs were sealed in a steel chamber (matrix cup) and a known volume of helium at 100 psi reference pressure introduced to the cup. From the resultant pressure drop the unknown volume (i.e. the grain volume), was calculated using Boyle's Law. The bulk

volume of every plug was determined by immersed mercury. The difference between the grain volume and the bulk volume is the pore volume. The porosity is calculated as the volume percentage of pore space with respect to the bulk volume. The porosity calculated using this technique is a total porosity.

Boyle's Law $P_1 V_1 = P_2 V_2$ (Eq.3.3)

$P_1 Vr = P_2 (Vr + Vc - Vg)$

Where,
P_1 = initial pressure
Vr = reference cell volume
Vc = matrix cup volume
Vg = grain volume
P_2 = final pressure

$PV = BV - GV$

Ambient Porosity % = PV/BV x 100

Where,
PV = ambient pore volume
BV = ambient bulk volume
GV = grain volume

For permeability measurements, which were done by Amdel Ltd, the plugs are placed in a hydrostatic cell at a confining pressure of 400 psig. This pressure is used to prevent bypassing of air around the sample when the measurement is made.

During the measurement a known air pressure is applied to the upstream face of the sample, creating a flow of air through the sample. Permeability for each sample is then calculated using Darcy's Law through the knowledge of the upstream pressure and flow rate during the test, the viscosity of air and the plug dimensions.

$$Ka = \frac{2000 * BP * \mu * q * L}{(P_1^2 - P_2^2) * A} \qquad \text{(Eq.3.4)}$$

Where, Ka = air permeability (md)
BP = barometric pressure (atmospheres)
μ = gas viscosity (cp)
q = flow rate (cm^3/s)
L = sample length (cm)
P_1 = upstream pressure (atmospheres)
P_2 = downstream pressure (atmospheres)
A = sample cross sectional area (cm^2)

3.4.1 Porecast analysis

Pore geometry is a very important petrophysical characteristic and porecast analysis is one of the techniques that can be used to evaluate it. The technique is also useful to estimate the pore to throat size ratio. The porecast is made by impregnating the sample with blue epoxy resin, making sure the pore system is penetrated with the epoxy material. The grains or rock are then dissolved by hydrofluoric acid (in clastic sedimentary rocks) or hydrochloric acid (in carbonate rocks). This leaves the pore network preserved as a cast which can be examined using SEM (Trewin, 1988).

The impregnation procedure was originally used for thin sections preparation. The samples were first impregnated with blue epoxy resin in a pressure chamber. A vacuum was then applied to remove the air from the pores. Every few minutes the air was released into a chamber and this process was repeated for 30 minutes. Finally, the sample was allowed to be set and the epoxy hardened for 24 hours under room temperature.

The impregnated samples were put in 10M hydrofluoric acid for 4 days which was effective in dissolving the silicate minerals. All selected samples were clastic rocks (v. fine Sandstone - fine Siltstone). A large

proportion of the sample material was dissolved but some of the bulk sample remained which allowed observation of some of the consolidated part of the samples.

All samples were examined using the Philips *XL30* scanning electron microscope (SEM). The Philips *XL30* tool has better resolution at higher magnification which was extremely useful for very fine grained rock.

3.4 Mineralogical Determination Techniques

Four techniques have been used to identify different mineralogy. These techniques are X-ray diffraction analysis, X-Ray fluorescence, thin sections and point counting.

3.4.1 X-Ray Diffraction Analysis (XRD)

X-ray diffraction (XRD) is used to identify the bulk mineralogy of sedimentary rock samples. According to Hardy et al (1988), the best tool to determine the clay types in very fine grained rocks such as shale is XRD. The X-ray tool sends a subparallel beam to the powder sample that is rotated at regular speed. Every mineral has different characteristic diffraction angles and they are recorded when the beam is diffracted to the receiver. The x-ray diffraction intensity that will be derived from the sample depends on the differences between grain size, crystallinity, relative abundance, structure and chemical composition.

XRD analysis was made by CSIRO for all 11 samples. Bulk samples were pre-ground for 15 seconds in a tungsten carbide mechanical mill to pass through a 0.5mm sieve. A 1g sub-sample was further ground for 10 minutes in a McCrone micronizing mill under ethanol. The resulting slurry was oven dried at 60°C then thoroughly mixed in an agate mortar and pestle

before being lightly pressed into aluminium sample holders for X-ray diffraction analysis.

XRD patterns were recorded with a Philips PW1800 microprocessor-controlled diffractometer using Co Ka radiation, variable divergence slit, and graphite monochromator. The diffraction patterns were recorded in steps of 0.05° 2 theta with a 1.0 second counting time per step, and logged to data files for analysis. Quantitative analysis was performed on the XRD data using the commercial package SIROQUANT from Sietronics Pty Ltd. The data were first background subtracted and calibrated for the automatic divergence slit. The results are normalized to 100%, and hence do not include unidentified or amorphous materials.

3.4.2 X-Ray Fluorescence (XRF)

X-Ray Fluorescence is widely used in the determination of the major and trace element chemistry of a rock sample. It depends on the excitation of a powder sample by X-rays. Every element in the sample has different wavelength characteristic of the X-rays fluorescence which is excited by the primary X-ray. The concentration of the elements is determined by the intensity of the X-rays fluorescence (Rollinson, 1993).

XRF analysis was made also by CSIRO for all 11 samples. Approximately 1g of each oven dried sample (105°C) was accurately weighed with 4g of 12-22 lithium borate flux. The mixtures were heated to 1050°C in a Pt/Au crucible for 12 minutes then poured into a 32mm Pt/Au mould heated to a similar temperature. The melt was cooled quickly over a compressed air stream and the resulting glass disks were analysed on a Philips PW1480 wavelength dispersive XRF system using a dual anode Sc/Mo tube and algorithms developed in the laboratory.

All the minerals were analyzed in oxide form and there no separation analysis was made for the heavy minerals. Iron content was reported as Fe2O3 without measuring the Fe^{2+}/Fe^{3+} ratio.

3.4.3 Thin Section Petrology

Three samples were selected based on grain size for thin sections. The first one represented the best seal lithology (massive clayey siltstone "Sample 7 (2841.99m)"), the second one represented a poor seal lithology (very fine sandstone "Sample 3 (2840.86m)") and the third one comprises clayey fine siltstone clasts inside fine to medium sandstone "Sample 11 (2844.08m)".

Thin sections were prepared by Pontifex and Associate in Adelaide. Samples were impregnated with blue epoxy resin in a pressure chamber. Vacuum was then applied to suck the air from the pores. Every few minutes the air was released into a chamber and this process repeated for 30 minutes. Finally, the sample was allowed to be set and the epoxy hardened for 24 hours under room temperature.

A thin slice was cut for every sample with a diamond saw. The slice was ground for around 30 minutes. Extra lapping steps were performed to produce a highly polished surface which helps to increase resolution in microscopy (Miller, 1988). A small amount of blue epoxy resin was applied to the first face and then the glass slide was attached under vacuum pressure. The second face was cut automatically on diamond-impregnated saw with a vacuum chuck. The precision lapping machine lapped the slice to a final 30 μm thickness.

Thin sections were examined under Olympus BH2-UMA petrographic microscope with an Olympus DP11 camera attached (Figure.3.5). Petrographic description of thin sections was possible down to the very fine sandstone samples. Siltstone and finer samples were difficult to examine. Thin section descriptions focused on the abundant minerals in the

samples. Quartz, albite, orthoclase, biotite, muscovite, clays and accessory minerals were the main minerals which were described.

3.4.4 Point Counting

An Olympus BH2-UMA petrographic microscope with pointcounting equipment attached was used for point counting. To assure better results in fine grained samples, the procedure used was 300 counts per thin section with 1 mm vertical interval and 0.65 mm median horizontal interval. Eight mineral categories were used for point counting because possibility to distinguish different very fined grains is more difficult. These eight minerals are quartz, albite, orthoclase, biotite, muscovite, rock fragments, organic matter and clays.

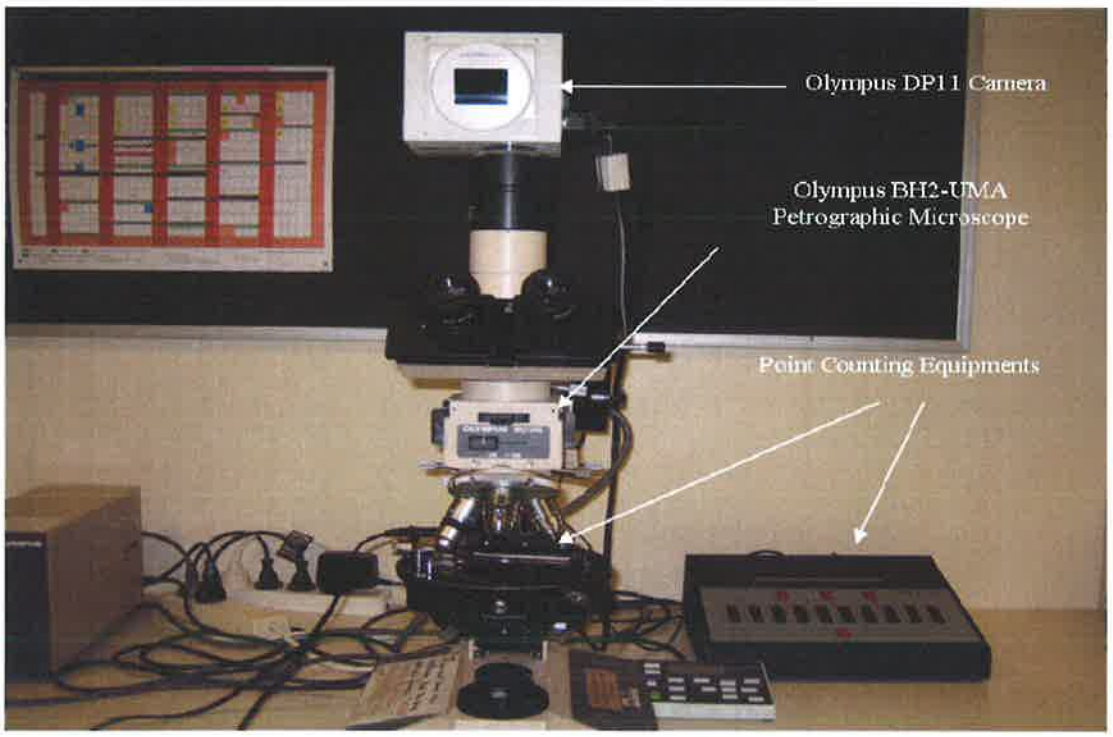

Figure 3.5 Olympus BH2-UMA petrographic microscope with an Olympus DP11 camera attached and pointcounting equipment used in thin section analysis.

CHAPTER FOUR
PETROLOGY

4.1 Core Description

This study focuses on the 4.5 m of the floodplain facies which is separated by channel and bar facies (Figure 4.1). The interval is predominately siltstone. Grain size ranges from very fine sandstone to fine siltstone and the mineralogy from quartz and feldspar rich to clay rich rock. Higher organic and mica content are observed in the finer grained intervals.

Figure 4.1 shows an intraclast conglomerate which was deposited at the base of the channel (2844.3m) which represents a sequence boundary. The intraclasts comprise large clasts (gravels) made up of very fine siltstone which were transported from previous deposits and mixed with medium sandstone. The intraclast conglomerate grades rapidly into very fine sandstone followed by a flood plain interval starting from 2844m with coarse siltstone interbedded with very fine sandstone (Figure 4.1). Blocky very fine grained siltstone with high organic content extends to 2843m. Slight bioturbation is present throughout the flood plain facies. Minor micro fractures occur at 2843.1 with clay smear along the micro fracture plane.

Coarsening upward characterizes the interval between 2843 to 2842.2m with interbedded layers of very fine and very coarse siltstone. Blocky very fine siltstone makes up the interval between 2842.2 and 2841.1m and represents a low energy depositional environment. The amount of very fine sandstone increases upward from 2842.2m until the top of the flood plain facies, 2840.66m, occurring as interbedded layers within the coarse siltstone. Occasional light gray lithic clasts with lamination occur between 2841.2 and 2840.8m. A channel facies was deposited above the flood plain interval between 2840.66 to 2837.6m. Very fine siltstone (clayey siltstone)

flood plain sediments with burrows infilled with silt occurs between 2837.6 and 2837.1.

Laboratory analyses were performed on 11 samples to identify their textural features and mineralogical composition to complement the petrophysical data. The location of samples is shown in Figure 4.1 and Table 4.1. The samples range from clayey siltstone to fine sandstone. Three thin section samples were prepared and examined using a petrological microscope. These are interbedded very fine sandstone-coarse siltstone (Sample 3), massive clayey fine siltstone (Sample 7) and heterolithic sandstone-siltstone (Sample 11). Figure 4.2 shows the scanned thin sections. Photomicrographs were taken to illustrate different minerals: most are taken from the very fine sandstone (Sample 3). The minerals observed in the fine grained rock interval of the Pretty Hill Sandstone at Redman-1 can be divided into detrital and authigenic phases and are described below.

4.2 Detrital Mineralogy

The detrital mineralogy of the fine grained interval of Pretty Hill Sandstone consists mainly of quartz, feldspar (albite and orthoclase), mica (biotite and muscovite) and clays (smectite and kaolin). The accessory minerals include garnet. The different minerals were plotted against depth using XRD bulk mineralogy and have no distinguishing trend with depth (Table 4.2; Figure 4.3).

Quartz and feldspars increase relative to mica and clay contents in the coarser grained samples Sample 2 (2840.66m), Sample 3 (2840.86m) and Sample 4 (2841.21m). These samples represent the gradual shift from flood plain to channel facies. Commonly, the flood plain interval is characterized by the change from coarse siltstone to fine sandstone and clayey fine siltstone.

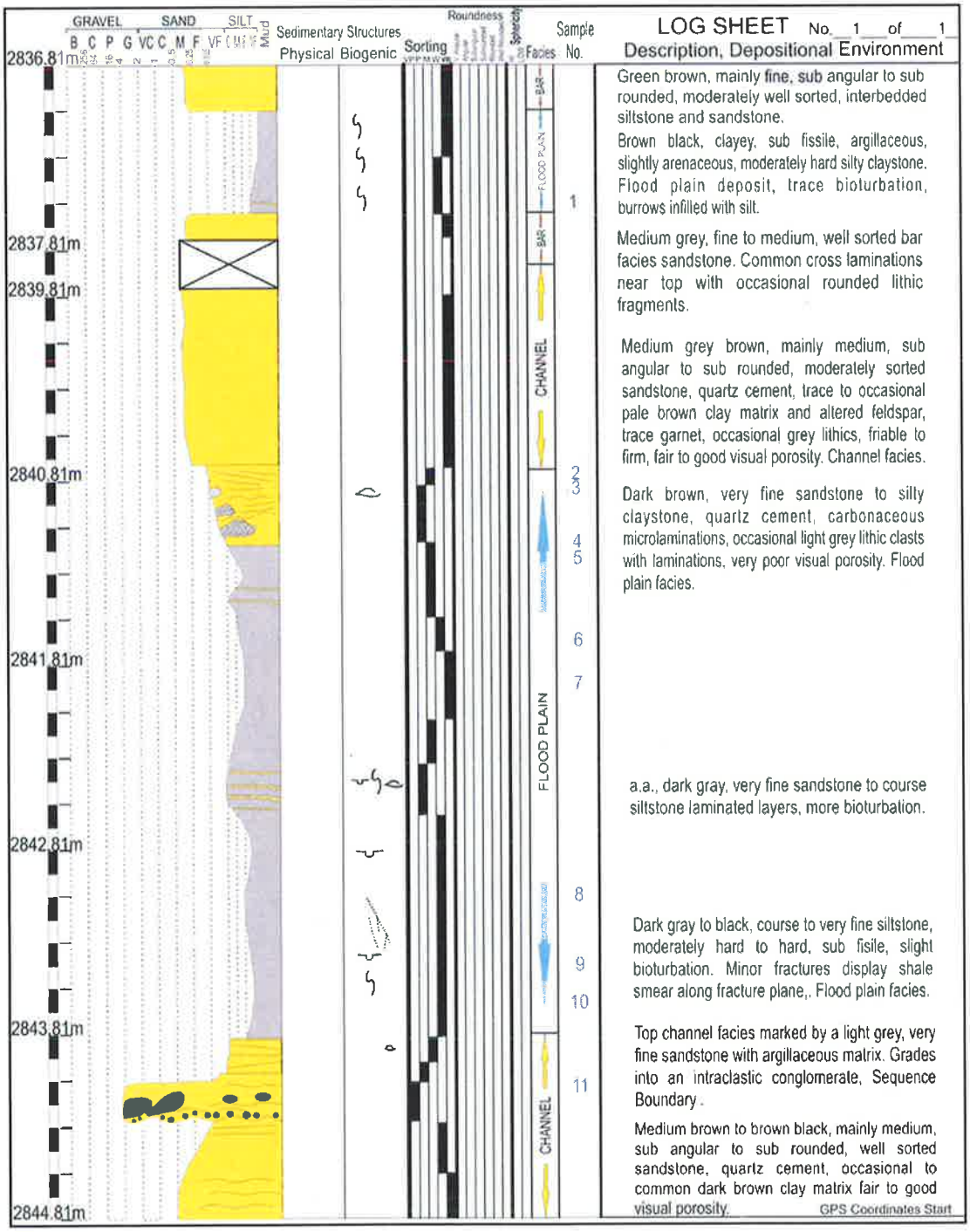

Figure 4.1 Redman-1 core log for the very fine grained interval (2836.81-2844.81m)

Sample No	Core Depth	Log Depth	Sample Classification	MICP	NMR	XRD	SEM	XRF	Thin Section	Porosity and Permeability
1	2833.76	2837.57	course siltstone	Yes	Yes	Yes	Yes	Yes		
2	2836.85	2840.66	laminated fine sandstone-siltstone	Yes	Yes	Yes	Yes	Yes		Yes
3	2837.05	2840.86	laminated very fine sandstone-siltstone	Yes	Yes	Yes	Yes	Yes	Yes	Yes
4	2837.4	2841.21	laminated coarse-fine siltstone	Yes	Yes	Yes	Yes	Yes		Yes
5	2837.49	2841.3	laminated coarse-fine siltstone	Yes	Yes	Yes	Yes	Yes		Yes
6	2837.85	2841.66	massive fine siltstone	Yes	Yes	Yes	Yes	Yes		Yes
7	2838.18	2841.99	massive fine siltstone	Yes	Yes	Yes	Yes	Yes	Yes	Yes
8	2839.27	2843.08	massive fine siltstone	Yes	Yes	Yes	Yes	Yes		
9	2839.61	2843.42	massive fine siltstone	Yes	Yes	Yes	Yes	Yes		Yes
10	2839.8	2843.61	massive fine siltstone	Yes	Yes	Yes	Yes	Yes		Yes
11	2840.27	2844.08	inhomogeneous sandstone-siltstone	Yes	Yes	Yes	Yes	Yes	Yes	Yes

Table 4.1 The different analyses were performed on the 11 fine lithology samples of Redman-1 core. Thin sections from three samples (colored yellow) with different grain size were examined under microscope.

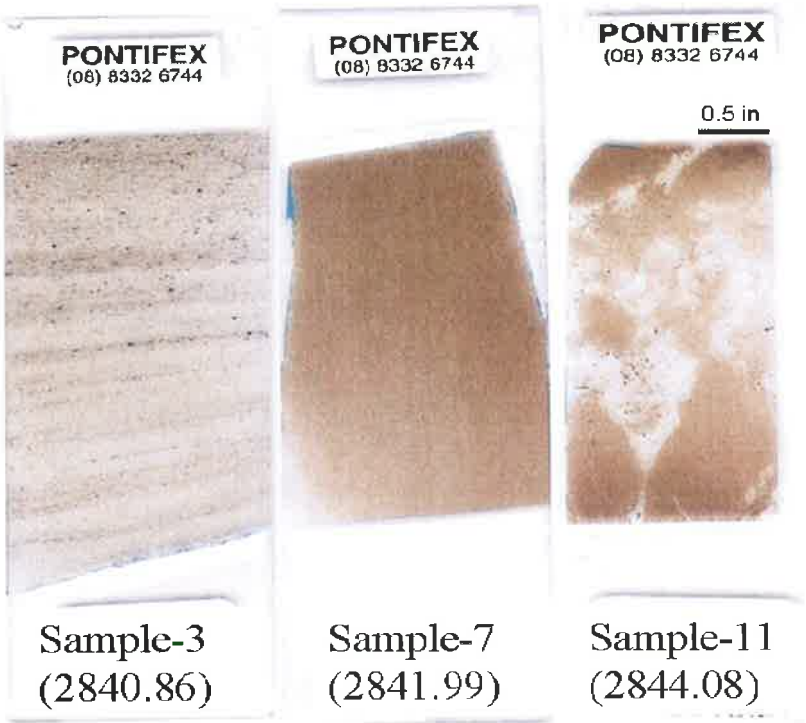

Figure 4.2 Thin section images from samples with differences in grain size, sorting and homogeneity.

4.2.1 Quartz

Quartz measured from XRD ranges from 9% in clay rich samples, such as Sample 1 (2837.57m), to 32% in sandier samples, such as Sample 4 (2841.21m). The quartz intensity is between 1800- 6000 counts on XRD (Figure 4.4 and Appendix-D). Point counting (Table 4.3) indicates similar percentages as the XRD quartz results (Table 4.2) but point counting is less accurate than XRD analysis in very fine grained rocks.

The most abundant quartz type is monocrystalline (Figure 4.5) within the coarse siltstone and fine sandstone fractions. The quartz, is characterized by no inclusions, and is interpreted to be of volcanic origin (Little and Phillips, 1995).

4.2.2 Feldspars

Feldspars range from 19% to 35% percent in the very fine grain interval of the Pretty Hill Formation based on XRD analysis (Table 4.2) and 18% to 25% from point counting (Table 4.3). The dominant feldspar type is albite (32-17%) with minor amounts of K-feldspar (orthoclase) (Table 4.2). Microcline was recognized in trace amounts in the fine sandstone and may increase with increasing grain size.

The abundance of plagioclase (Figure 4.6) among the total feldspars probably reflects a predominantly volcanic provenance. The plagioclase was probably originally andesine but has since been albitized by digenesis (Little, 1996). Also, albitization of originally K rich feldspar, which was reported by Little (1996), may contribute to the high albite content. The present orthoclase concentration is between 2 and 4 percent. It is slightly to completely altered to authigenic minerals (Figure 4.7). Orthoclase may contribute to pore filling clays in the samples. Also, it has some inclusions of Na-plagioclase distinguishable from original perthitic texture which

suggests diagenetic replacement of potassium by sodium (Little and Phillips, 1995).

Redman-1 XRD Bulk Analysis Results											
Sample No.	Core-depth	Log-depth	Quartz (%)	Albite (%)	Orthoclase (%)	Mica (%)	Chlorite (%)	Smectite (%)	Kaolin (%)	Calcite (%)	Pyrite (%)
1	2833.76	2837.57	9	17	2	26	8	32	7	-	-
2	2836.85	2840.66	24	32	3	10	7	16	6	2	-
3	2837.05	2840.86	19	29	4	12	8	22	5	-	-
4	2837.4	2841.21	32	28	3	11	7	8	11	-	-
5	2837.49	2841.3	24	20	2	22	9	18	4	-	-
6	2837.85	2841.66	26	20	3	21	8	16	5	-	-
7	2838.18	2841.99	22	20	3	22	9	20	4	-	-
8	2839.27	2843.08	24	23	3	21	7	17	4	-	-
9	2839.61	2843.42	23	22	3	21	8	19	4	-	-
10	2839.8	2843.61	20	18	2	24	9	22	3	-	1
11	2840.27	2844.08	15	27	3	16	7	29	2	-	-

Table 4.2 XRD bulk mineralogy analysis result shows the increase in albite and mica content in clayey fine sample in expense of quartz.

Sample No	Log-depth	Quartz (%)	Albite (%)	Orthoclase (%)	Biotite (%)	Muscovite (%)	Rock Fragments (%)	Organic Matter (%)	Chlorite (%)	Smectite (%)
3	2840.86	20.667	23	2.333	12	3.333	12.333	2.667	5	18.667
7	2841.99	18.667	21.333	2.667	11	6.333	4.333	3.667	7.667	24.333
11	2844.08	19.667	13.667	4.333	7.333	4.667	4.333	2.333	4.667	39

Table 4.3 Summary table of point count results from three thin sections. It shows the percentage of the minerals that comprise the rocks. Sample 3 has the most reliable mineral estimation because it is coarse grained and homogeneous.

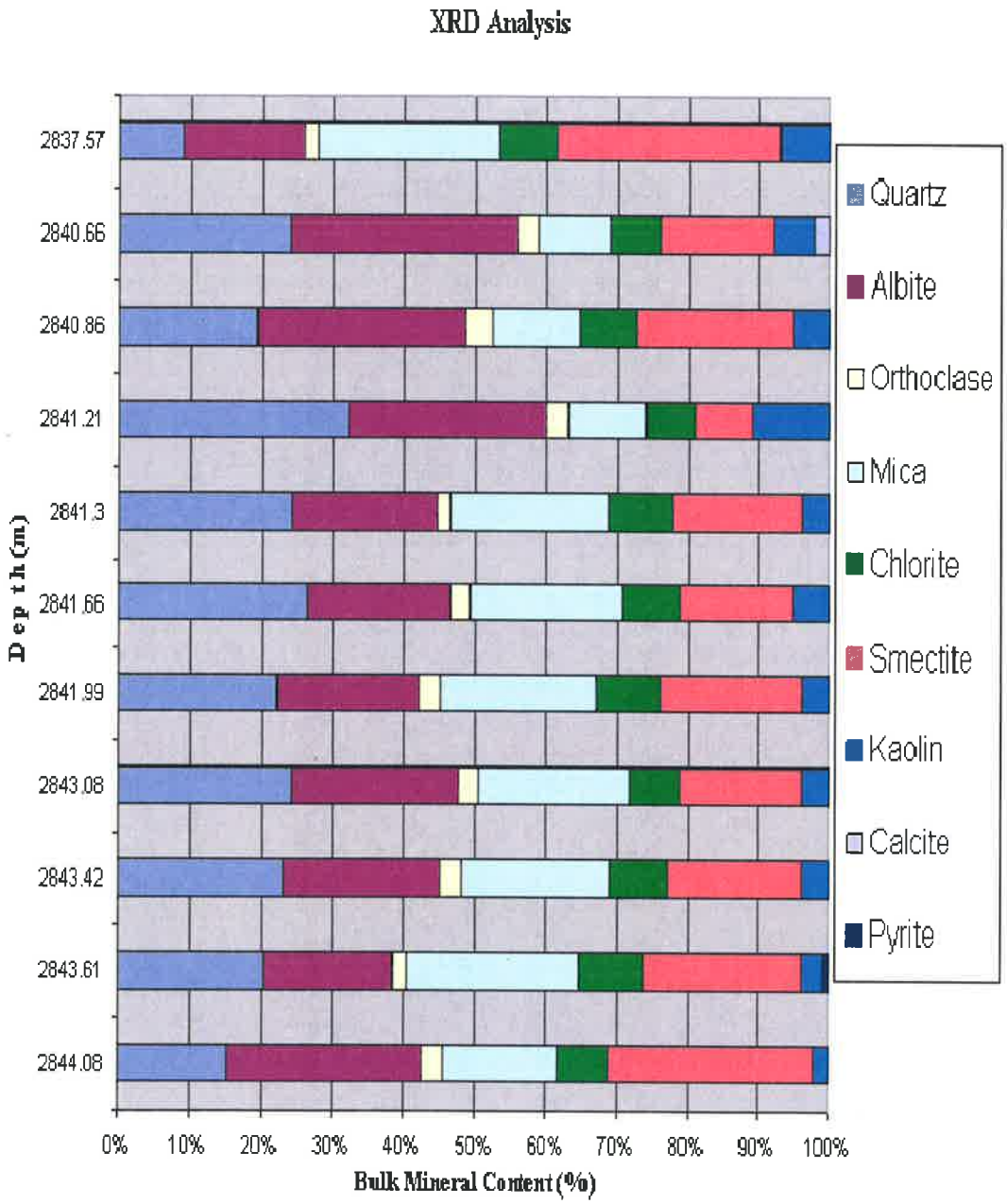

Figure 4.3: XRD bulk mineralogy content versus depth

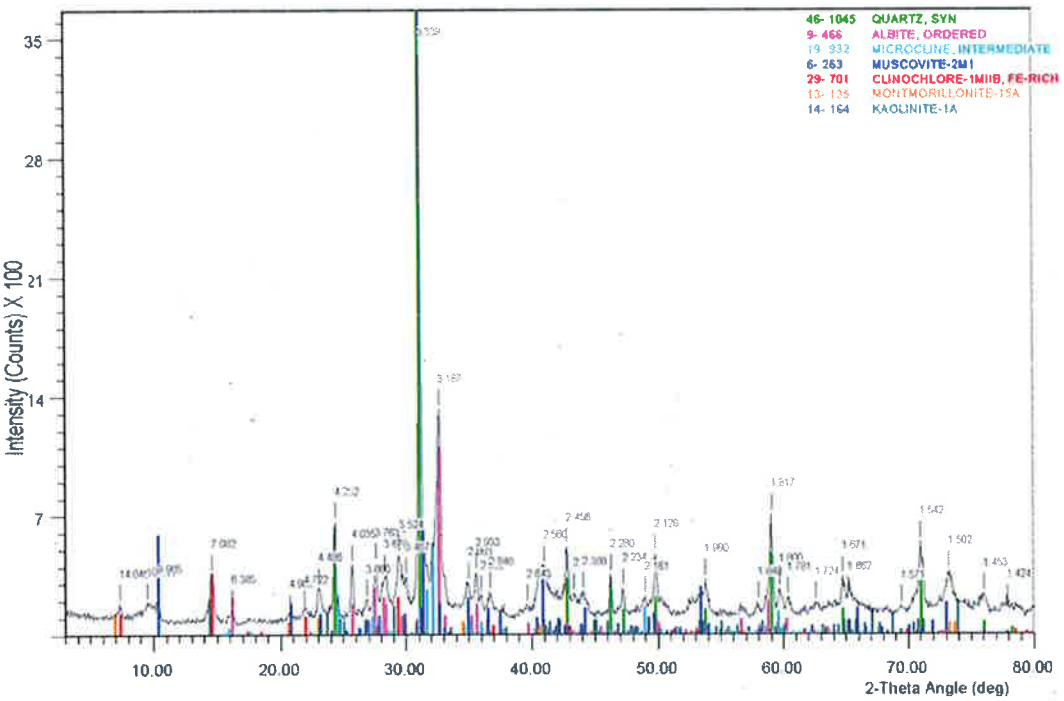

Figure 4.4 XRD trace showing the main minerals that make-up this sample: quartz, albite, microcline, mica, clays and chlorite. Quartz has the highest intensity in this sample, >3500 counts. Redman-1, Sample 3 (2840.86m).

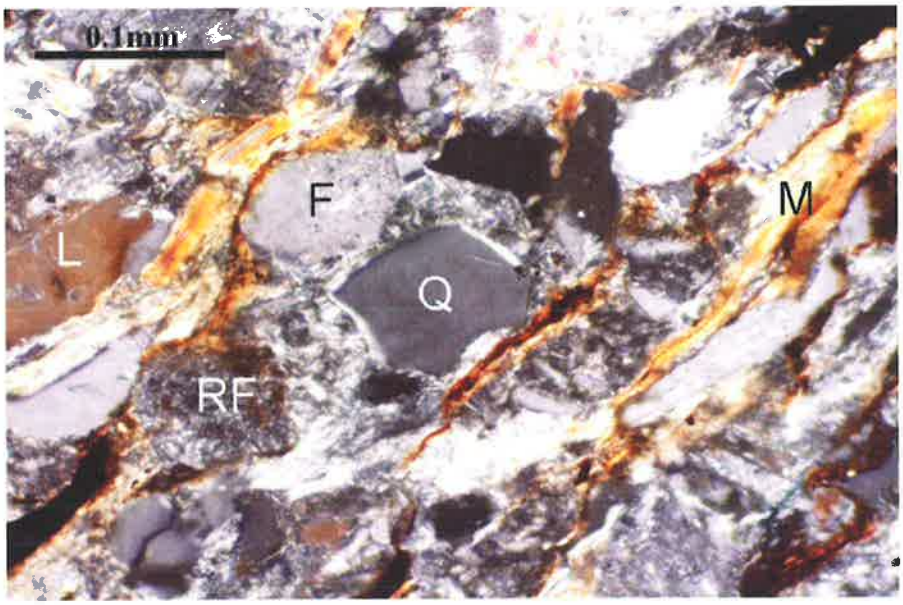

Figure 4.5 Cross polarized photomicrograph of the dominant minerals in the 11 samples: detrital quartz (Q), feldspars (F) mica (M), altered rock fragment to clay (RF) and lithic grains (L). Monocrystalline quartz grain (Q) is the dominant quartz type. Redman-1, Sample 3 (2840.86m).

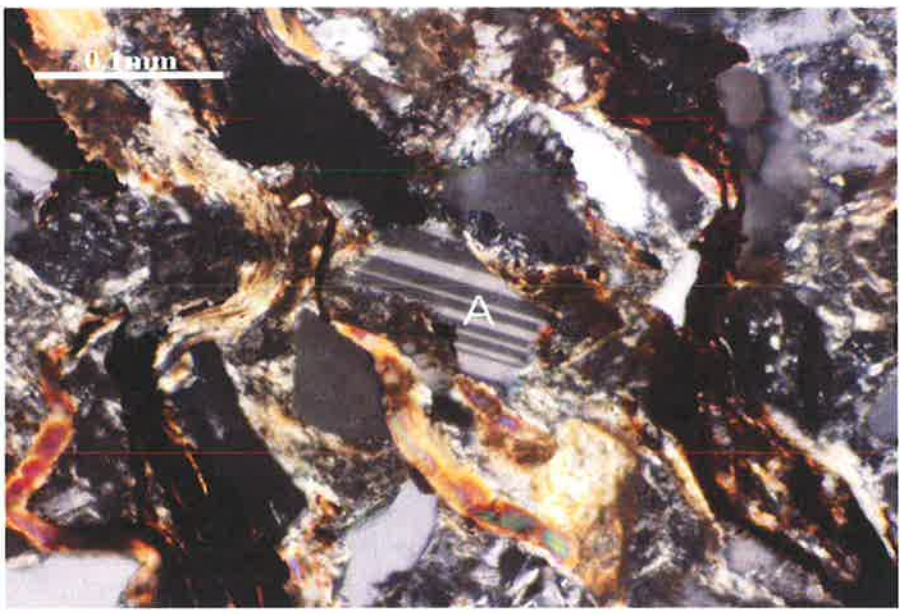

Figure 4.6 Cross polarized photomicrograph of Na-Plagioclase (albite) grain with parallel twining (A). Albite is the dominant type of feldspar in the samples. Redman-1, Sample 3 (2840.86m).

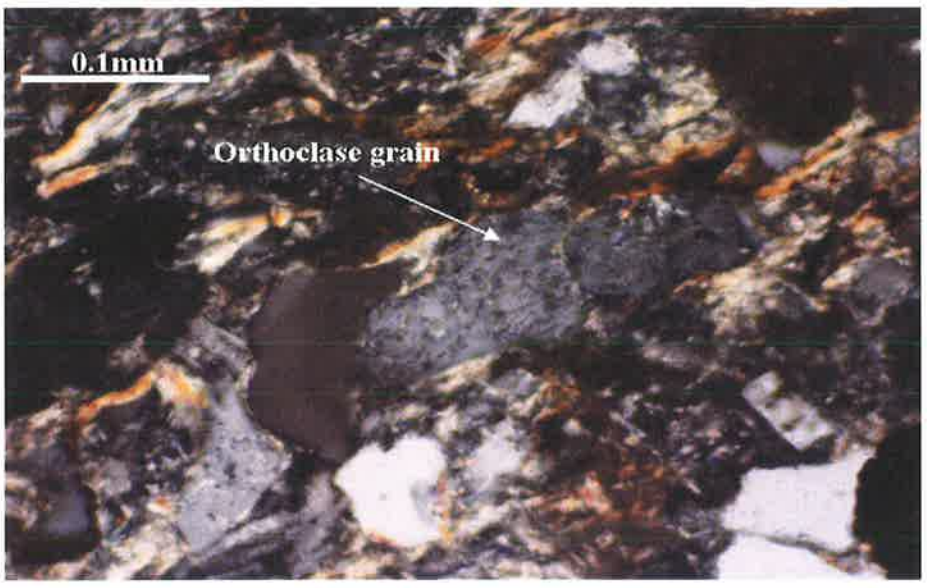

Figure 4.7 Cross polarized photomicrograph of K-feldspar (orthoclase) grain which appears to be altered during digenesis-partial. Albitization is likely based on Na-plagioclase inclusions within the grain. Redman-1, Sample 3 (2840.86m).

4.2.3 Mica

XRD results indicate that mica forms between 10 - 26 % of the total mineralogy. Mica content increases when the grain size decreases along with the quartz and feldspar content. Point counting (Table 4.3) was done on the thin sections to determine the percentage of different minerals with emphasis on biotite to muscovite ratio. The XRD results did not identify biotite whereas the biotite was more common than muscovite in thin sections (Table 4.3, Appendix-C and Appendix-D).

The discrepancy in the biotite concentration is probably due to diagenetic alteration which would not have given sharp classical biotite peaks. A reason for the discrepancy between the XRD and the point counting results is that there was overlap in the XRD of the muscovite and biotite peaks and they were grouped. The biotites have also been altered by diagenesis, its birefringence is altered, and in some cases the graines are partially chloritized. Knowing the biotite percentage is important for the objective of this study, point counting was performed although it was quite difficult in fine grain rocks.

Biotites are two to three times the muscovite percentages calculated by point counting (Table 4.3; Figure 4.8). Sample 3 (2840.86m) is the best sample to obtain reliable mineral estimations from point counting because Sample 7 (2841.99m) is clayey siltstone (hard to count) whereas Sample 11 (2844.08m) is heterolithic sandstone-siltstone.

Biotite ranges from slightly to highly altered. Biotite flakes have been squeezed between the quartz and feldspar grains and their orientation is an indication of the compaction direction and magnitude. It has significant iron content which is likely to affect NMR response (discussed in chapter 6.2). Distorted mica grains were observed in the samples indicating deformation via compaction (Figure 4.9). Muscovite is present as finer

grains and as elongated flakes which were deposited in the same bedding direction (Figure 4.10).

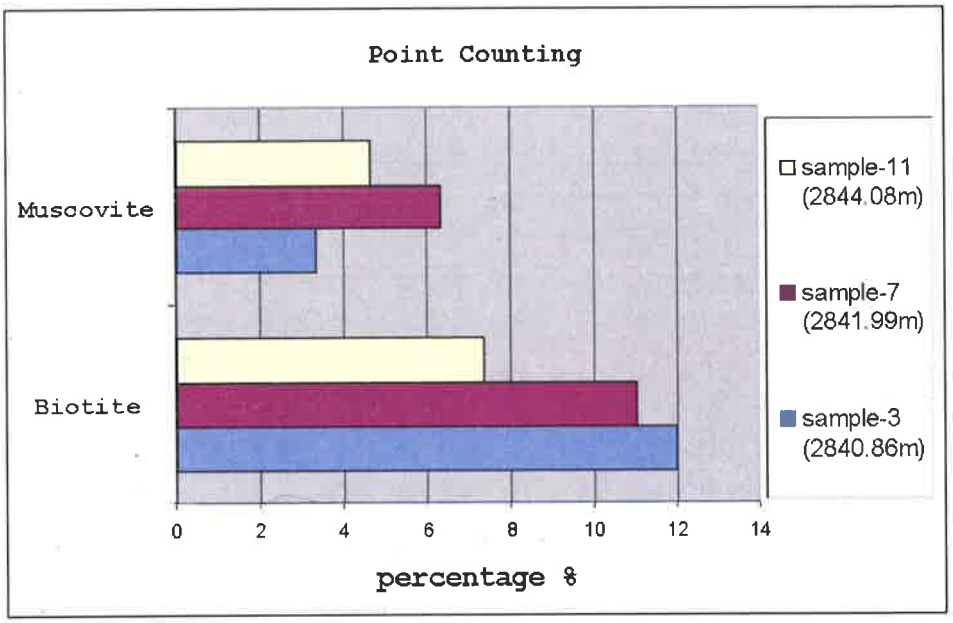

Figure 4.8 The percentage of biotite and muscovite using point counting on thin sections. Biotite is twice or three times muscovite content.

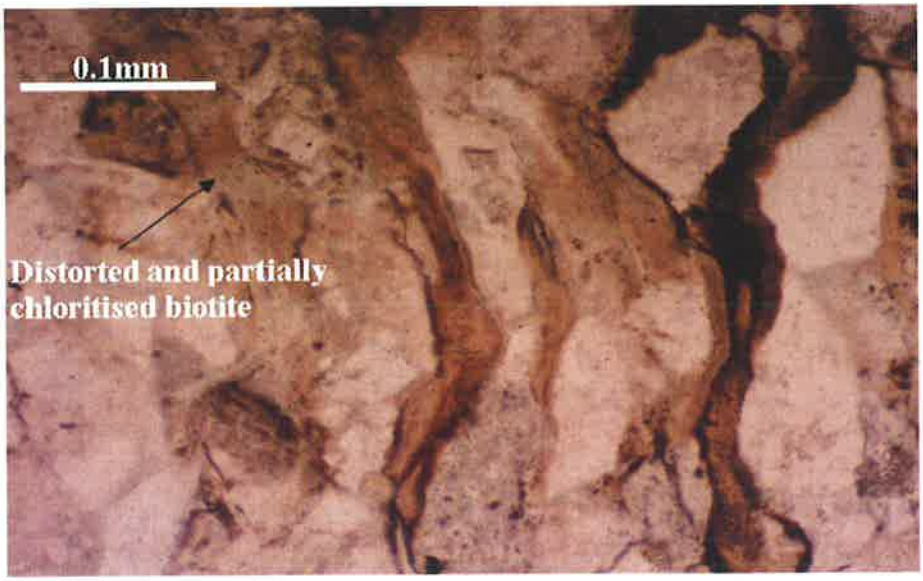

Figure 4.9 Plane polarized photomicrograph of deformed and altered biotite flakes deposited in the bedding direction and every flake has different levels of alteration. The pale green color increases as the chloritisation increases. Redman-1, Sample 3 (2840.86m).

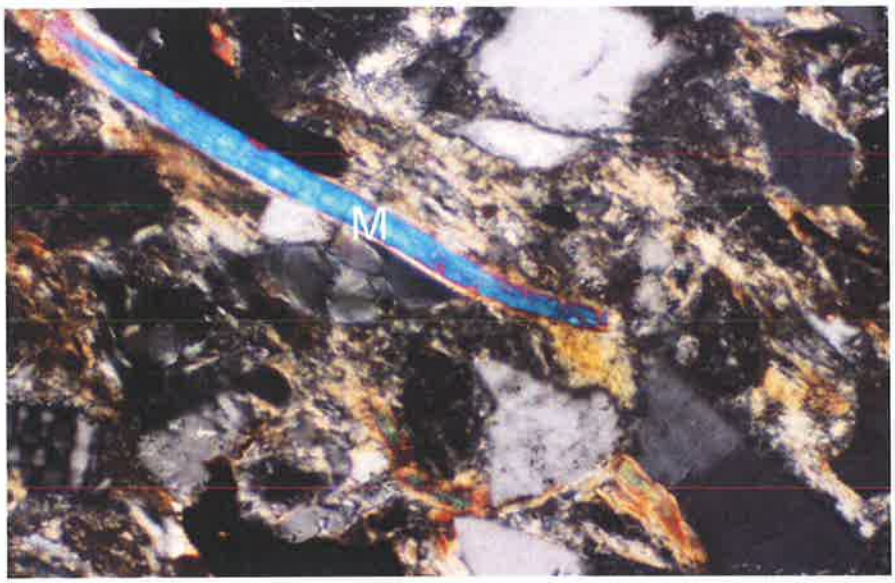

Figure 4.10 Cross polarized photomicrograph of muscovite (M) elongated grain deposited in the same bedding direction. Redman-1, Sample 3 (2840.86m).

4.2.4 Clays

Smectite, chlorite and kaolin are the main clay types which were identified using XRD analysis within the interval (Figure 4.3). Smectite is the most abundant clay type with concentration between 16 and 32 % of the total bulk volume. Kaolin comprises between 2 and 11 percent while the chlorite (discussed further in chapter 4.4) is between 7 and 9 percent. The increase in the total clay content indicates the low energy environment.

Smectite is a swelling clay which might reduce porosity, therefore; care was taken in sample handling to preserve the original pore volume was examined using SEM (Figure 4.11). Kaolin was not seen in SEM because it occurs in lower concentration in very fine grained rock. Kaolin can form as a product of feldspar dissolution. Porosity and permeability would not be greatly affected by increasing the kaolin percentage.

4.2.5 Lithic Grains

The very fine grained rocks of the Pretty Hill Formation have a significant amount of lithic grains. Point counting indicates 4 to 13 percent lithics in siltstone to very fine sandstone. Thirteen percent is probably a more reliable estimation because it was done on very fine sandstone thin section and the altered nature of the lithic grains can make them hard to identify. Little and Philips (1995) reported that the origin of lithics in the Pretty Hill Formation are igneous, metamorphic and sedimentary rocks (Figure 4.12). However, rock fragments of sedimentary origin were not observed in the three thin sections examined.

Rock fragments are commonly chemically unstable grains and highly altered. These unstable grains produce many authigenic minerals through extensive diagenesis, particularly chlorite. Also, rock fragments are affected by compaction which changes the grain shape to produce low permeability pseudo-matrix with indistinct grain boundaries (Figure 4.13).

4.2.6 Accessory Minerals

Garnet occurs in minor amounts in the fine grained rock interval of the Pretty Hill Formation. It is found as isolated mainly colorless grains locally concentrated in heavy mineral-rich bands (Figure 4.14). Garnet has high relief boundaries with no cleavage and the colours vary slightly based on the chemical composition. The garnets have a high grade metamorphic origin based on high Mg contents (Tingate, 2005, personal communication).

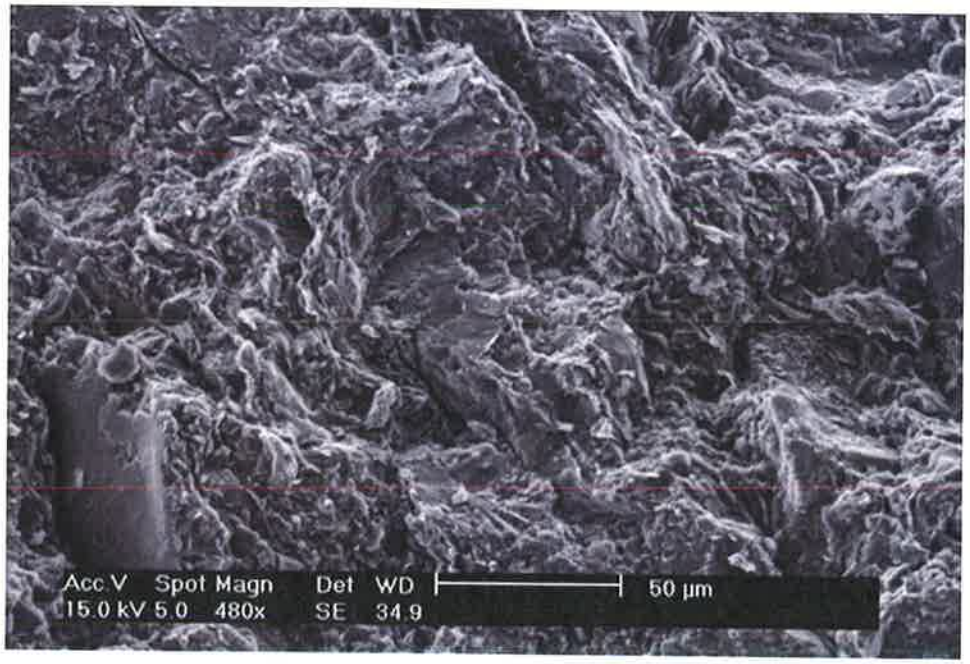

Figure 4.11 SEM image of smectitic clay that cover most of the grains and occludes the pore system. Redman-1. Sample 9 (2843.42m).

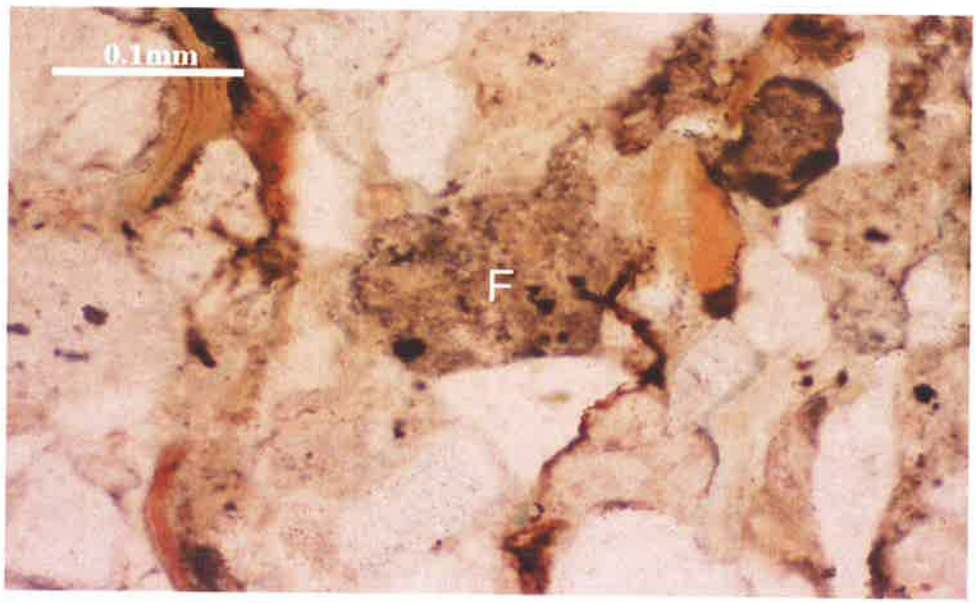

Figure 4.12 Plane polarized photomicrograph of rock fragment (F) which is partially altered to authigenic clay. Redman-1, Sample 3 (2840.86m).

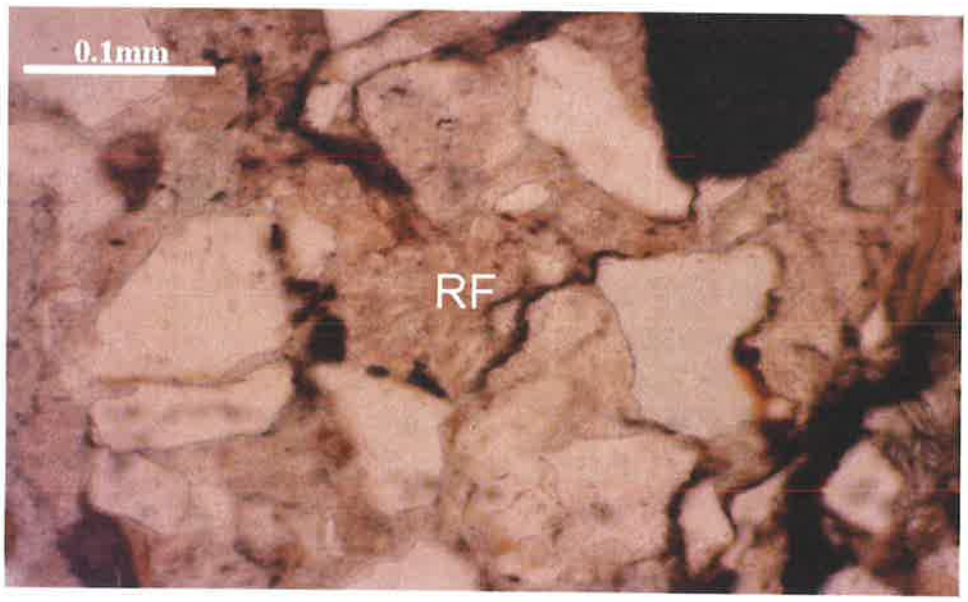

Figure 4.13 Plane polarized photomicrograph of deformed and altered rock fragment grain (RF) with no clear boundaries due to the compaction process. Redman-1, Sample 3 (2840.86m).

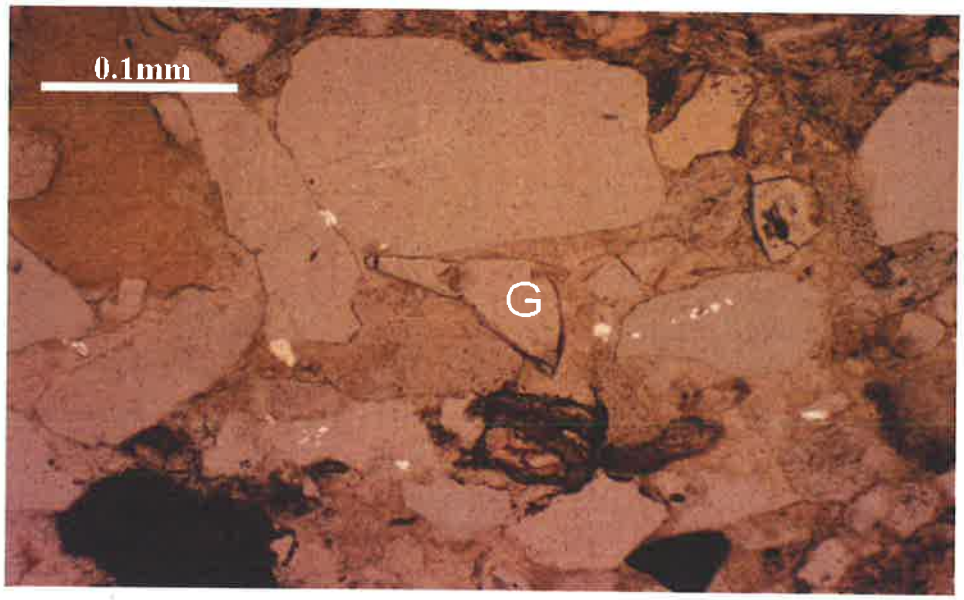

Figure 4.14 plane polarized photomicrograph of garnet grain (G) with high relief boundaries. Garnets exist throughout the Pretty Hill Formation and indicate a high grade metamorphic source. Redman-1, Sample 3 (2840.86m).

4.3 Authigenic Minerals

The most abundant authigenic minerals in the fine grained rocks of the Petty Hill Formation are chlorite and laumontite. Laumontite is significant only in one sample (Sample 11), a fine sandstone with poor reservoir quality.

4.3.1 Chlorite

Chlorite is an abundant authigenic mineral in the Pretty Hill Formation (Little, 1996). The chlorite concentration in the very fine grained interval ranges between 7 and 9 percent (XRD analysis). The chlorite content is considered constant throughout the flood plain facies (no major changes). Under the microscope, it is pale green to brown color (Figure 4.9). The chlorite is iron rich as determined from XRD analysis (Appendix-C).

The chlorite occurs as replacement of volcanic lithics in the Pretty Hill Formation. The high iron content in diagenetic chlorite was recognized by Little and Philips (1995) and they proposed a second possible origin related to biotite alteration.

4.3.2 Laumontite

Laumontite is a calcium rich zeolite which precipitates as a white pore filling cement (Figure 4.15) associated with albitization of feldspars. This authigenic mineral only exits in a fine sandstone (Sample 11 (2844.08m)) mixed with fine siltstone clasts, which occur in the poor reservoir quality rocks. Laumontite is a common authigenic mineral in the reservoir interval in the Pretty Hill Formation (Little, 1996).

The high laumontite content in the reservoir section is likely to be due to the original presence of calcic plagioclase. The laumontite formed during

the albitization process which altered the calcium bearing-plagioclase to Na-plagioclase (albite). The calcium released during this reaction formed laumontite as pore filling cement.

4.3.3 Diagenetic Accessory Minerals

Calcite and pyrite occur as minor components in the samples analyzed. Calcite was recognized using XRD analysis in Sample 2 (2840.66m), where it comprises 2 percent. Calcite occurs as a replacement product of other grains and authigenic minerals in the Pretty Hill Formation. Calcite exists in the fine-medium sandstone, Sample 2 (2840.66m) which has poor reservoir quality. The occurrence of carbonates in the reservoir section in the Penola Trough area was also reported by Little & Phillips (1995).

Pyrite was indicated by XRD only in one sample (Sample 10, 2843.61m) comprising 1 percent in XRD, but was also identified in thin section (Sample 3, Figure 4.16). Pyrite occurs as cubes or octahedrons and is commonly associated with organic matter.

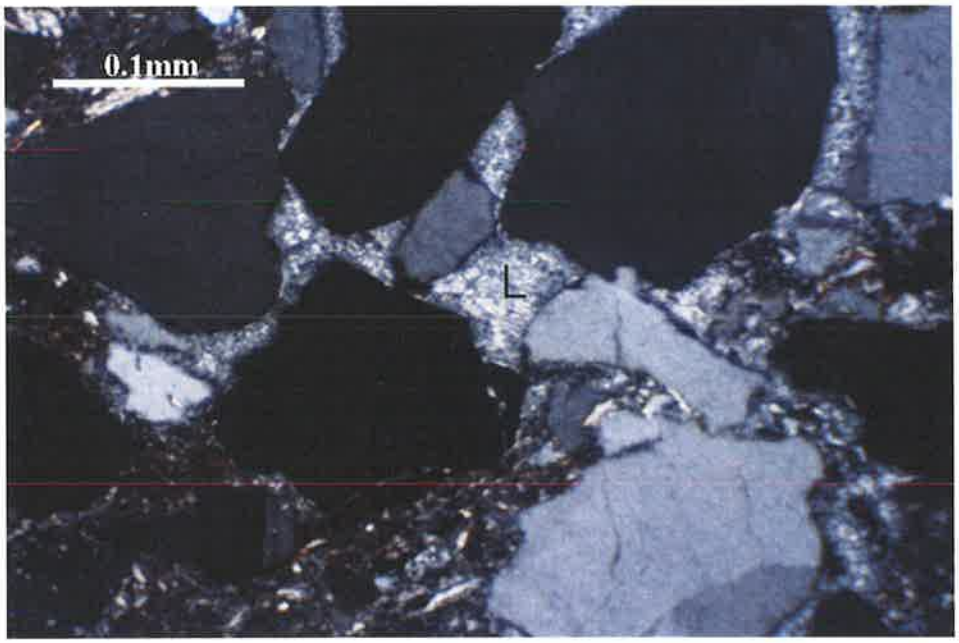

Figure 4.15 Cross polarized photomicrograph of authigenic laumontite which occurs as a white pore filling cement (L). Laumotite is a cement commonly associated with albitization of plagioclase in the Otway Group. Redman-1, Sample 11 (2844.08m).

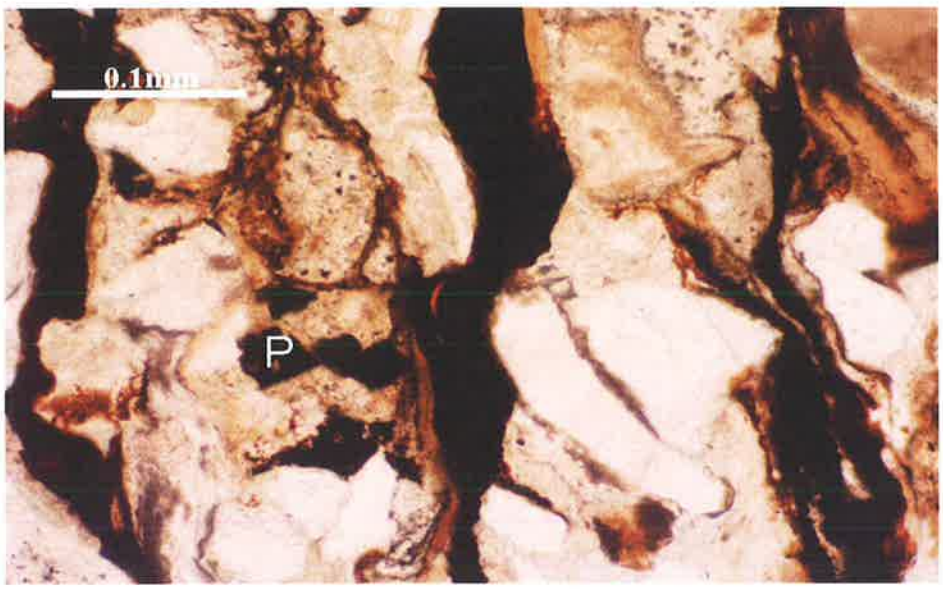

Figure 4.16 Plane polarized photomicrograph of opaque pyrite crystals (P), associated with organic matter. Redman-1, Sample 3 (2840.86m).

CHAPTER FIVE
PETROPHYSICAL PROPETIES DETERMINATION

5.1 Introduction

Petrophysical properties of the rocks in this study were determined using different analytical techniques. The laboratory techniques include porosity and permeability analyses, mercury injection capillary pressure (MICP), scanning electron microscopic (SEM) and porecast. Nuclear magnetic resonance (NMR) was also used to provide information on porosity, permeability and pore geometry.

This chapter starts with the laboratory and log porosity and permeability measurements and illustrates which one is more reliable in fine grained lithologies. Then, capillary pressure and pore throat size data are used to describe the pore system in the flood plain facies, supported by SEM observation. NMR data processing and pseudo capillary pressures are then outlined. Finally, displacement pressures are estimated from the pseudo capillary pressure curve at different percentages.

5.2 Porosity and Permeability Estimation

Porosity was measured using both laboratory analyses and logging tools. In the laboratory, core plug porosity was measured by helium and also calculated using mercury injection capillary pressure. Density, neutron and Schlumberger's combinable magnetic resonance (CMR-200) tools (porosity logs) were run in Redman-1. Comparisons between the results of laboratory and log porosity measurements are illustrated in Figure 5.1. MICP porosity has a good correlation with density and total CMR porosity except Sample 8 (2843.08m) which has micro fractures. Helium porosity has excellent

match with the effective CMR porosity in the flood plain facies. The neutron porosity log is not reliable in such lithologies and can give higher or lower measured hydrogen content.

Total CMR porosity ranges between 1.1% and 9.2% in the siltstone-clayey siltstone interval (the good seal lithology). The only exception is Sample 8 (2843.08m) which has a micro fractures that affect the porosity measurement. Porosity increases more than 9.2% in the very fine sandstone which represent poor reservoir quality (Figure 5.1). Effective CMR porosity is much lower than total CMR porosity which characterizes the very fine grained lithology. The difference between total and effective porosity decreases over the very fine sandstone interval. Effective CMR porosity ranges between 0.12% and 2% in siltstone-clayey siltstone samples.

Permeability was calculated by using the mean T2 model (SDR) from the CMR tool. It ranges between 0.001 and 0.00006md in the siltstone-clayey siltstone interval. This suggests a good seal lithology. Permeability increases when the lithology becomes more sandy (Figure 5.2). The laboratory measurements for permeability were not reliable and therefore they are not included for further interpretation (Appendix-D). The results were too high to be accepted as siltstone-clayey siltstone permeability and this might be due to alteration of *in situ* conditions or core handling artifacts, these samples can be easily fractured. If core plugs have received fractures, permeability values increase significantly.

From the available effective porosity and permeability data, the flood plain facies is interpreted as very tight. Since smaller pore and throat sizes have better sealing potential, these flood plain samples are potentially good seals.

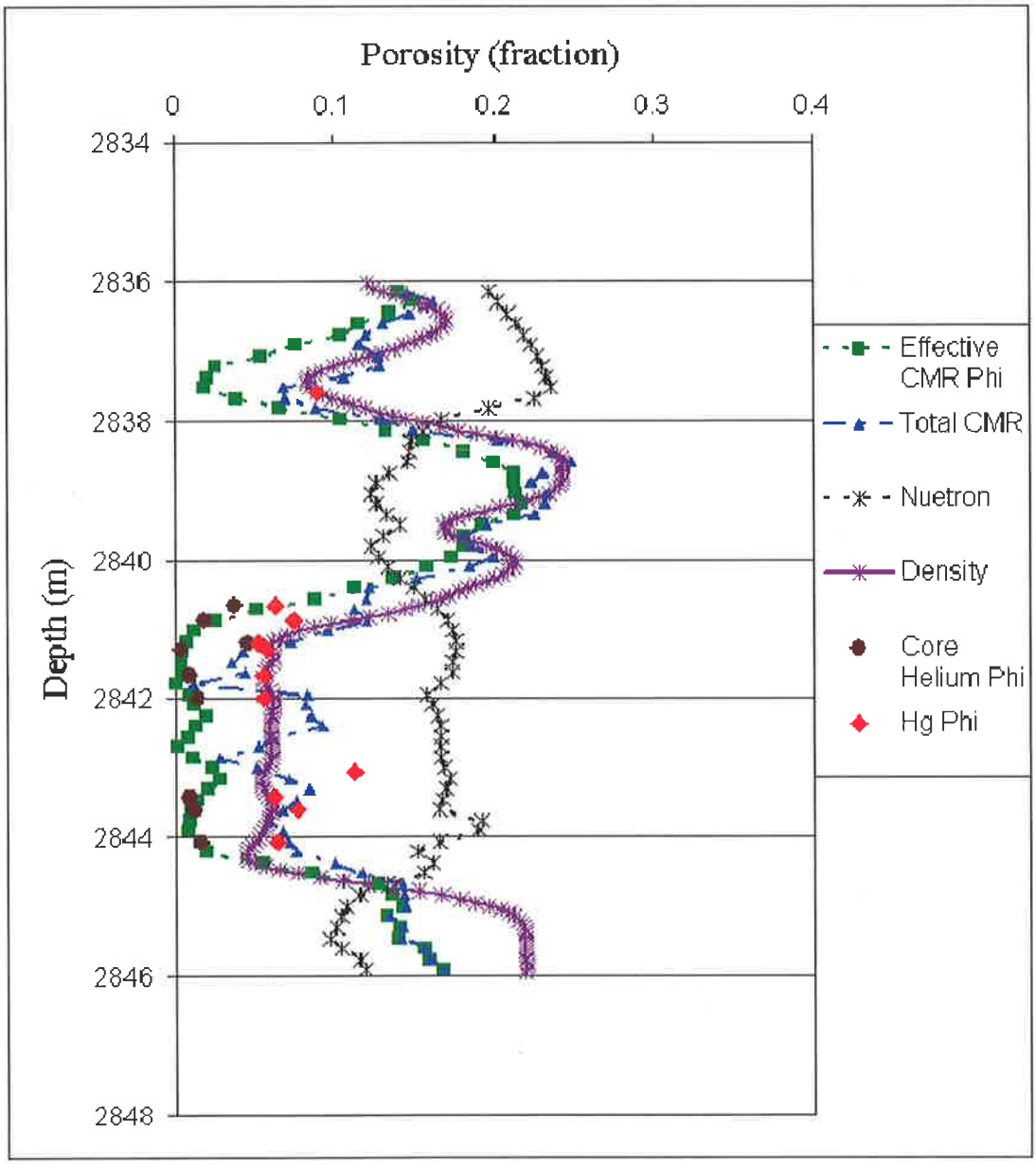

Figure 5.1 Different porosity measurements (from Lab & Logs). CMR total porosity has similar estimation of MICP porosity and density while the effective CMR porosity gives a good match to core helium porosity. Effective CMR porosity, linked to fluid movement, ranges between 0.12% and 2% in siltstone-clayey siltstone samples.

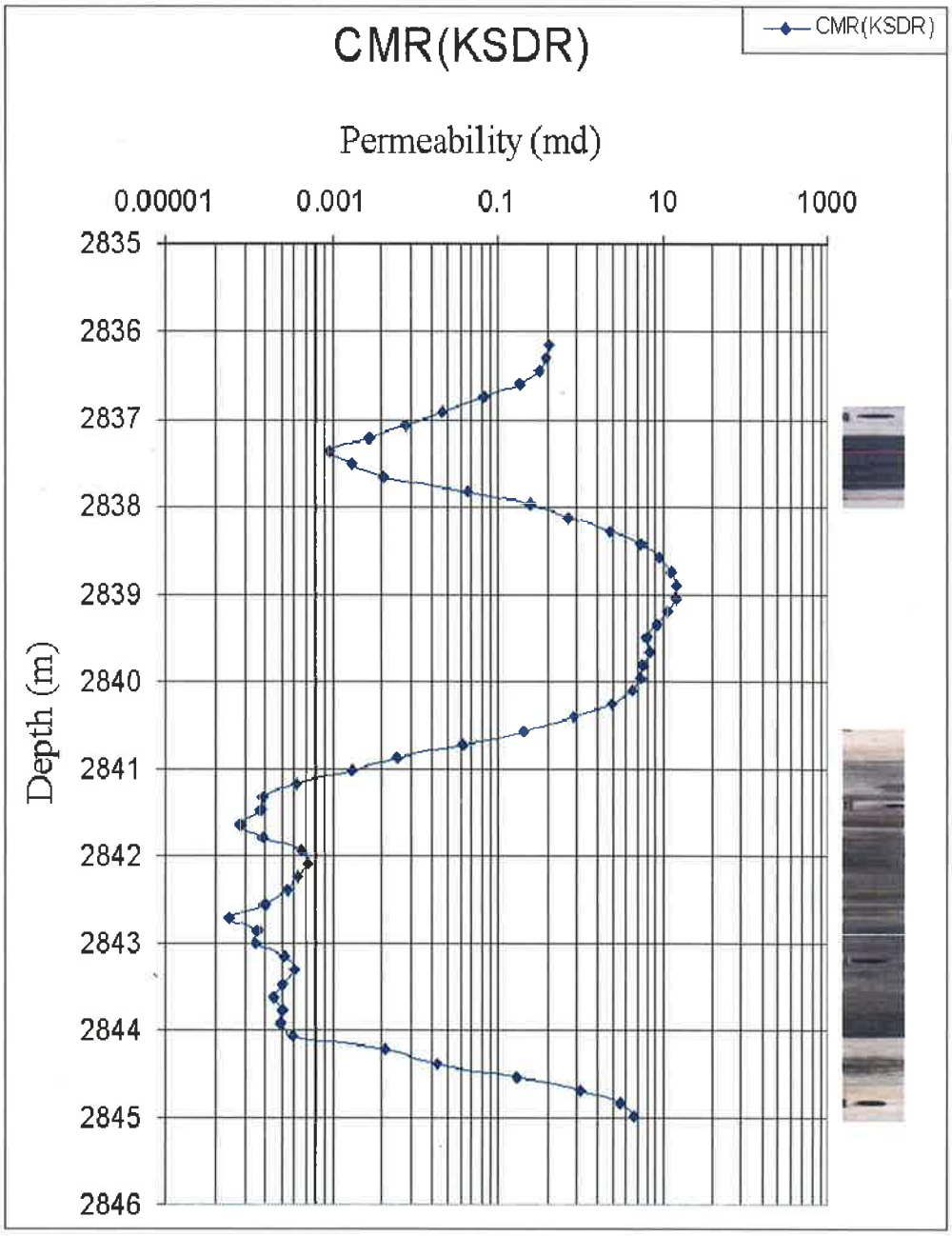

Figure 5.2 Permeability estimation of flood plain facies ranges between 0.001 and 0.00006md in the siltstone-clayey siltstone interval.

5.3 Capillary Pressure and Pore Throat Size Determination

Mercury injection capillary pressure (MICP) is the primary tool to measure capillarity. Pressure is applied up to 60,000 psi which enables mercury to enter extremely small pores, including seal lithologies. For all samples, conformance (closure) effect was corrected before applying raw data to any calibration. Also, data were converted to reservoir condition (hydrocarbon/brine system) as described in chapter 3.

Mercury/air displacement pressure of Redman-1 samples range between 200 and 500 psi in the good seal lithology (Figure 5.3). In the poor seal lithology, displacement pressures range between 50 and 200 psi (Figure 5.4). All of the Redman-1 flood plain samples have broad pore throat size distribution showing no bimodal or trimodal distributions. Sample 8 (2843.08m) has micro fractures which cause the early breakthrough in the MICP curve. All the MICP data and graphs are attached in appendix A.

The pore throat size of good seal lithologies in Redman-1 samples ranges between 0.004 and 0.7 microns with median pore throat size around 0.0075 microns (Figure 5.5). Poor seal lithology sample have pore throat sizes that range between 0.005 and 1 microns with a median pore throat size around 0.015 microns (Figure 5.6). Also, Sample 8 (2843.08m) has a higher median pore throat size than expected due to micro fractures.

Decreasing pore throat sizes means a more restricted pore system which increases displacement pressure and sealing potential. Redman-1 samples were chosen in both good and poor seal intervals. Therefore, samples which have more siltstone and clay are more likely to be better seals while the increase of sand grains results in poorer seals. The MICP measurement for Sample 8 (2843.08m) was affected by micro fractures.

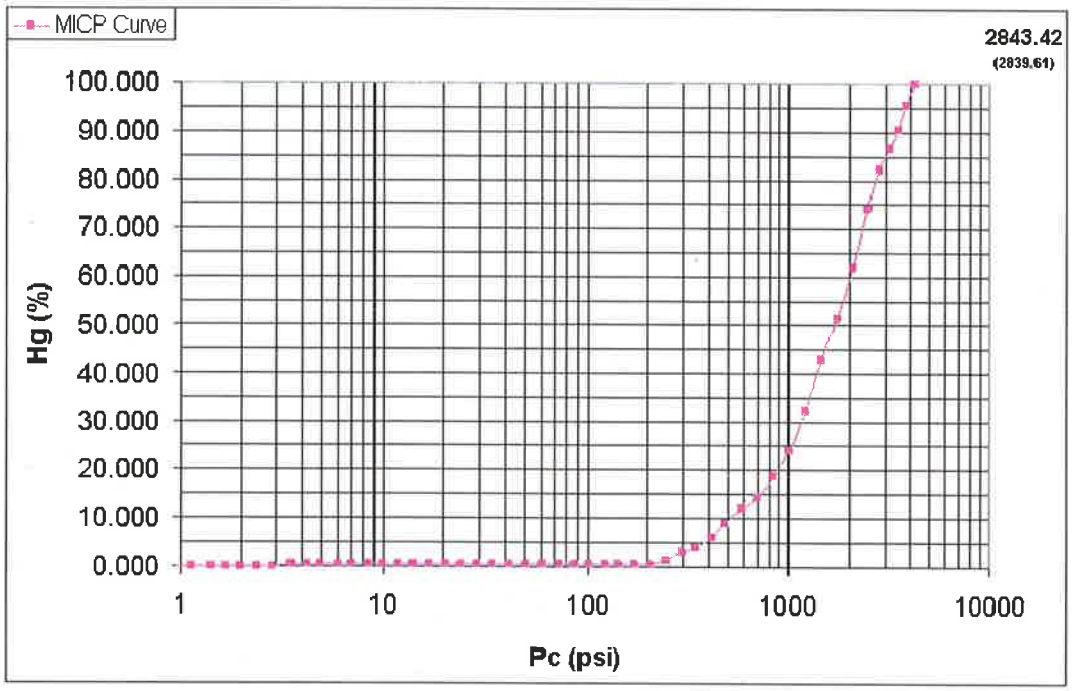

Figure 5.3 Mercury injection capillary pressure (MICP) curve of a good seal lithology sample in Redman-1. Displacement pressure is around 400 psi. Redman-1, Sample 9.

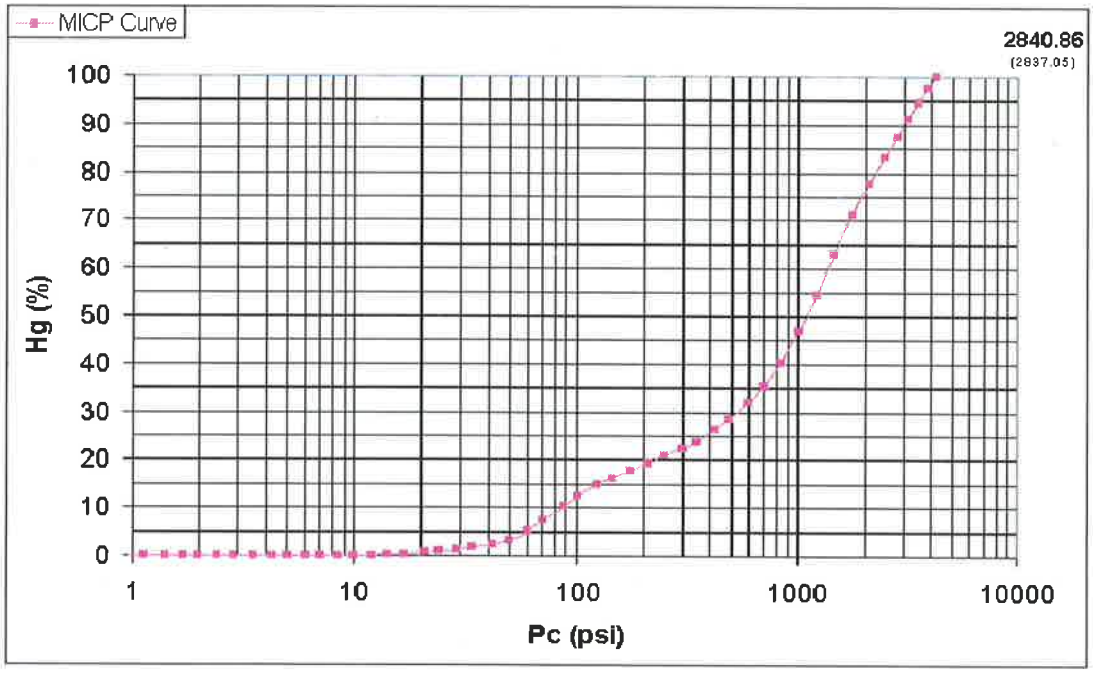

Figure 5.4 Mercury injection capillary pressure (MICP) curve of poor seal lithology sample in Redman-1. Displacement pressure is around 50 psi. Redman-1, Sample 3.

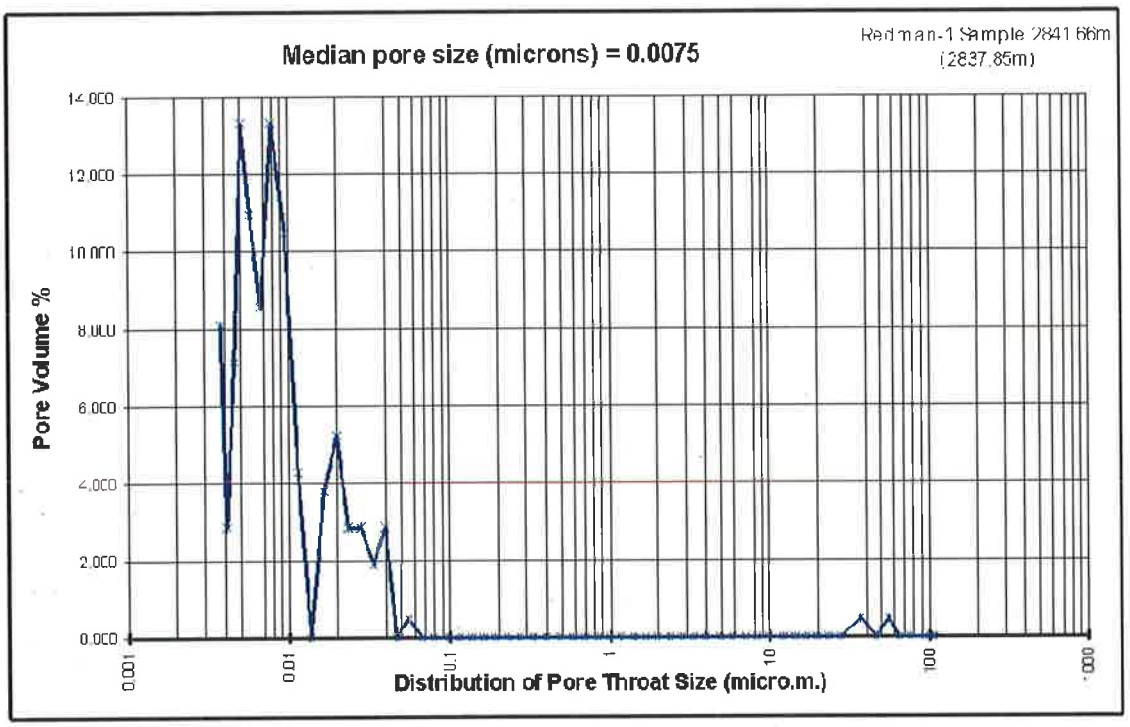

Figure 5.5 Pore throat size distribution in good seal lithology. Median pore throat size is 0.0075microns. Redman-1, Sample 6.

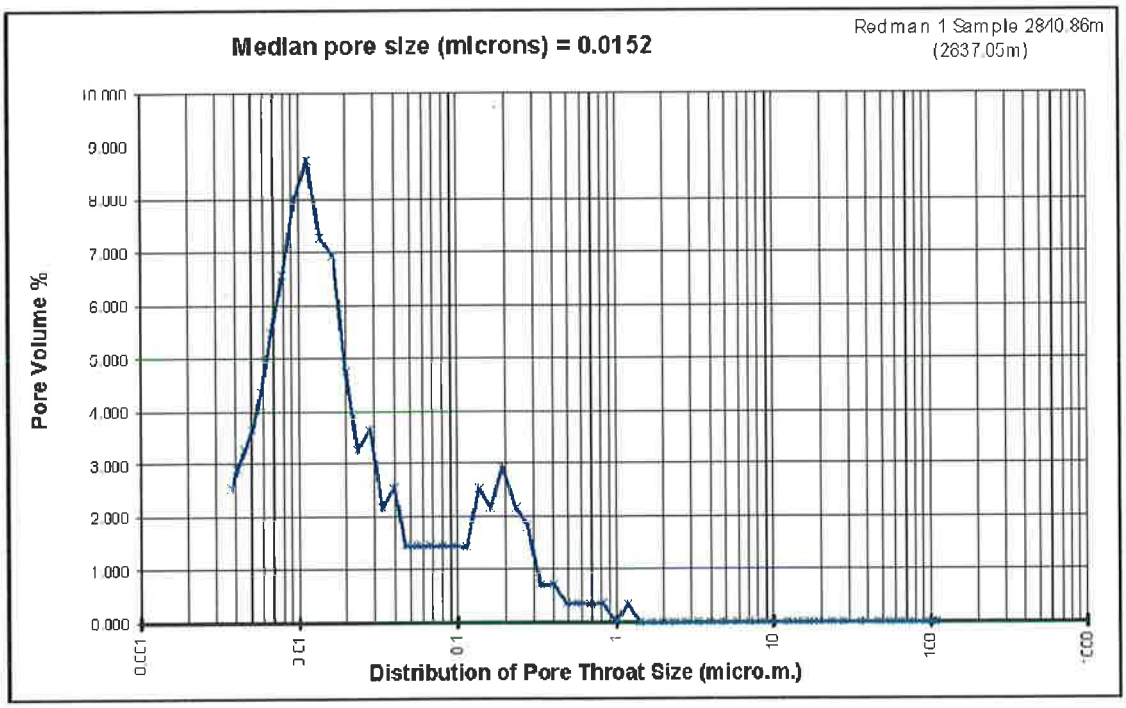

Figure 5.6 Pore throat size distribution in poor seal lithology. Median pore throat size is 0.0152microns. Redman-1, Sample 3.

5.4 T2 Distribution Processing

Nuclear magnetic resonance (NMR) at Redman-1 well was processed in GeoFrame using different stacking levels. One, three and five stacking levels were used. Increasing stacking level increases the signal to noise ratio at the expense of vertical resolution. The CMR tool acquired rolling average readings, with readings every 3.6 inches (9.14 cm). The output value was averaged with the previous and the following readings when the stacking level was greater than one (Figure 5.7).

One, three and five averaging levels of T2 distribution were converted to ASCII files from GeoFrame. All the incremental curves were displayed as incremental T2 distribution for comparison of results. The signal to noise ratio increases and is more consistent when the stacking level increases (Figure 5.8 A-C). The NMR tool usually has high level of noise in very fine grained rocks which might broadens T2 distribution. Therefore, stacking level of five was chosen in the calibration to MICP curve in this study.

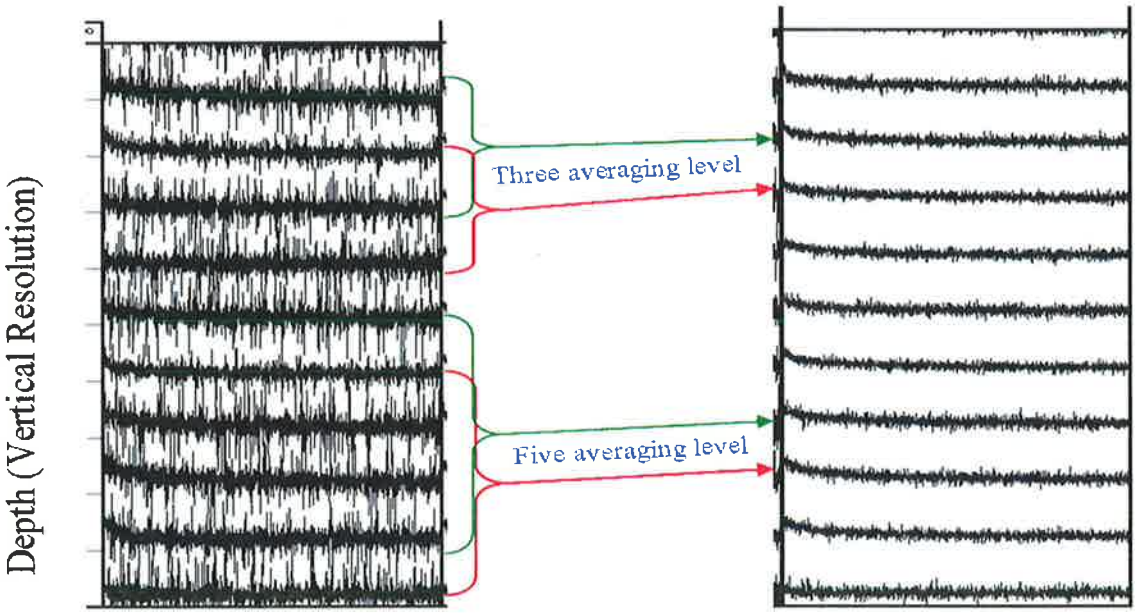

Figure 5.7 Illustration of different stacking levels (one, three and five) were used in CMR data processing

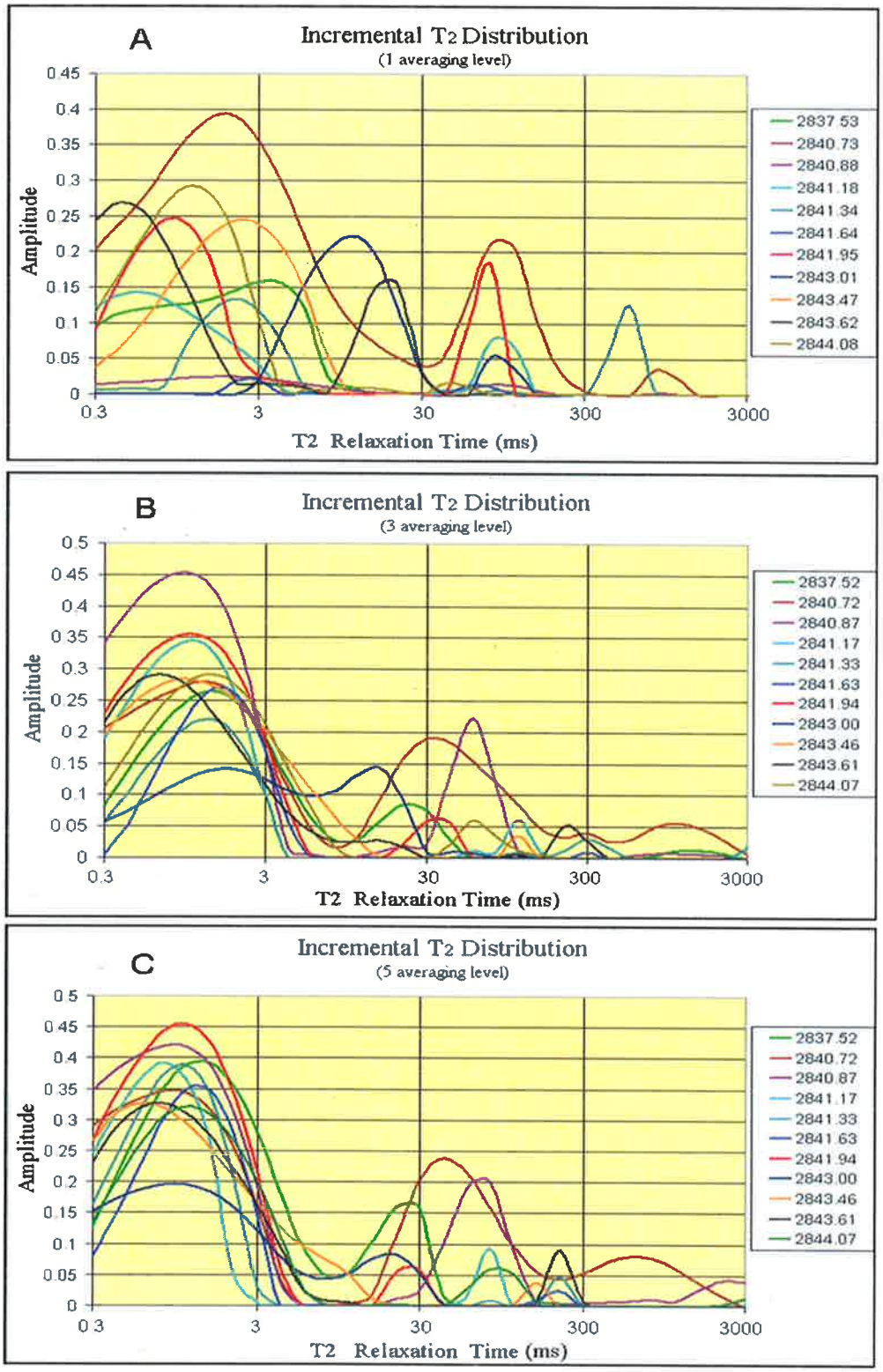

Figure 5.8 A-C Incremental T2 distributions of different depth intervals for every stacking level (one, three and five). Signal to noise ratio increases with increasing stacking level.

5.5 T_2 Pseudo Capillary Pressure Curves

The standard T2 distribution was displayed as an incremental distribution while mercury injection capillary pressure (MICP) was displayed as a cumulative distribution. Therefore, the T2 incremental distribution was converted to a cumulative distribution before any adjustment was made to the relaxation time or amplitude. Then, clay bound water which exists on the surface and within the structure of the clay aggregates was taken out of the cumulative T2 distribution. Finally, the two T2 curve axes, relaxation time and amplitude, were converted to capillary pressure and water saturation respectively.

5.5.1 Corrected Cumulative T2 Distribution

NMR incremental T2 distributions need some modification to be calibrated to MICP curves. First of all, the incremental T2 distribution was converted to a cumulative distribution by adding the amplitude value for every incremental time to the sum of all previous amplitudes. This process was repeated for every depth interval (Figure 5.9).

The T2 relaxation time responds to the hydrogen content in the pore space of the matrix. Thus, T2 response measures any hydrogen which exists in the effective pore system (e.g. interparticle pores) and also ineffective pore system (e.g. micro porosity and clay bound water). Sandstone reservoir rocks have a small amount of ineffective porosity which might be eliminated by the applied effective relaxivity (scale) factor. The NMR T2 response in seal lithologies (clay-rich rocks) includes the response from fluids between clay aggregates and bound water on clay surfaces (Figure 5.10).

The surface area associated with clays is much larger than any other sediment and the magnitude depends on clay types. Smectite has the

highest surface area and kaolin has the lowest. Consequently, clay bound water in clay-rich rocks contributes significantly to the T2 distribution. Swelling clay, such as the smectite group, has additional storage spaces for brine or water inside the clay structure. The water inside the clay structure might be included in the T2 distribution if it has significant amount of water which could contribute to the relaxation mechanisms. On the other hand, mercury injection capillary pressure (MICP) measures only the effective (connected) pore system of the clay-rich rock. This includes the interaggregate pore system and capillary bound water.

Because of this, the clay bound water content should be removed from the T2 distribution in order to calibrate it to MICP data. This was achieved by subtracting the effective porosity from the total porosity to calculate the clay bound water (CBW) percentage at every depth (Figure 5.11). There is high clay bound water content in all the flood plain samples. The CBW percentage ranges between 53% and 90%, a high portion of the total T2 distribution. The amount of clay bound water porosity can be used to determine the clay bound water portion (amplitude) of T2 distribution by using the following relation (Eq.5.1) for every T2 distribution curve.

$$\text{Clay Bound Water Portion} = \frac{\phi_{CBW} * \sum Amplitude}{100} \qquad \text{(Eq.5.1)}$$

Where,

ϕ_{CBW} = Percentage of the clay bound water porosity

$\sum Amplitude$ = Sum of T2 distribution Amplitudes

To build a cumulative T2 distribution free of the clay bound water, the clay bound water (CBW) amplitude portion was subtracted from every incremental value in the T2 distribution curve (Figure 5.12). That means that every value on cumulative T2 distribution was suppressed by the value of CBW amplitude in each sample.

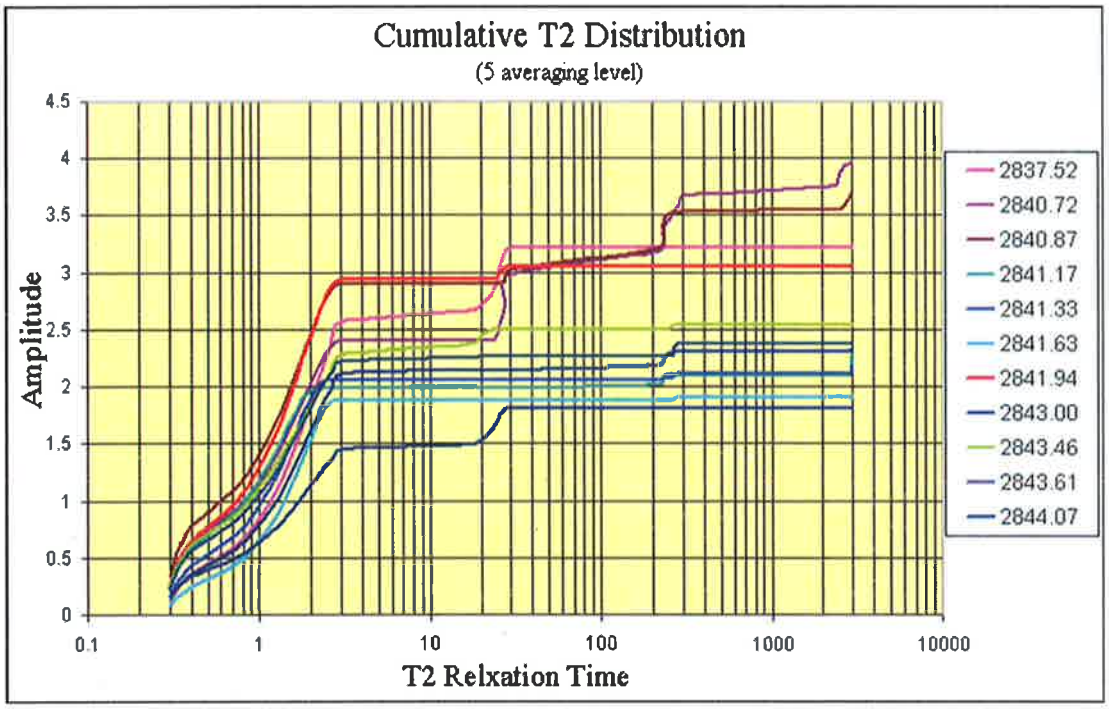

Figure 5.9 Converted cumulative T2 distribution from incremental curves for every depth sample.

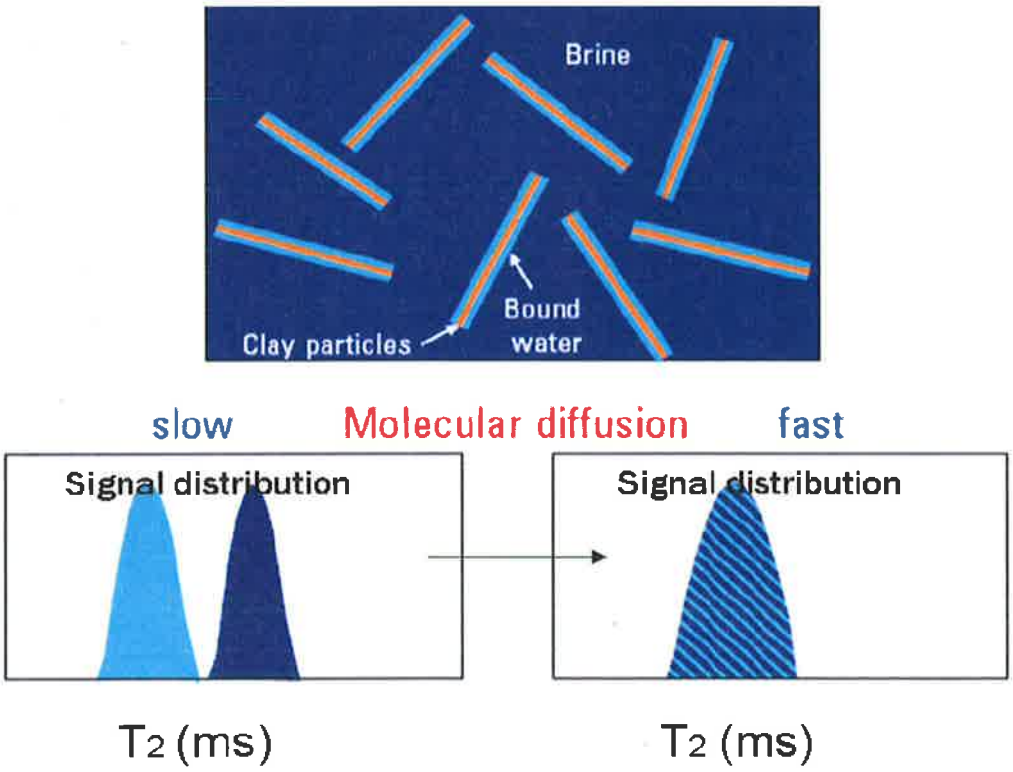

Figure 5.10 T2 distribution is the sum of the fluid content of both interaggregate pores and on the clay surfaces. At normal logging speeds, the logging tool can not differentiate between them.

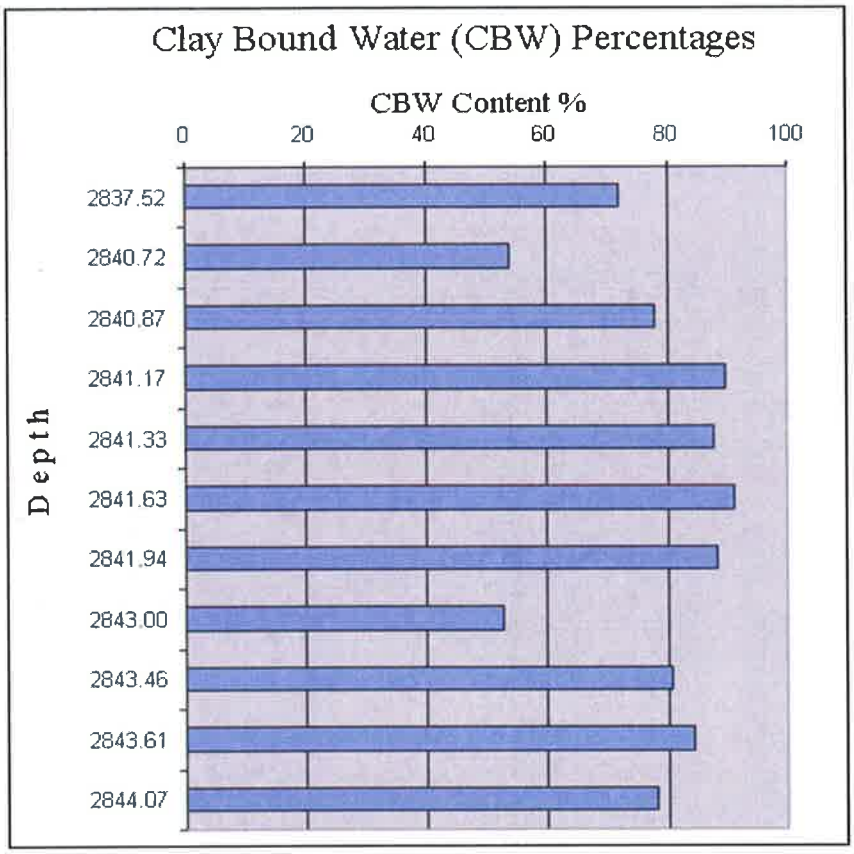

Figure 5.11 Clay bound water content for every depth was calculated by subtracting effective porosity from total porosity. Then, CBW content can be easily taken from T2 response.

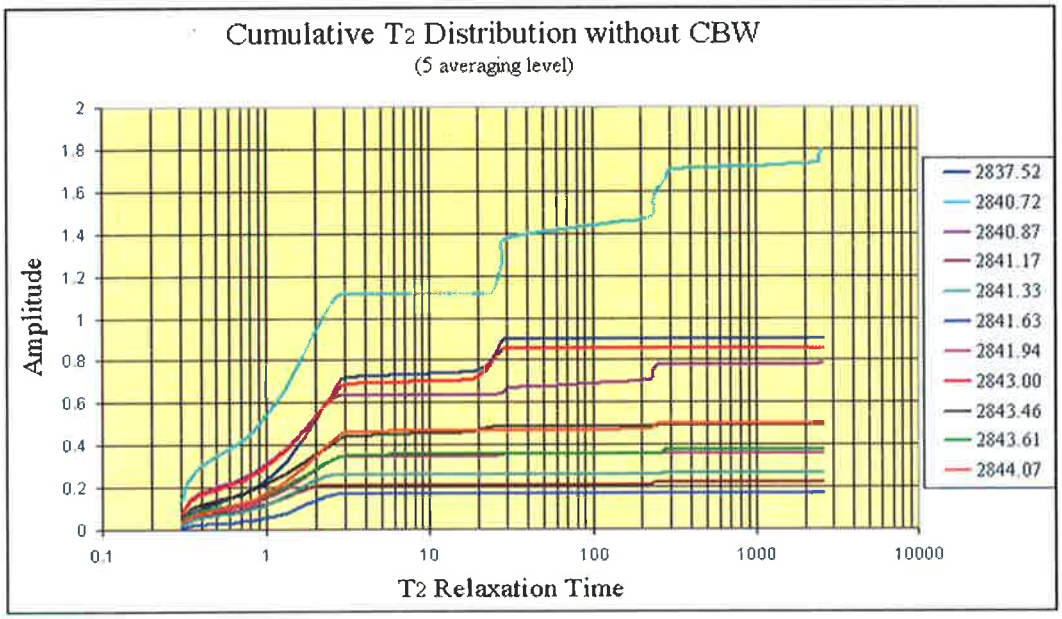

Figure 5.12 Cumulative T2 distribution after taking out the clay bound water (CBW) for every depth sample.

5.5.2 Creating Pseudo Capillary Pressure Curves

Converting the two axes of T2 distribution to their equivalent capillary pressure is essential to build pseudo capillary pressure curve. The two axes of T2 distribution were converted from relaxation time and amplitude to capillary pressure and water saturation respectively.

Water saturation was calculated by considering the maximum cumulative amplitude to be 100% for each curve. Then, the water saturation for every cumulative amplitude value can be calculated by the following relationship (Eq.5.2);

$$Water\ Saturation\ (100\%) = \frac{Amplitude\ Value * 100}{Maximum\ Amplitude\ Value} \qquad \text{(Eq.5.2)}$$

The relaxation time of T2 distribution extends logarithmically from 0.3ms to 3000ms. The short relaxation time represents small pores, thereby, high capillary pressure. In contrast, long relaxation time represents large pores and low capillary pressure. The relationship between relaxation time and capillary pressure is reversible (Eq.5.3). The effective surface relaxivity (ρ_e) is proportional to the product of intrinsic surface relaxivity (ρ) and the ratio of pore throat size to pore body size.

$$P_c = \frac{\rho_e}{T_{2s}} \qquad \text{(Eq.5.3)}$$

Where,

Pc = Capillary pressure (in psi)

T_{2s}= Surface grain relaxation time (in ms), which dominates the T_2 response in 100% water saturation

ρe = Effective surface relaxivity factor (combines surface relaxivity and pore/throat size ratio)

By knowing the relaxation time values for each curve, capillary pressure can be calculated when the appropriate effective surface relaxivity factor (ρ_e) is known. The Pretty Hill Sandstone effective surface relaxivity factor (ρ_e), is 1200 as the best fit (constant) for reservoir lithologies. However, this value does not work for flood plain samples. Therefore, the correct factor had to be estimated using trial and error technique. The best effective surface relaxivity factor (ρ_e) for all 11 flood plain facies samples was found to be 2300. A reliable factor is essential to build a valid calibration.

The water saturation axis was converted to a non-wetting phase saturation by subtracting from 100. This was done in order to calibrate to mercury injection capillary pressure (MICP) data. The 11 pseudo capillary pressure curves which were converted from T2 distribution are illustrated in Figure 5.13 (detailed results in Appendix-B). Note that the 2840.66m curve has a different trend than the other curves and it can be considered as an outlier. This is because it is a fine sandstone and also it was affected by the response from the coarse sand interval in between the flood plain section (due to 5 stacking level).

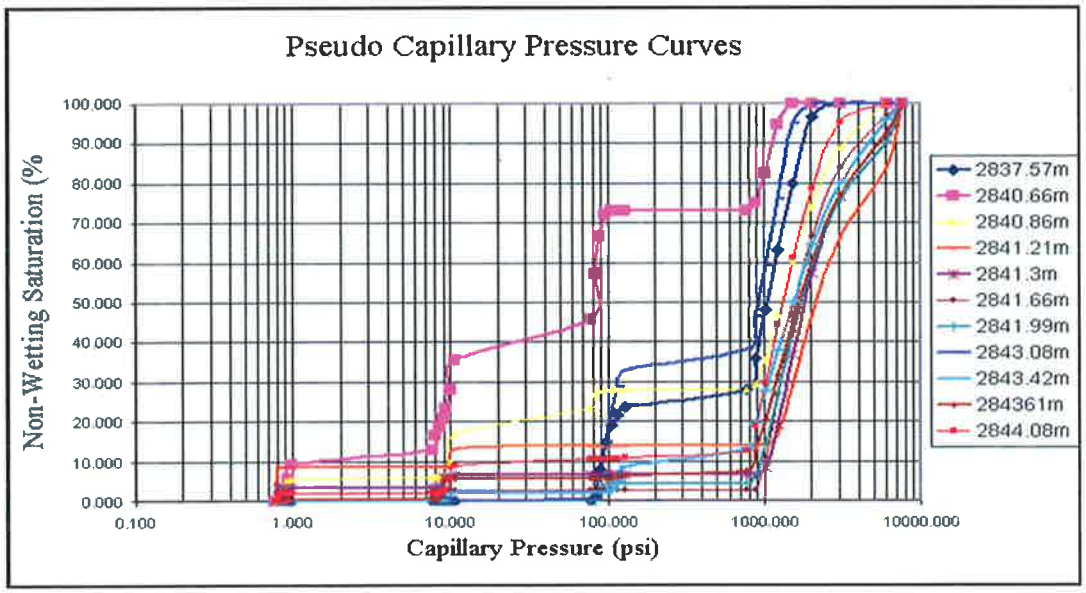

Figure 5.13 Pseudo Capillary pressure curves from T2 distribution. 11 curves are for flood plain facies samples in Redman-1. The high entry pressure is recognized for all samples except for 2840.66m which is affected by nearby coarser samples.

5.6 Pseudo Pc and MICP Curves Calibration

Full curve calibration of pseudo capillary pressure and mercury injection capillary pressure (MICP) curves was done for the 11 samples. The best effective surface relaxivity factor (ρ_e) used for pseudo capillary pressure was 2300 for all samples. Figures 5.14 to 5.24 shows the full curve calibration for every depth sample. An obvious mismatch between the two curves was recognized for most of the samples. Selecting a different effective surface relaxivity factor (ρ_e) for each sample was not practical to build a reliable relationship.

Some samples have consistent variation between the pseudo capillary pressure plots and the measured capillary pressure curves such as Sample 1 (Figure 5.14, 5.15, 5.17 and 5.21). Most of the samples exhibit deviation at the beginning of the curve with low pressure and non-wetting saturation (0-30% Snw) such as Sample 3 (Figure 5.16, 5.18, 5.19, 5.20, 5.22, 5.23 and 5.24). The disparity of the pseudo capillary pressure curve increases where NMR T2 distribution represents two lithologies, shale and sand. Consequently, the deviation of the pseudo capillary pressure curve is more dominant when the median pore size of the sample increases (Figures 5.14-24). Calibration is poor when median pore throat size is grater than 0.013microns. It gets better, at high pressure equivalent to extremely small pore sizes.

The most important part of the capillary pressure curve in conventional seal capacity determination is the displacement pressure. Pseudo capillary pressure curves have a mismatch from the actual MICP curve in the low pressure region (large pore throats). This means pseudo capillary pressure curves will not be reliable in estimating displacement pressure when using a simple effective surface relaxivity factor (ρ_e). Pseudo capillary pressure curves have good calibration to MICP above 30% non-wetting phase (NWP) saturation (small pores) in most of the samples except Sample 8 (2843.08m) which is influenced by micro fractures.

5.7 Estimation of NMR Displacement Pressure

Displacement pressure can be estimated from MICP curves by determining the capillary pressure at 10% non-wetting phase (NWP) saturation (Schowalter, 1979). The 20% and 35% NWP saturations were examined as well because displacement pressure in seal lithologies is higher than in the reservoir lithologies that Schowalter studied. Therefore, displacement pressures were selected at 10%, 20% and 35% NWP saturations from both pseudo capillary pressure and mercury injection capillary pressure (MICP) curves (Table 5.1). This technique assumes both curves are representing one lithology. Displacement pressures plotted against depth for the 11 samples are shown in Figures 5.25-27.

The best calibration between the three saturation percentages used is the 20% saturation. Agreement between the curves at 35% is the worst. While it improves at 10%, they are not close enough. Other saturation percentages were also examined but little improvement was seen. Statistically, correlation coefficient for the 10%, 20% and 35% saturations were analyzed (Figure 5.28-30). It is obvious from the correlation coefficients that the 20% saturation values give the best estimation of the displacement pressures. The correlation coefficient at the 20% saturation is 0.59 but it is not good enough to rely on to estimate displacement pressure. Moreover, the standard deviation distribution of the 20% saturation shows the difference between MICP and pseudo capillary pressure values around the mean (Figure 5.31). MICP values are distributed well around the mean which increase the statistical confidence of the measurements whereas pseudo capillary pressure values are skewed.

20% NWP saturation of T2 pseudo capillary pressure curve

Mean = 667.79

Standard Deviation = 478.38

20% NWP saturation of mercury injection capillary pressure curve

Mean = 627.93

Standard Deviation = 290

Pseudo capillary pressure deviation from the true displacement pressure increases when median pore size increases which indicates more sand contribution. Sample 1 (2837.57m), Sample 2 (2840.66m), Sample 3 (2840.86m) and Sample 4 (2841.21m) have large median pore sizes, representing two lithologies (shale and sand), and the greatest deviation occurs within those samples. Also, Sample 8 (2843.08m) has the higher median pore size but this is influenced by micro fractures which contribute to the mismatch. This deviation might be due to one reason or many factors may contribute to the poor match. Sample 2 (2840.66m) which can be considered an outlier was taken out to improve the calibration but the correlation was statistically worse. This decline may be due to the inadequate sample numbers. The different factors which may influence NMR response and subsequently T2 distribution are discussed in detail in the following chapter.

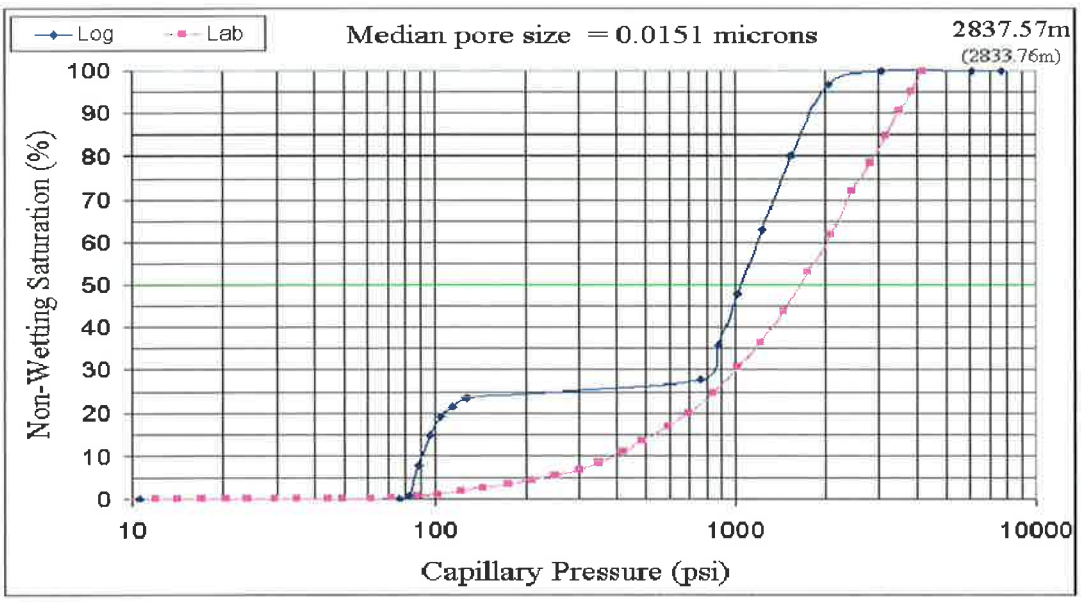

Figure 5.14 T2 pseudo capillary pressure and MICP calibration curves. The mismatch increases with an increase in pore size especially at large pore sizes (low non-wetting phase saturation). Redman-1, Sample 1.

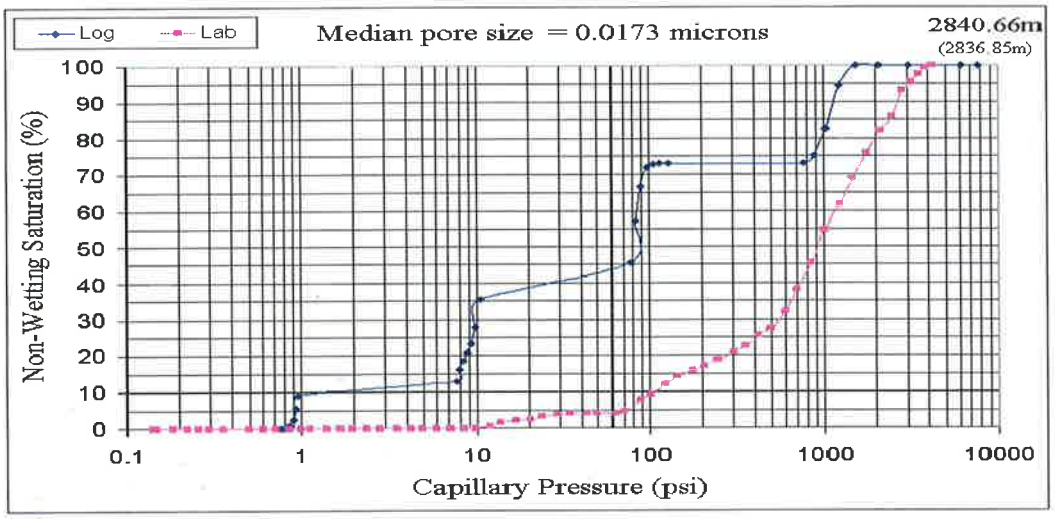

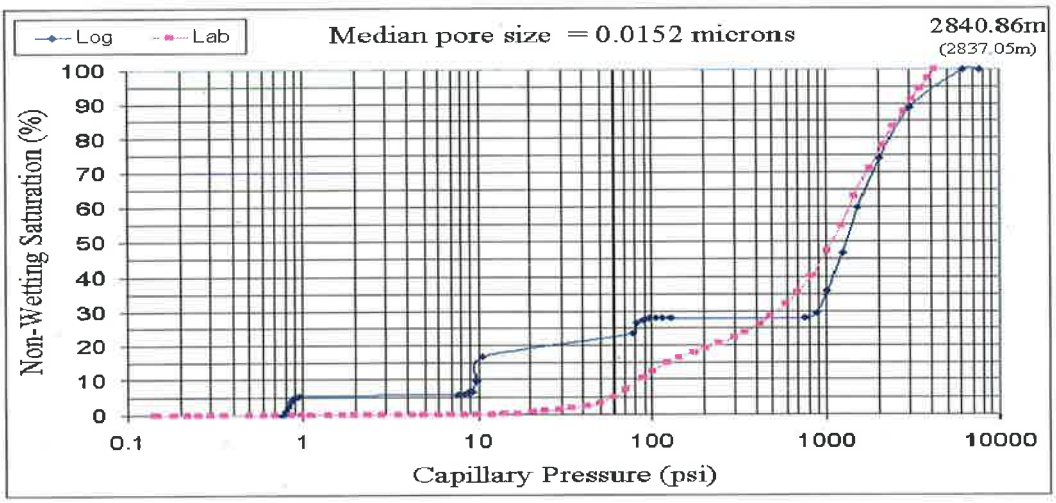

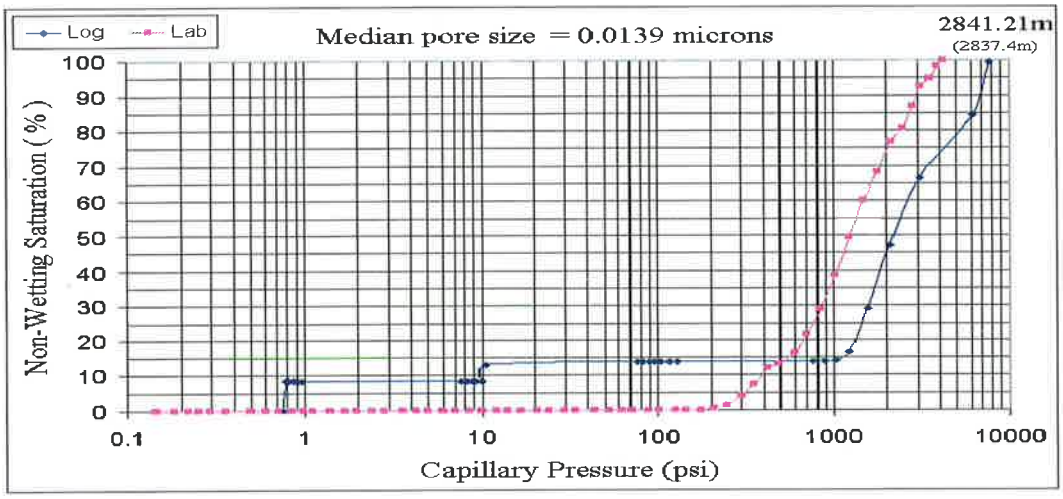

Figure 5.15-17 T2 pseudo capillary pressure and MICP calibration curves. The mismatch increases with an increase in pore size especially in large pore sizes (low non-wetting phase saturation). Redman-1, Sample 2-4.

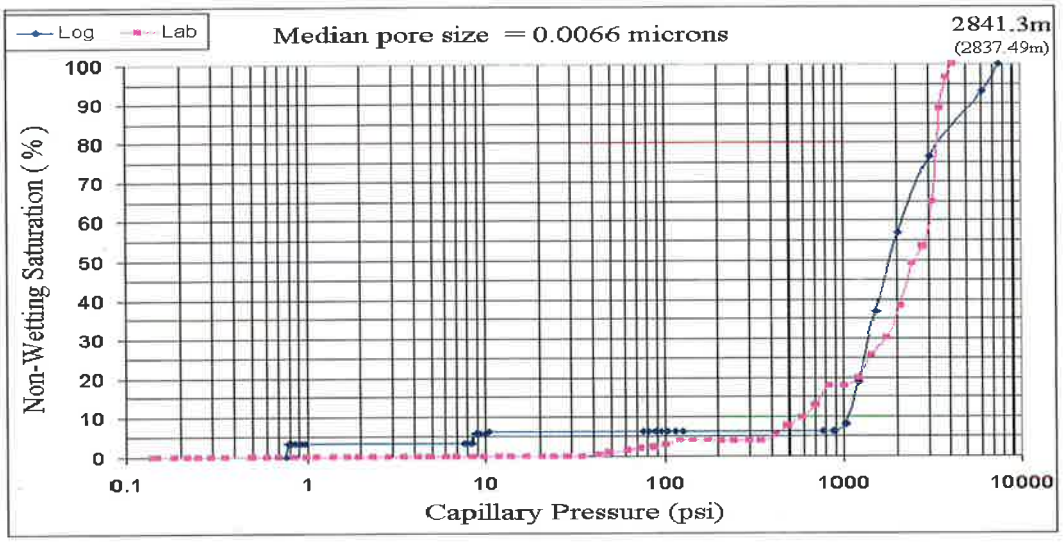

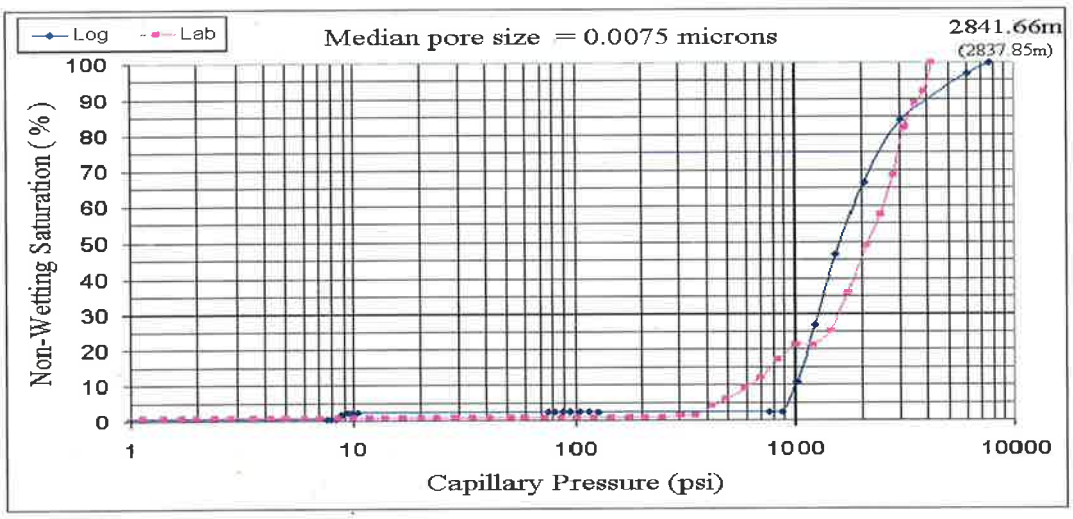

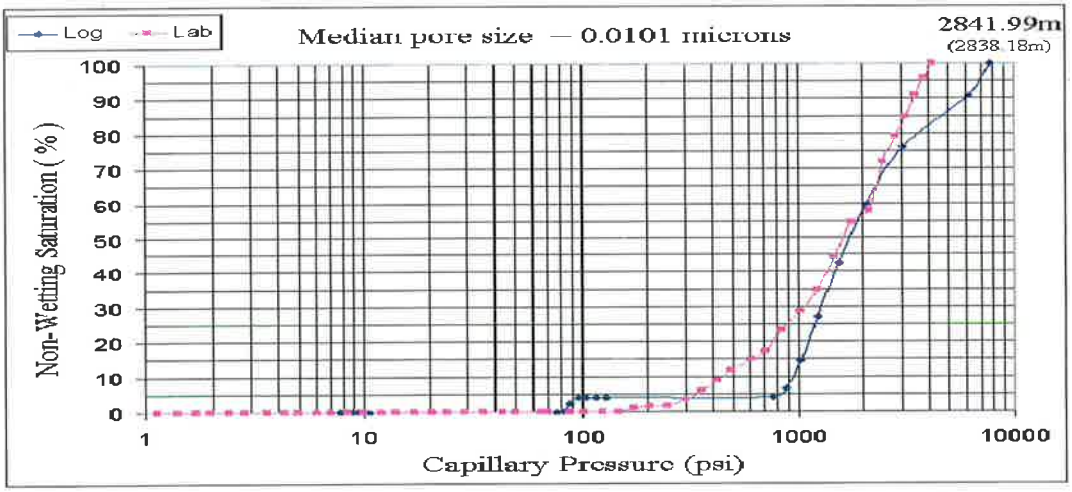

Figure 5.18-20 T2 pseudo capillary pressure and MICP calibration curves. The mismatch increases with an increase in pore size especially in large pore sizes (low non-wetting phase saturation). Redman-1, Sample 5-7.

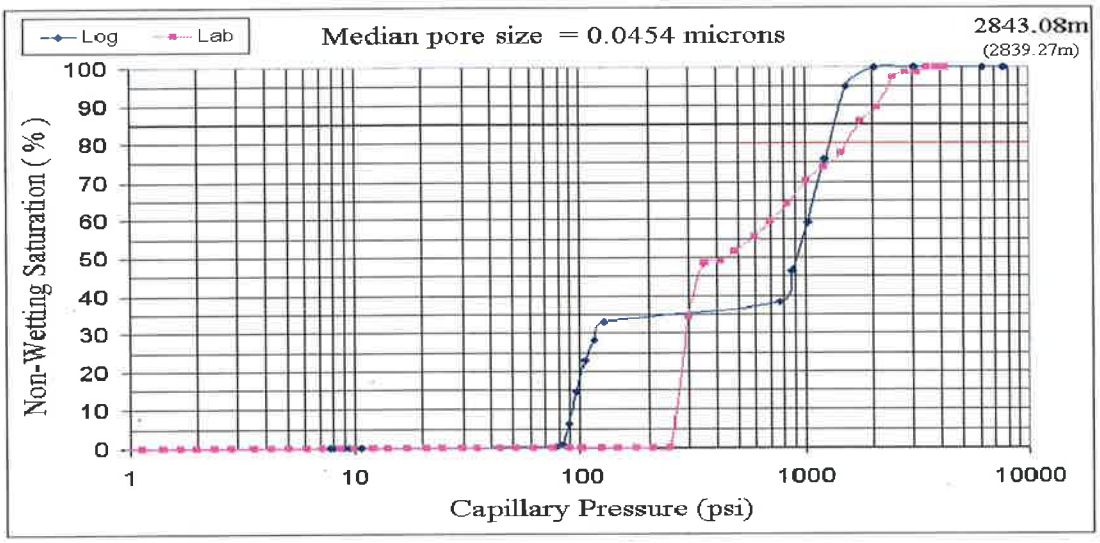

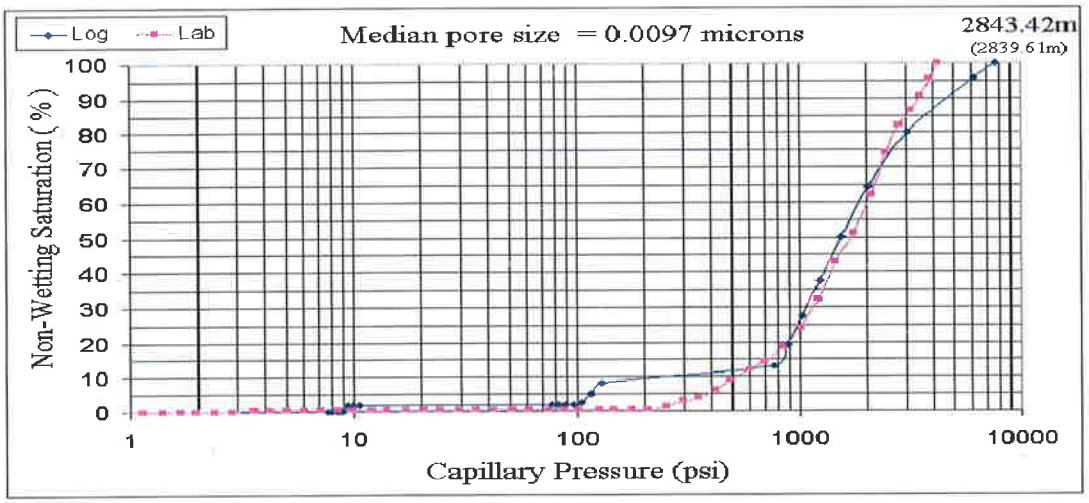

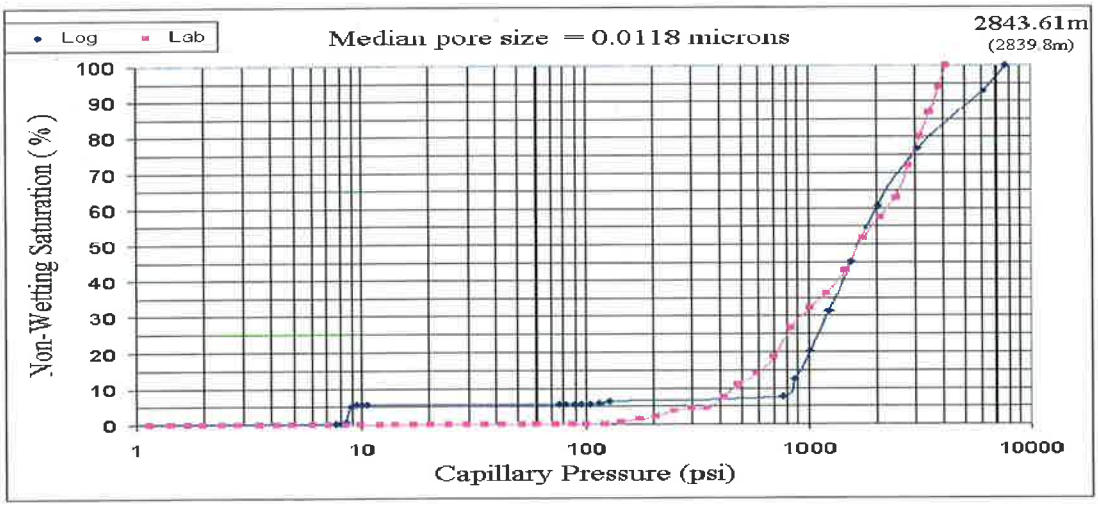

Figure 5.21-23 T2 pseudo capillary pressure and MICP calibration curves. The mismatch increases with an increase in pore size especially in large pore sizes (low non-wetting phase saturation). Redman-1, Sample 8-10.

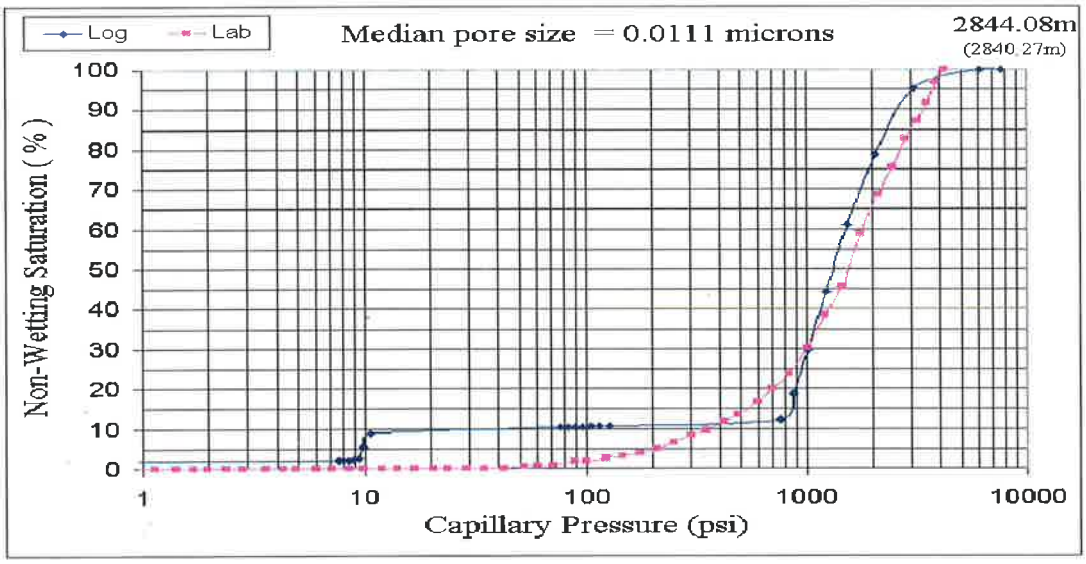

Figure 5.24 T2 pseudo capillary pressure and MICP calibration curves. The mismatch increases with an increase in pore size especially in large pore sizes (low non-wetting phase saturation). Redman-1, Sample 11.

		10th Percentile		20th Percentile		35th Percentile	
Sample No.	Log-depth	MICP Pd	Log Pd	MICP Pd	Log Pd	MICP Pd	Log Pd
1	2837.57	349.960316	88.46153846	699.4302603	104.5454545	1014.357099	766.6666667
2	2840.66	102.1413394	0.966666667	247.6180507	8.433333333	596.2020942	9.921568627
3	2840.86	70.93318349	9.921568627	207.7145783	10.54166667	595.7243681	876.1904762
4	2841.21	350.0713171	9.921568627	597.7202794	1226.666667	841.85093	1533.333333
5	2841.3	599.2173885	1022.222222	1219.991462	1226.666667	1748.029778	1226.666667
6	2841.66	597.7806977	876.1904762	840.2083955	1022.222222	1454.684213	1226.666667
7	2841.99	420.6700923	876.1904762	704.8974133	1022.222222	1216.840578	1226.666667
8	2843.08	247.4023714	88.46153846	247.4023714	95.83333333	302.1392372	127.7777778
9	2843.42	490.5684369	127.7777778	841.4947431	876.1904762	1219.982329	1022.222222
10	2843.61	419.9183764	766.6666667	701.0018384	876.1904762	1014.96901	1226.666667
11	2844.08	350.4921375	10.54166667	599.7716912	876.1904762	1013.880778	1022.222222

Table 5.1 Comparison table for displacement pressures (Pd) in every sample at different saturations (10%, 20% and 35%) for MICP curves and NMR T2 pseudo capillary pressure curves.

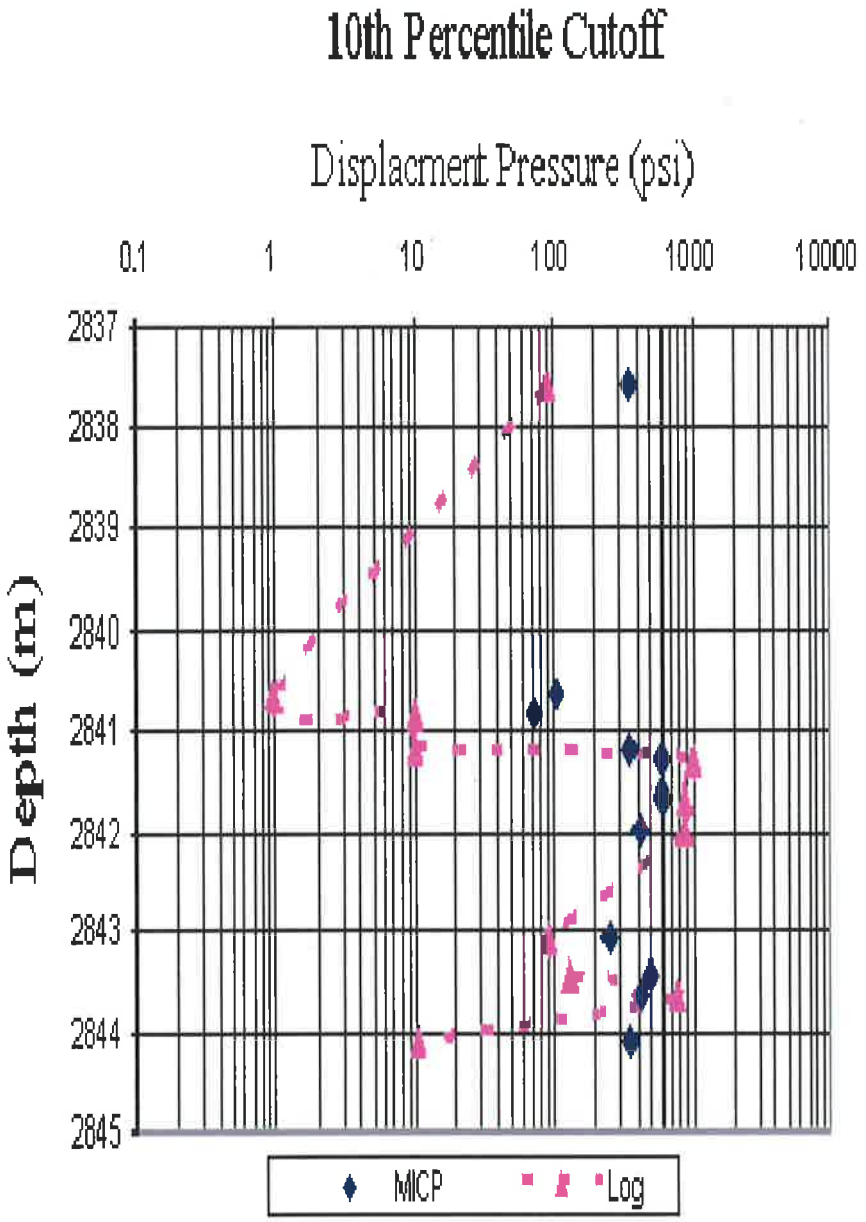

Figure 5.25 The displacement pressure at 10% non-wetting phase saturation for both T2 pseudo Pc and MICP curves. T2 pseudo Pc estimation gives poor agreement with the MICP values.

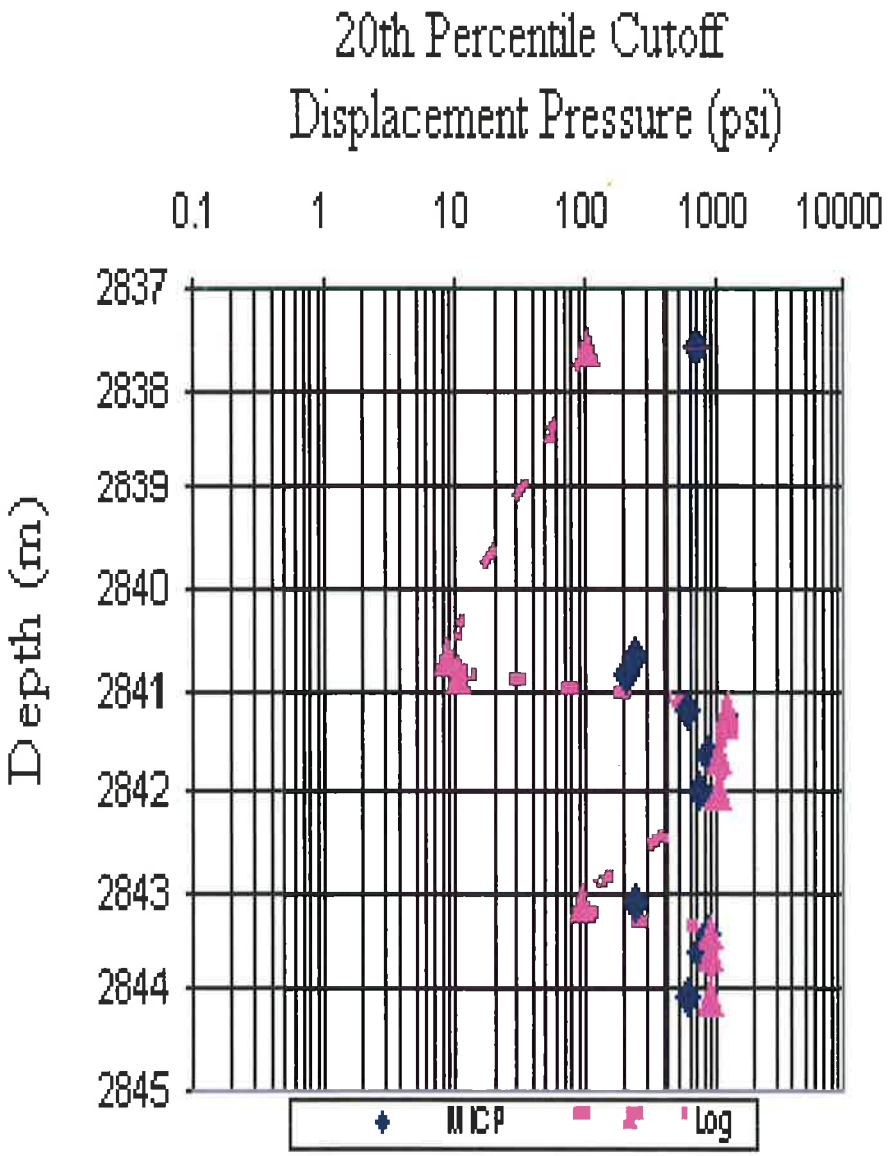

Figure 5.26 The displacement pressure at 20% non-wetting phase saturation for both T2 pseudo Pc and MICP curves. T2 pseudo Pc estimation at this saturation is the best to predict the MICP displacement pressures but it is not good enough to accurately predict MICP values.

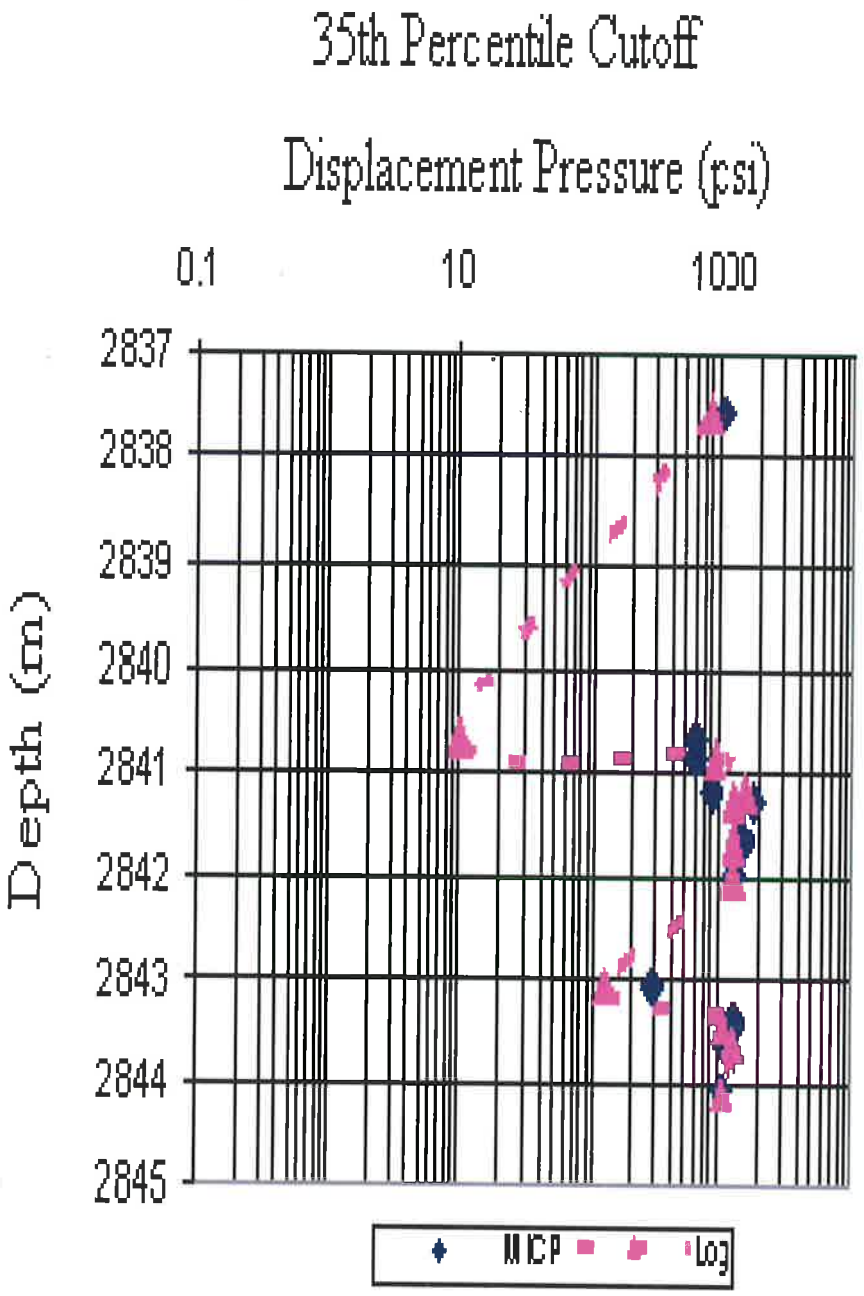

Figure 5.27 The displacement pressure at 35% non-wetting phase saturation for both T2 pseudo Pc and MICP curves. T2 pseudo Pc at this saturation is not accurate enough to predict displacement pressures.

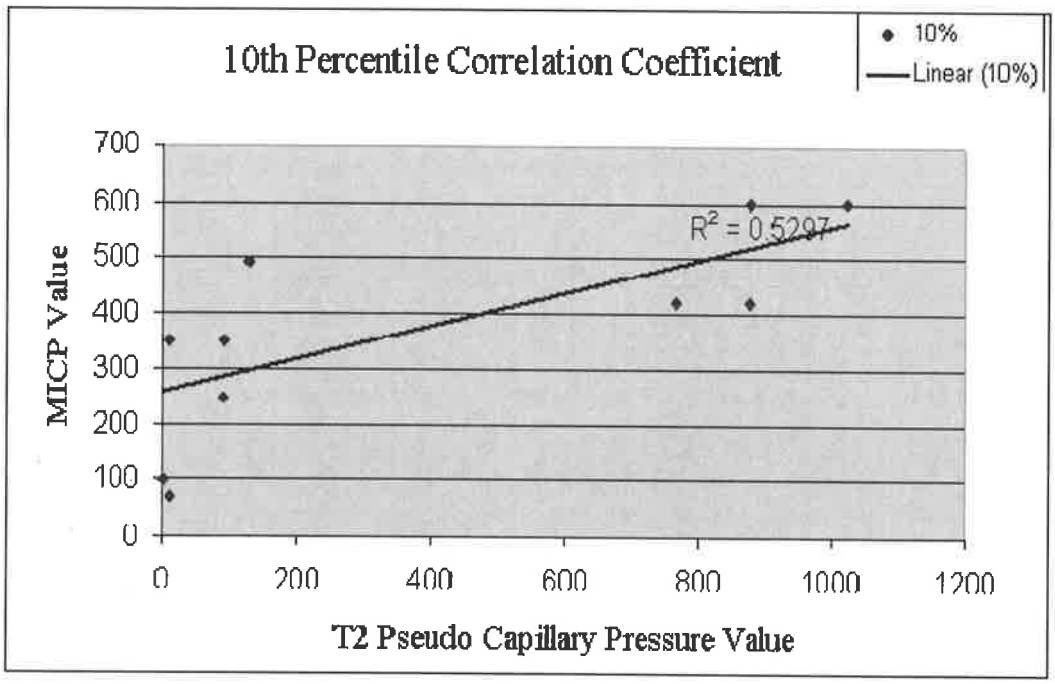

Figure 5.28 The correlation coefficient at 10% non-wetting phase saturation for the two data sets (MICP and Pseudo Pc) is low.

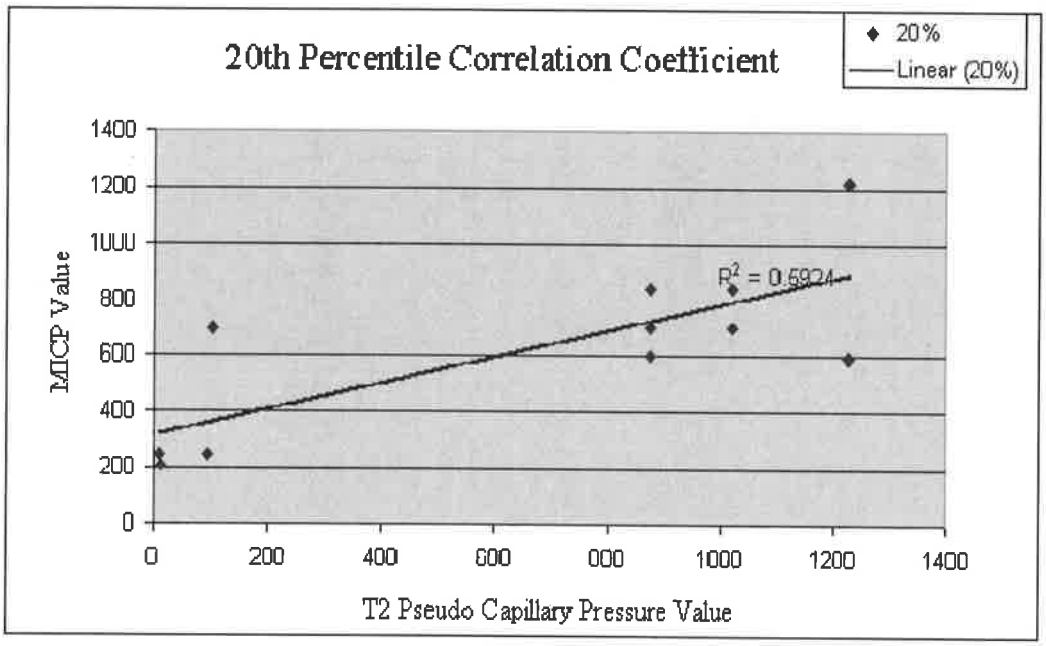

Figure 5.29 The correlation coefficient at 20% non-wetting phase saturation for the two data sets (MICP and Pseudo Pc) is considered the best in this study but it is not good enough to accurately predict MICP values.

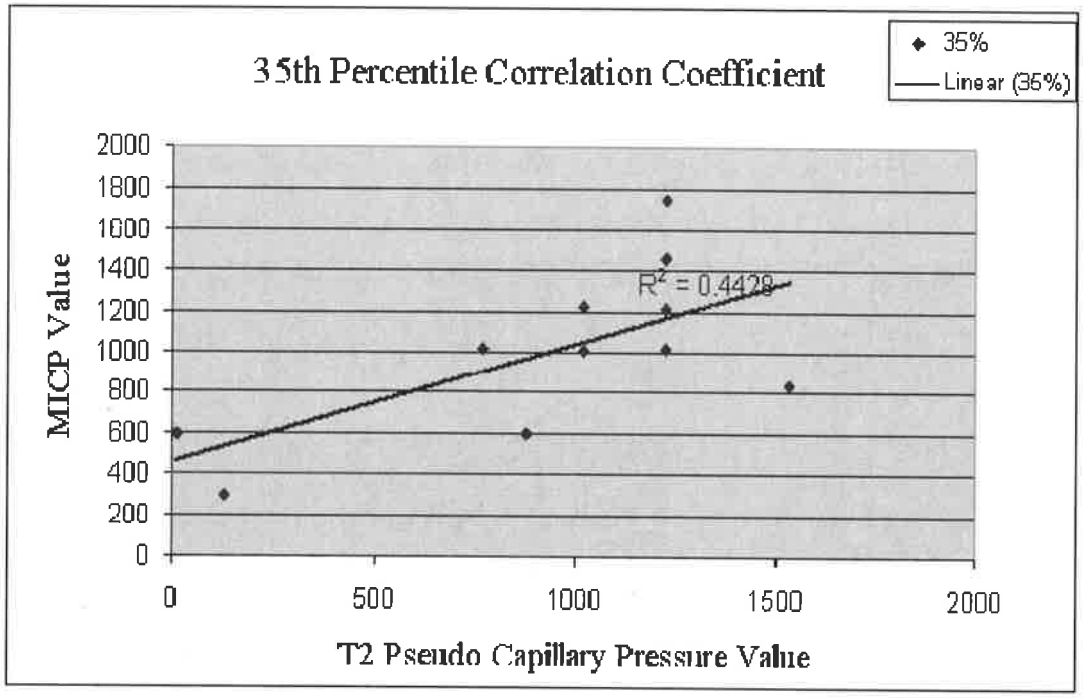

Figure 5.30 The correlation coefficient at 35% non-wetting phase saturation for the two data sets (MICP and Pseudo Pc) is too low and makes the worst correlation.

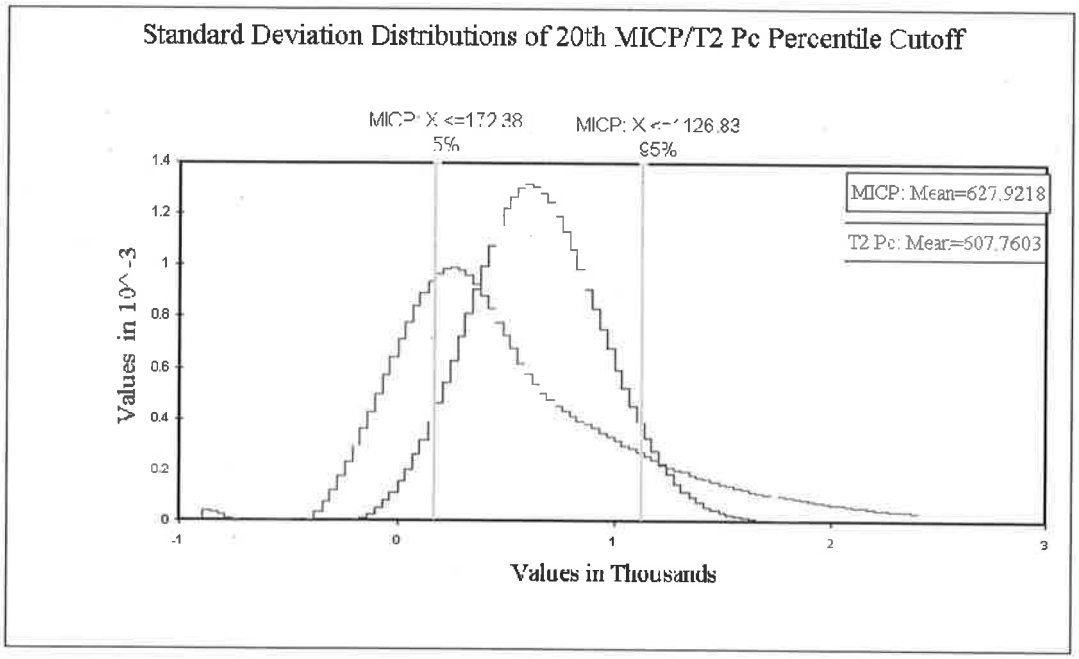

Figure 5.31 Standard deviation distributions of the 20% non-wetting phase saturation for MICP and pseudo capillary pressure curves. MICP values distribute very well around the mean unlike the pseudo capillary pressure values.

CHAPTER SIX
DISCUSSION

6.1 Introduction

Nuclear magnetic resonance (NMR) does not effectively estimate displacement pressure in fine grained lithologies in the Pretty Hill Formation. In addition, the high standard deviation value, 478.38, in the 2% NWP saturation of pseudo capillary pressure shows wide spread around the mean which indicates a high level of uncertainty.

This part of the study investigates and discusses the reason(s) that contribute to T2 distributions giving poor estimates of displacement pressures. These reason(s) might be mineralogical or petrophysical or both or due to sampling errors. The mineralogical reasons will be discussed first followed by the petrophysical and sampling ones.

6.2 Discussion

Nuclear Magnetic resonance (NMR) response is sensitive to the molecular diffusion of the pore fluid if the applied magnetic field is not homogeneous. The fluid possesses a gradient over a length scale that corresponds to the dephasing length of the spins. The NMR tool controls this gradient by applying pulse sequences known as the CPMG technique. However, the magnetic susceptibility between the solid phase and the fluid in the pore space can lead to significant magnetic field inhomogeneities which are called internal magnetic field gradients (Hurlimann, 1998).

This internal field gradient is caused mainly by the presence of paramagnetic ions such as iron, nickel and manganese which are frequently found in clays (Kleinberg et al, 1994). The effect of the internal field on

the NMR response depends on its magnitude and the applied magnetic field. If these gradients are equal to or larger than the applied tool gradient, interpretation of NMR data becomes more complicated. Moreover, the magnitude of internal field gradient increases in small pore sizes and high iron-rich clay content (Appel et al, 1999). The Redman-1 flood plain samples are characterized by small pore size system and high concentration of iron which suggests the existence of internal magnetic field gradients.

XRD analysis and thin sections show high content of chlorite and biotite minerals in the flood plain facies of Redman-1 core. XRD result shows that Chlorite, (Mg, Al, Fe)12 [(Si, Al)8O20] (OH)16, is between 7 and 9 percent of the total bulk sample in all 11 samples. Point counting indicates that Biotite, K2 (Mg, Fe+2)6-4 (Fe+3, Al, Ti)0-2 [Si6-5 Al2-3 O20] (OH, F)4, is between 7 and 12 percent. Approximately 12 to 20 percent of the bulk samples are composed of iron-rich minerals.

Iron oxide content expressed as Fe_2O_3 (Fe^{2+}/Fe^{3+} was not measured) was measured using XRF technique and varied between 5.2 and 7.16 percent (Table 6.2.1). Iron in the Pretty Hill Formation is characterized by its reduced status. The Fe^{2+}/Fe^{3+} ratio was found (previous studies) 0.7 in the Pretty Hill Sandstone and 0.9 in the Otway Group Sandstone (Tingate, personal communication). The high concentration of iron would raise its effect directly on NMR response and subsequently the conversion to pseudo capillary pressure.

Internal magnetic field gradients in iron-rich clays have been reported by many authors (Zhang et al, 1998; 2001; 2003; Appel et al, 1999 and Shafer et al, 1999). Researcher attention has focused mainly on chlorite since it is the most common iron-rich mineral found in sandstone reservoirs. Zhang et al (2001) examined the internal magnetic field gradient of both chlorite (iron-rich clay) and kaolinite (iron-free clay) fluid slurries to measure the magnetic field difference. Different chlorite fluid slurries were used and they produced maximum magnetic field gradient values that are

significantly higher than the kaolinite fluid slurries (Table 6.2.2). Also, the internal magnetic field gradient values for chlorite fluid slurries are much greater than the applied gradient of the logging tool. The internal magnetic field gradients are proportional to the volume of magnetic susceptibilities between grains and pore fluids (Kleinberg and Vinegar, 1996).

Depth	SiO2	Al2O3	MgO	Fe2O3	CaO	Na2O	K2O	TiO2	P2O5	MnO	SO3
	%	%	%	%	%	%	%	%	%	%	%
2837.57	53.27	22.75	2.38	6.60	0.76	2.00	4.93	1.40	0.17	0.07	0.04
2840.66	63.81	17.80	1.54	5.45	1.01	3.30	3.26	0.82	0.13	0.06	0.06
2840.86	61.62	19.05	1.77	5.65	0.86	2.97	3.77	0.89	0.13	0.06	0.07
2841.21	65.40	15.62	1.68	7.16	0.72	2.65	2.82	0.80	0.13	0.08	0.06
2841.30	62.24	17.70	1.92	6.09	0.92	2.07	3.84	0.93	0.12	0.06	0.06
2841.66	63.35	17.31	1.81	5.83	0.92	2.09	3.84	0.93	0.13	0.06	0.06
2841.99	62.21	17.88	1.79	5.67	1.06	2.02	4.06	0.97	0.14	0.06	0.10
2843.08	62.93	17.55	1.78	5.57	0.80	2.30	3.95	0.94	0.14	0.06	0.08
2843.42	62.85	17.79	1.84	5.94	0.86	2.28	3.96	0.91	0.14	0.07	0.08
2843.61	60.51	18.68	1.98	5.98	0.98	1.92	4.24	1.01	0.14	0.06	0.23
2844.08	62.54	17.98	1.73	5.21	0.69	2.67	3.85	1.02	0.13	0.06	0.07

Table 6.1 XRF analysis results with the paramagnetic cations highlighted. Fe_2O_3 (Fe^{2+}/Fe^{3+} ratio was not determined) has high concentration in flood plain Redman-1 samples and traces of the manganese.

A physical model was proposed for a chlorite-coated sandstone by Zhang et al (2001). Chlorite flakes can be viewed as forming microchannels perpendicular to the pore walls and therefore every mircopore opens to a macropore (Figure 6.1(a)). The magnetic fields in the macropores, micropores, and chlorite flakes were modeled between two planes which were parallel to the magnetic field lines. Field lines are concentrated inside the chlorite flake because of the paramagnetic characteristics of chlorite while the magnetic field strength is weakened in the micropore (Figure 6.1(b)). Also, the magnetic field difference increases between macropore and micropore when the size of the microchannel becomes small relative to

the size of the chlorite flake. This can occur in very restricted pore systems as in the Redman-1 flood plain samples.

The chlorite model can also be applied to biotite since it too, is an iron rich mineral with platey characteristics (Figure 6.2). Biotite is rich in iron which increases the magnetic susceptibilities between the solid phase and fluids.

Thus, the Redman-1 flood plain interval is expected to possess internal field gradients due to magnetic susceptibilities since it has high concentration of chlorite and biotite. Also, the very confined pore system of the rock interval suggests high internal magnetic field gradients. The magnitude of these gradients is not known in the flood plain interval of the Pretty Hill Formation at Redman-1, as measuring the magnitude of this internal field gradient is beyond the scope of this study. However, the internal field gradient is likely to affect the NMR response and thus increase the diffusion effect in the total T2 relaxation. Consequently, molecular diffusion relaxation rate dominates the total T2 relaxation in equation 2.1. If surface relaxation rate does not dominate T2 relaxation, the T2 time distribution does not represent pore size distribution.

$$\left(\frac{1}{T_2}\right)_{total} = \left(\frac{1}{T_2}\right)_S + \left(\frac{1}{T_2}\right)_B + \left(\frac{1}{T_2}\right)_D \qquad \text{(Eq.2.1)}$$

	Brine	Hexane	Soltrol
Chlorite	711	710	710
Kaolinite	1.8	4.0	3.7

Table 6.2 Maximum Internal field gradients (Gauss/cm) for different chlorite and kaolinite slurries. Chlorite has a much higher internal field gradient than kaolinite (Zhang et al, 2001).

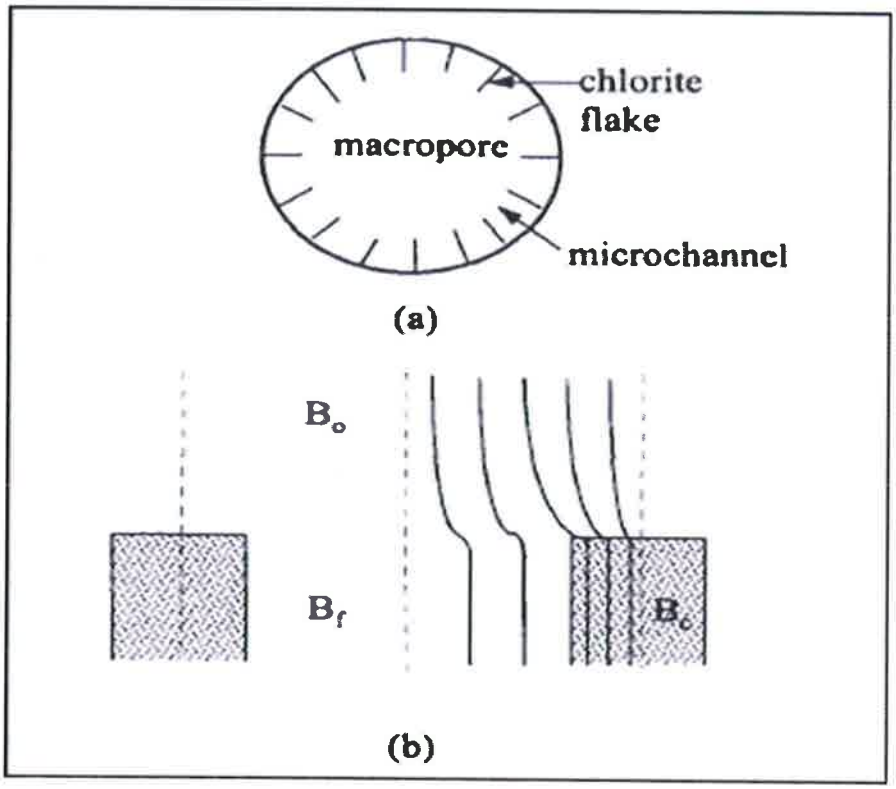

Figure 6.1 Model of magnetic field for chlorite coated sandstone. (a) chlorite flakes forming microchannels open to macro pore. (b) magnetic fields of macropore, B_o, micropore, B_f, and inside chlorite flake, B_c (Zhang et al, 2001).

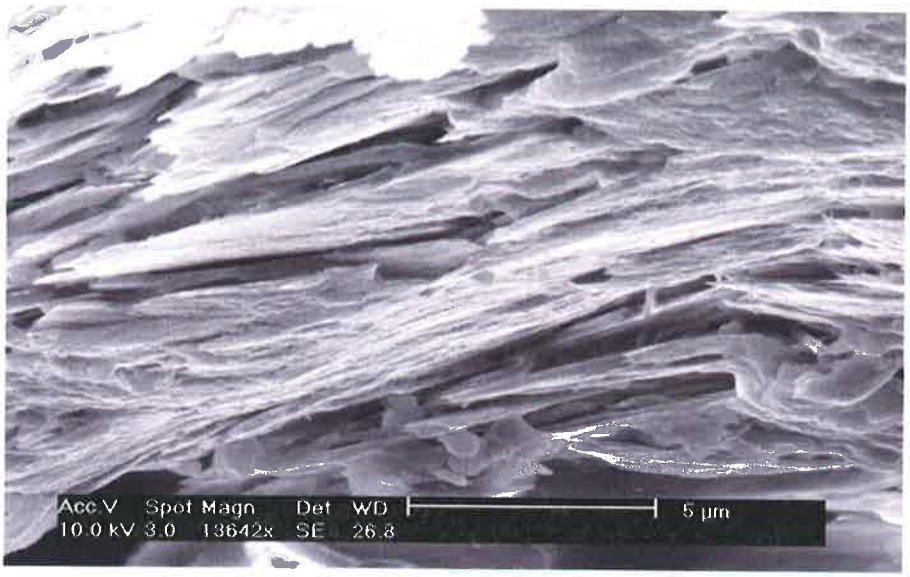

Figure 6.2 SEM photo shows biotite has platey structure which increases the internal magnetic field gradients.

Relaxivity, which is the ability of the surface to relax hydrogen nuclei, is also affected by the presence of magnetic minerals. Iron and manganese, which are the paramagnetic ions in the samples, increase NMR surface relaxivity parameter ρ by an order of magnitude or more. This variation is as great as the variation observed for pore size distribution in natural geological material (Roberts, et al 1995).

All Redman-1 flood plain samples have high iron concentration which can be considered as constant. If the iron content varies between samples, then the effective surface relaxivity factor (ρ_e) should also be changed to account for the variability (Figure 6.3). Given the consistency of the iron content, it may be possible to use the same effective surface relaxivity factor (ρ_e) for the whole interval. However, the increase in the effective surface relaxivity factor (ρ_e) shortens T2 distribution and pore size. Therefore, this adjustment leads to underestimation of the actual pore size of the sample and also the converted capillary pressure. The underestimation level is proportional to the concentration of the iron in the samples. Redman-1 samples have high iron concentrations and therefore unrealistic reduction of pore size and capillary pressure is likely to occur (Figure 6.4).

The nuclear magnetic resonance (NMR) response represents the hydrogen content in the pore space. The hydrogen exists mainly between grains or inside any kind of voids in the clastic or carbonate sediments. In clays, there is potentially hydrogen in bound water on the clay surface itself. The amount of surface space depends on the clay type. The smectite group or swelling clay has high surface area to volume ratio while kaolin has low surface area to volume. Changing clay type concentration will change surface area to volume ratio which is the base of NMR pore size quantification. Therefore, NMR response will vary based on the clay type present and not because of the variations in pore size distribution.

Redman-1 samples are rich in smectite (swelling) clay, between 8-32 % of the total volume. This high concentration of swelling clay might be responsible of significant amount of hydrogen on its surface that does not represent pore space between clay aggregates. Also, swelling clays can store hydrogen inside the smectite structure when it has high enough water saturation. In this study, this amount was estimated to be the difference between total and effective porosity and subtracted from T2 response. Because of the large amount of hydrogen which can be stored in such rock, the clay bound water cutoff (less than 1ms) might not be the solution to such problem. Therefore, it is believed that the pore geometry in such swelling-clay rocks is not well represented by NMR response.

Hence, T2 distribution position in clay-rich rocks such as the Redman-1 samples is affected by the difference and concentration of clay types. Consequently, changing T2 distribution position is not a function of inter aggregate pore size changes only but also of the large surface area of clays. Swelling clay (largest surface area) in particular can increase the deviation of T2 response which can not be able to represent the effective pore geometry of the sample (comparing to MICP measurements). Redman-1 samples have significant amount of smectite which contribute to the skewness of T2 distribution.

The NMR response is basically porosity or pore body size measurement while mercury capillary pressure is pore throat size measurement. From a petrophysical point of view, the T2 distribution is calibrated to capillary pressure curves based on the hypothesis that there is relationship between pore throat size and pore body size especially in clastic rocks. The sandstone pore system has low pore to throat size ratio and pore throat size can be estimated by knowing pore body size. Therefore, the effective surface relaxivity factor (ρ_e) was introduced to T2 distribution to take into account for pore to throat size ratio as well as relaxivity.

The difference between MICP drainage and imbibition curves is an indication of the pore to throat size ratio. The pore to throat size ratio increases in very fine grained rocks such as Redman-1 samples (appendix A). The Redman-1 flood plain samples have very confined pore system and pore throat sizes are very small, between 0.1 to 0.004microns (appendix A). Blue epoxy resin, which was used to prepare thin sections, was not able to enter the pore system of the rock even after etching, confirming the small size of the pore throats in there samples (Figure 6.5). Therefore, the large difference between pore and throat size measurements might be too high to be adjusted by the effective surface relaxivity factor (ρ_e).

The Redman-1 flood plain samples are clay rich samples which are characterized by isolated pores with very small patchy connected throats (Figure 6.6). Thus, the difference between pore body and pore throat size is too high and variable which means they can not be estimated from each other. Therefore, the two measurements, T2 distribution and MICP distribution, are difficult to compare in very fine sediments (clay rich rocks).

A question raised here is why does the deviation in capillary pressure estimation increase with median pore size. An answer may be that internal magnetic field gradients occur more readily in the bigger pore sizes. Brine, associated with internal gradients, in very small pores relaxes at a very early stage which does not give much time for protons to be affected by the internal magnetic field.

Finally, a better sampling selection of one lithology would help the study a lot in representing shale lithology effectively. More samples of only shale lithology will give a robust statistical correlation.

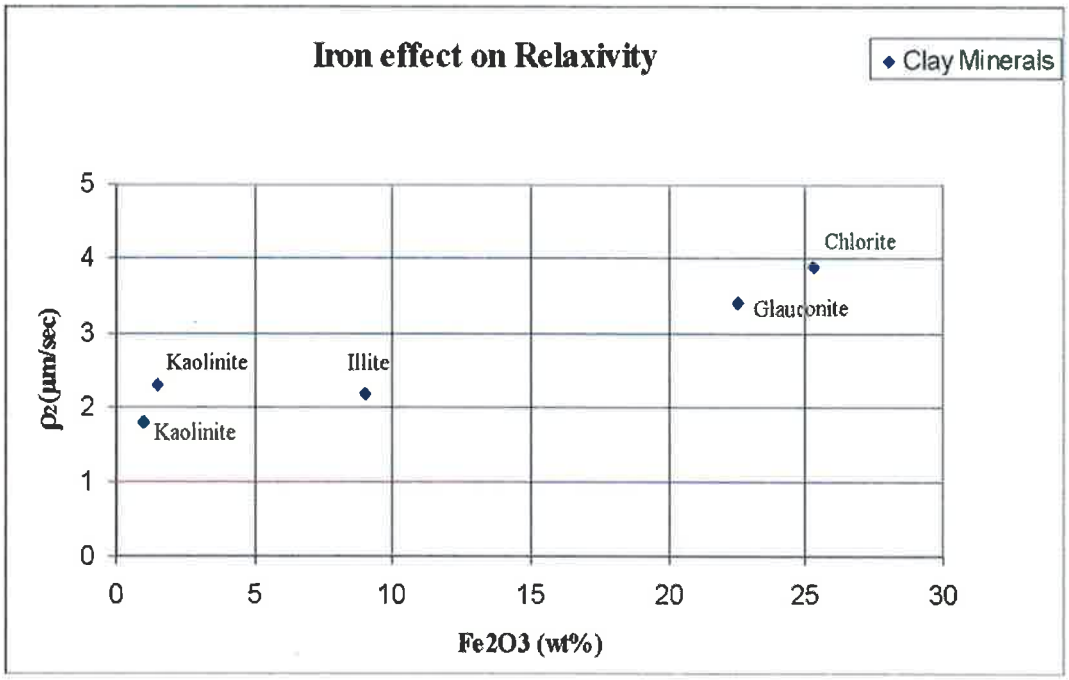

Figure 6.3 Iron oxides of different clay types and their effect on NMR surface relaxivity (modified after Matteson, et al 1998).

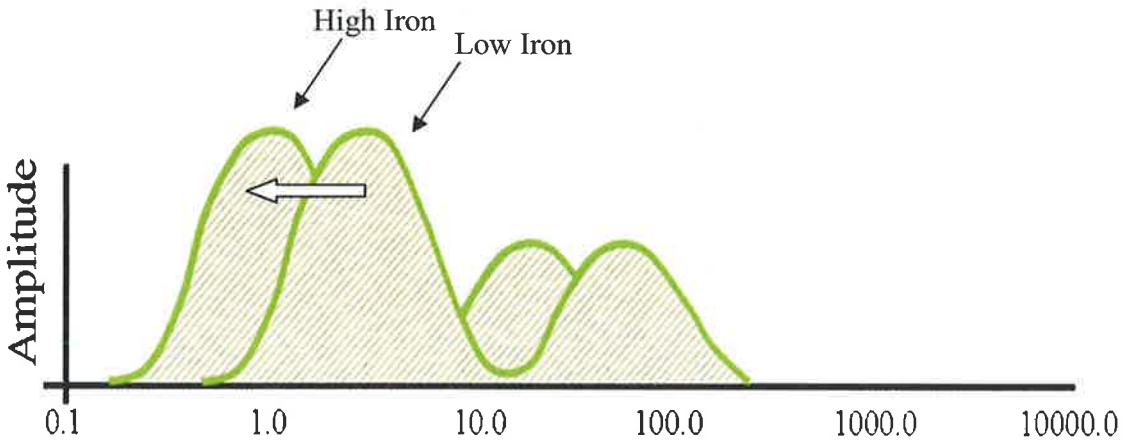

Figure 6.4 High iron concentration and clay type changes can affect T2 distribution position. T2 distribution is shortened by the increase in iron concentration.

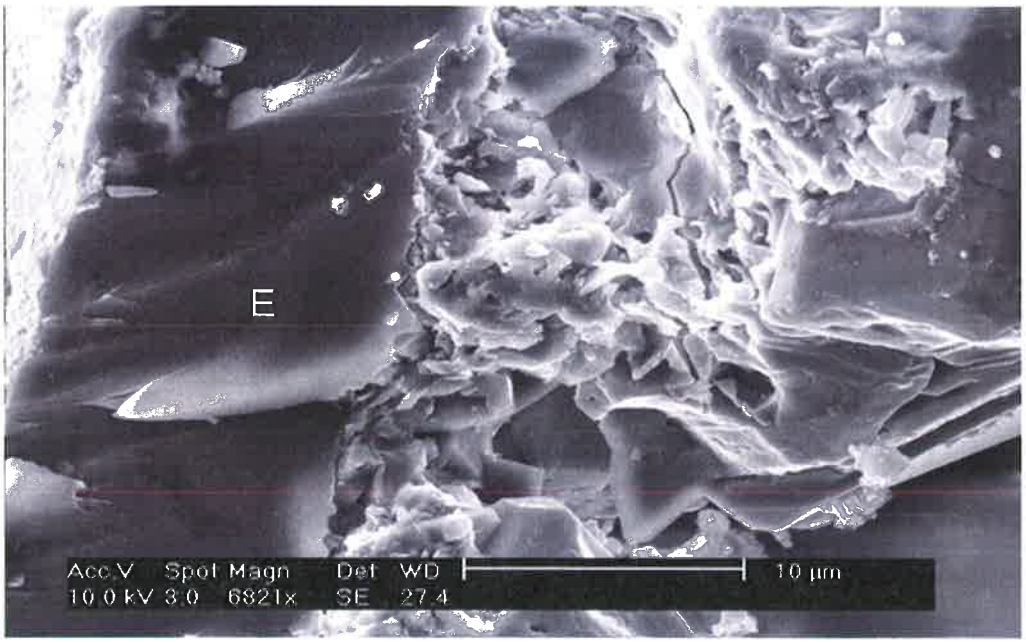

Figure 6.5 SEM photo of epoxy resin (E), on the left side, which could not enter pore space of very fine sandstone sample

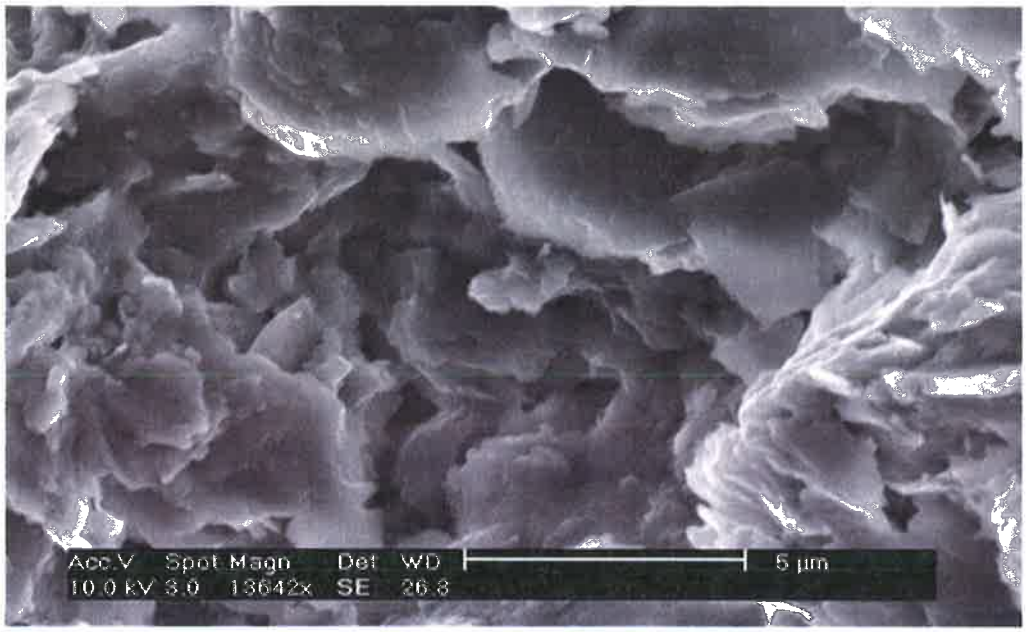

Figure 6.6 SEM photo of clayey siltstone with high pore to throat size ratio. Note isolated pores with poor connected throats.

CHAPTER SEVEN
CONCLUSIONS AND RECOMMENDATIONS

7.1 Conclusions

- The best estimated displacement pressures from the down-hole T2 pseudo capillary pressure curve is the 20% non-wetting phase saturation which has a correlation coefficient of 0.59 in flood plain samples. However, this correlation is not high enough to reliably determine seal capacity from CMR 200 data in low porosity formations.

- Down-hole T2 pseudo capillary pressure differs more from laboratory mercury injection capillary pressure (MICP) curve in large pores (low pressure). The difference increases with increasing pore size and calibration improves in smaller pores. The standard deviation of the 20% NWP saturation in T2 pseudo capillary pressure curve is much higher than MICP curve.

  20% NWP saturation of T2 pseudo capillary pressure curve

  Mean = 667.79 psi

  Standard Deviation = 478.38 psi

  20% NWP saturation of mercury injection capillary pressure curve

  Mean = 627.93 psi

  Standard Deviation = 290 psi

- The Redman-1 flood plain samples are iron-rich rocks, as XRD and XRF analyses show, due to the presence of minerals such as chlorite and biotite. Thus, increased magnetic susceptibility characterizes

Redman-1 flood plain samples because of the difference in paramagnetic ions between the solid phase and fluids.

- Internal magnetic field gradients are generated due to the magnetic susceptibility. NMR relaxation is affected by the internal field gradient and the effect is proportional to the internal field magnitude. The magnitude of the internal field gradient depends on the paramagnetic ions concentration which is high in Redman-1 flood plain samples.

- NMR response was dominated by the diffusion relaxation mechanism of the measurements in the large pores. As a result, the NMR response assumption of a pore size distribution in not valid in iron-rich rocks with small pores.

- The calibration improves in fine pores because hydrogen nuclei relax quickly by surface relaxation mechanism. Therefore, the internal magnetic field gradients do not influence the NMR response in extremely small pore sizes.

- Surface relaxivity varies as a function of heavy mineral concentration (such as iron content of samples). Therefore, the effective surface relaxivity factor (ρ_e) should be calibrated to the heavy mineral concentrations.

- Clay type and concentration can affect NMR T2 distribution position because every clay type has different surface area. Swelling clays have large surface areas which can affect surface to volume ratio and thereby, change NMR response.

- Pore to throat size ratio can be included in the effective surface relaxivity factor (ρ_e) in sandstone lithology. Pore to throat size ratio

could be more difficult to estimate in very fine pores because the ratio increases as pore size decreases.

7.2 Recommendations

- Calibrating NMR T2 distribution to mercury injection capillary pressure curve should be re-examined in fine grained lithologies with low paramagnetic ion content. Understanding clay type concentration and pore to throat size ratio can be useful when magnetic susceptibility and the high relaxivity effect are eliminated.

- The magnitude of the internal magnetic field gradients should be measured using magnetic susceptibility logging tool or NMR laboratory technique on Redman-1. The effect on NMR response may be predicted in the seal and reservoir intervals by recognizing the magnitude of the internal field gradients for the whole core.

- NMR measurements should be acquired down-hole over the Pretty Hill Formation with echo spacing as small as possible to minimize the diffusion effect. Also, the static field gradient of NMR tool should be as high as possible to control the internal magnetic field gradients.

- Investigation of pore to pore throat size ratio by using MICP drainage and imbibition curves in iron-free seal lithology should be carried out as they might help to constrain the relationship between the T2 and MICP displacement pressures.

- Hg samples should always be taken at least ½ the stacking interval resolution distance away from the edge of the lithology to be compared with the NMR response.

- Finally, CMR 200 tool might not be adequate to sample micro facies individually because of its poor resolution and acquisition. Higher signal to noise ratio data needs to be used in such study to provide more reliable T2 distribution without distortion.

References

Allen, D., Flaum, C., Ramakrishnan, T.S., Bedford, J., Castelijns, K., Fairhurst, D., Gubelin, G., Heaton, N., Minh, C.C., Norville, M.A., Seim, M.R., Prtichard, T., and Ramamoorthy, R., 2000, Trends in NMR logging: Schlumberger Oilfield Review, v. 12, no. 3, p. 2-19.

Appel, M., Freeman, J., Perkins, R. B., Hofman, J. P., Looyestijn, W. J., Slijkerman, W. F. J. and Volokitin, Y., 1999, Restricted diffusion and Internal Magnetic Field Gradients: Paper FF, in 40th Annual Symposium of SPWLA, May30-June3, Oslo, Norway, 13p.

Augsburg, A., Grundke, K., Pöschel, K., Jacobasch, H.J. and Neumann, A.W., 1998, Determination of contact angles and solid surface tensions of poly (4-X-styrene) films: Acta Polymerica v.49, no.8, p.417-426.

Bendel, P., 1990, Spin-echo attenuation by diffusion in non-uniform field gradients: Journal of Magnetic Resonance v.86, no.3, p.509-515.

Bentley, C., 2000, Operating Instructions for the Micromeritics Autopore 9410 Mercury Injection Porosimeter: unpublished report, University of South Australia.

Boult, P.J., Ramamoorthy, R., Theologou, East, R.D., Drake, A.M. and Neville, T., 1999, Use of Nuclear Magnetic Resonance and New Core Analysis Technology for Determination of Gas Saturation in Pretty Hill Sandstone Reservoirs, Onshore Otway Basin: APPEA Journal v.39, p.437-450.

Brown, R.J.S., and Gamson, B.W., 1960, Nuclear magnetism logging, SPE paper-1305: Journal of Petroleum Technology, v. 12, no. 8, p. 199-207.

Brownstein, K.R. and Tarr, C.E., 1979, Importance of classical diffusion in NMR studies of water in biological cells: Physical Review, v.19 (Series A), p.2446-2453.

Coates, G.R., Xiao, L. and Prammer, M.G., 1999, NMR Logging Principles and Applications: Houston, Halliburton Energy Services.

Cockshell, C.D., O'Brien, G.W., McGee, A., Lovibond, R., Perincek, D. and Higgins, R., 1995, Western Otway Crayfish Group Troughs: APEA Journal, v.35, p.385-404

Glorioso, J.C., Piotti, G. and Mengual, J., 2003, Deriving capillary pressure and water saturation from NMR transversal relaxation times, SPE paper- 81057: Journal of Petroleum Technology, 13p.

Hardy, R. and Tucker, M., 1988, X-ray Powder diffraction of Sediments, *in* M. Tucker, ed., Techniques in Sedimentology: Blackwell Scientific Publication, 7, p.191-228.

Hurlimann, M.D., 1998, Effective gradients In porous media due to susceptibility differences: Journal of Magnetic Resonance, v.131: p.232-240.

Jones, R.M., Boult, P., Hillis, R.R., Mildren, S.D. and Kaldi, J., 2000, Integrated hydrocarbon seal evaluation in the Penola Trough, Otway Basin: APPEA Journal, v.40, p.194-211.

Jorden, J.R. and Campbell, F.L., 1984, Well logging I - rock properties, borehole environment, mud and temperature logging: Society of Petroleum Engineers, v.9.

Kaldi, J.G., and Atkinson C.D., 1997, Evaluating seal potential, *in* R. Surdam, (ed.), Seals, traps and the petroleum system: AAPG memoir 67, p.85-101.

Kenyon, W., Kleinberg, R., Straley, C., Gubelin, G., and Morriss, C., 1995, Nuclear magnetic resonance imaging--technology for the 21st century: Schlumberger Oilfield Review, v. 7, no. 3, p. 19-33.

Kenyon, W.E., 1992, Nuclear magnetic resonance as a petrophysical measurement: Nuclear Geophysics, v. 6, no. 2, p. 153-171. Later revised and published in 1997 as Petrophysical principles of applications of NMR logging: The Log Analyst, v. 38, no. 2, p. 21-43.

Kenyon, W.E., Howard, J.J., Sezginer, A., Straley, C., Matteson, A., Horkowitz, K., and Ehrlich, R., 1989, Pore-size distribution and NMR in microporous cherty sandstones, paper LL, in 30th annual logging symposium transactions: Society of Professional Well Log Analysts, 24 p.

Kleinberg, R.L., Kenyon, W.E., and Mitra, P.P., 1994, Mechanism of NMR relaxation of fluids in rock: Journal of Magnetic Resonance, Series A, v. 108, no. 2, p. 206-214.

Kleinberg, R.L., and Horsfield, M.A., 1990, Transverse relaxation processes in porous sedimentary rock: Journal of Magnetic Resonance, v. 88, no. 1, p. 9-19.

Kleinberg, R.L., and Vinegar, H.J., 1996, NMR properties of reservoir fluids: The Log Analyst, v. 37, no. 6, p. 20-32.

Kopsen, E. and Scholefield, T., 1990, Prospectivity of the Otway supergroup in the central and western Otway Basin: APEA Journal, v.30, p.263-278.

Little, B.M., 1996, The petrology and petrophysics of the Pretty Hill Formation in the Penola Trough, Otway Basin: M.Sc. thesis (unpublished), University of South Australia.

Little, B.M. and Phillips, S.E., 1995, Detrital and authigenic mineralogy of the Pretty Hill Formation in the Penola Trough, Otway Basin: implications for future exploration and production: APEA Journal, v.35, p.538-557.

Lovibond, R., Suttill, R. J., Skinner, J.E., and Aburas, A.N., 1995, The hydrocarbon potential of the Penola Trough, Otway Basin: APEA Journal, v.35, p.358-371.

Lowden, B.D., Porter, M.J., Powrie, L.S., 1998, T2 relaxation time versus mercury injection capillary pressure: implications for NMR logging and reservoir characterization, SPE paper-50607: Society of Petroleum Engineers.

Marschall, D., Gardner, J.S., Mardon, D., and Coates, G.R., 1995, Method for correlating NMR relaxometry and mercury injection data: paper SCA-9511, in International SCA symposium proceedings, Society of Professional Well Log Analysts, Society of Core Analysts Chapter-at-Large, 12 p.

Matteson, A., Tomanic, J.P., Herron, M.M., Allen, D.F. and Kenyon, W.E., 1998, NMR relaxation of clay-brine mixtures, SPE Paper-49008: Transactions of the SPE Annual Technical Conference, 27-30 September, New Orleans, Louisiana, 7p.

Miller, J., 1988, Cathodoluminescence microscopy, *in* M. Tucker, ed., Techniques in Sedimentology: Blackwell Scientific Publications, 6, p.174-190.

Morris, C.E., Freedman, R., Straley, C., Johnstone, M., Vinegar, H.J. and Tutunjian, P.N., 1994, Hydrocarbon saturation and viscosity estimation from NMR logging in the Belridge Diatomite: Transactions of the SPWLA, 35th annual Logging Symposium, Tulsa, Oklahoma, June 19-20, paper C.

Morton, J.G.G., 1990, Revisions to stratigraphic nomenclature of the Otway Basin, South Australia: The Geological Survey of South Australia, Quarterly Geological Notes, No.116, p.1-19.

Morton, J.G.G., Hill, A.J., Alexander, E.M. and White, M.R., 1995, Lithostratigraphy and environments of deposition, *In* J.G.G. Morton, ed., The petroleum geology of South Australia series, Volume 1: The Otway Basin, South Australia, Department of Mines and Energy.

Miller, J., 1988, Cathodoluminescence microscopy. *In* M. Tucker, ed., Techniques in Sedimentology: Blackwell Scientific Publications, 6, p.174-190.

Purcell, W.R., 1949, Capillary pressures – Their measurements using mercury and calculation of permeability therefrom: AIME Petroleum Transactions, v.186, p. 39-48.

Roberts, S.P., Macdonald, P.J. and Tritchard, T., 1995, A bulk and spatially resolved NMR relaxation study of sandstone rock plugs: Journal of Magnetic Resonance, v.116, no.2, p.189-195.

Rollinson, H.R., 1993, Using geochemical data: Evaluation, presentation, interpretation: Prentice Hall, Pearson Education Limited.

Schowalter, T.T., 1979, Mechanics of secondary hydrocarbon migration and entrapment: AAPG Bulletin, v.63, p.723-760.

Seevers, D.O., 1966, A nuclear magnetic method for determining the permeability of sandstone, paper L, in 7th annual logging symposium transactions: Society of Professional Well Log Analysts, 14 p.

Sen, P.N., Straley, C., Kenyon, W.E., and Whittingham, M.S., 1990, Surface-to-volume ratio, charge density, nuclear magnetic relaxation, and permeability in clay-bearing sandstones: Geophysics, v. 55, no. 1, p. 61-69.

Shafer, J.L., Mardon, D. and Gardner, J., 1999, Diffusion effects on NMR response of oil & water in rock: Impact of internal gradients, paper SCA-9916, in International Symposium of the Society of Core Analysts: Montpellier, France.

Stegemeier, G.L., 1977, Mechanisms of entrapment and mobilization of oil in porous media, *in*, Shah, D.O. and Schechter, R.S., eds., Improved oil recovery by surfactant and polymer flooding: New York, Academic Press, p.55-91.

Timur, A., 1968, Effective porosity and permeability of sandstones investigated through nuclear magnetic principles, paper K, in 9th annual logging symposium transactions: Society of Professional Well Log Analysts, 18 p. Later published in 1969: The Log Analyst, v. 10, no. 1, January-February, p. 3-11.

Trewin, N., 1988, Use of the scanning electron microscope in Sedimentology, *in* M. Tucker, ed., Techniques in Sedimentology: Blackwell Scientific Publications, 8, p.229-273.

Vavra, C.L., Kaldi, J.G. and Sneider, R.M., 1992, Geological Applications of Capillary Pressure: A Review: AAPG Bulletin, v.76, p. 840-850.

Washburn, E. W., 1921, The Dynamics of Capillary Flow: Physical Review, v.17, p.273-283.

Zhang, G.Q., Hirasaki, G.J. and House, W.V., 1998, Diffusion in internal field gradients, paper SCA-9823, in International Symposium of the Society of Core Analysts, 10p.

Zhang, G.Q., Hirasaki, G.J., and House, W.V., 2001, Effect of internal field gradients on NMR measurements: Petrophysics, v. 42, no. 1, p. 37-47.

Zhang, G.Q., Hirasaki, G.J. and House, W.V., 2003, Internal field gradients in porous media: Petrophysics, v.44, no. 6, p.422-434.

APPENDIX – A

Mercury Injection Capillary Pressure Data Results

Sample REDMAN-1, D/**2837.57**m log-depth (2833.76m core-depth)

Sample Weight	3.7330
Pen. Weight:	63.5670
Assembly Weight:	251.2720
Hg Surface Tension:	485.0000
Pen. Volume:	15.2197
Stem Volume:	0.3800
Hg Density:	13.5335
Hg volume	-
Sample volume	-
Bulk density	2.2960
Skeletal volume	-
Grain density	2.5195
Porosity	8.8719
% Intrusion	38.0000

Intrusion	Data	Summary				
(From	Pressure	2	to	61000	psia)	
Total	Intrusion	Volume	=	0.0386	mL/g	
Total	Pore	Area	=	13.048	m^2/g	
Median	Pore	Diameter	(Volume)	=	0.0151	µm
Median	Pore	Diameter	(Area)	=	0.0061	µm
Average	Pore	Diameter	(4V/A)	=	0.0118	µm
Bulk	Density	=	2.296	g/mL		
Apparent	(skeletal)	Density	=	2.5195	g/mL	
Porosity	=	8.8719	%			
Stem	Volume	Used	=	38	%	

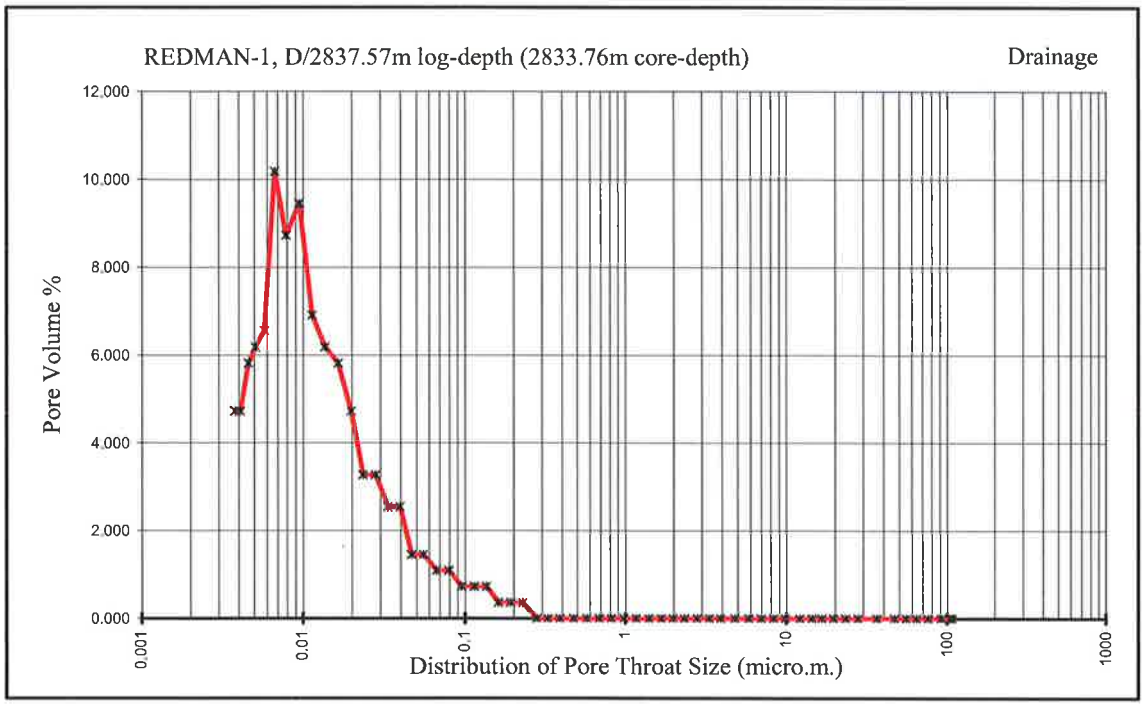
REDMAN-1, D/2837.57m log-depth (2833.76m core-depth)
Drainage
Pore Volume %
12.000
10.000
8.000
6.000
4.000
2.000
0.000
0.001
0.01
0.1
1
10
100
1000
Distribution of Pore Throat Size (micro.m.)

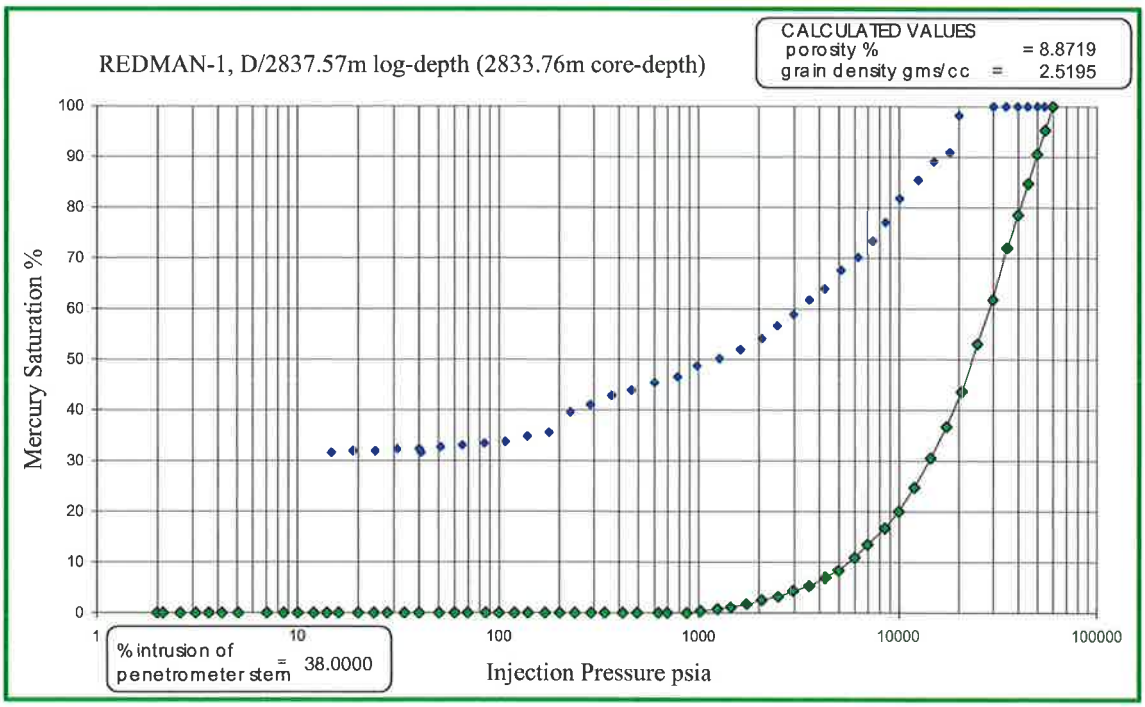
REDMAN-1, D/2837.57m log-depth (2833.76m core-depth)
CALCULATED VALUES
porosity % = 8.8719
grain density gms/cc = 2.5195
Mercury Saturation %
100
90
80
70
60
50
40
30
20
10
0
1
10
100
1000
10000
100000
% intrusion of penetrometer stem = 38.0000
Injection Pressure psia

Sample REDMAN-1, D/**2840.66**m log-depth (2836.85m core-depth)

Sample Weight	10.5430
Pen. Weight:	61.7200
Assembly Weight:	230.2290
Hg Surface Tension:	485.0000
Pen. Volume:	15.8813
Stem Volume:	1.1000
Hg Density:	13.5335
Hg volume	-
Sample volume	-
Bulk density	2.5048
Skeletal volume	-
Grain density	2.6738
Porosity	6.3184
% Intrusion	24.0000

Intrusion	Data	Summary				
(From	Pressure	2	to	61000	psia)	
Total	Intrusion	Volume	=	0.0252	mL/g	
Total	Pore	Area	=	7.377	m^2/g	
Median	Pore	Diameter	(Volume)	=	0.0173	µm
Median	Pore	Diameter	(Area)	=	0.0081	µm
Average	Pore	Diameter	(4V/A)	=	0.0137	µm
Bulk	Density	=	2.5048	g/mL		
Apparent	(skeletal)	Density	=	2.6738	g/mL	
Porosity	=	6.3184	%			
Stem	Volume	Used	=	24	%	

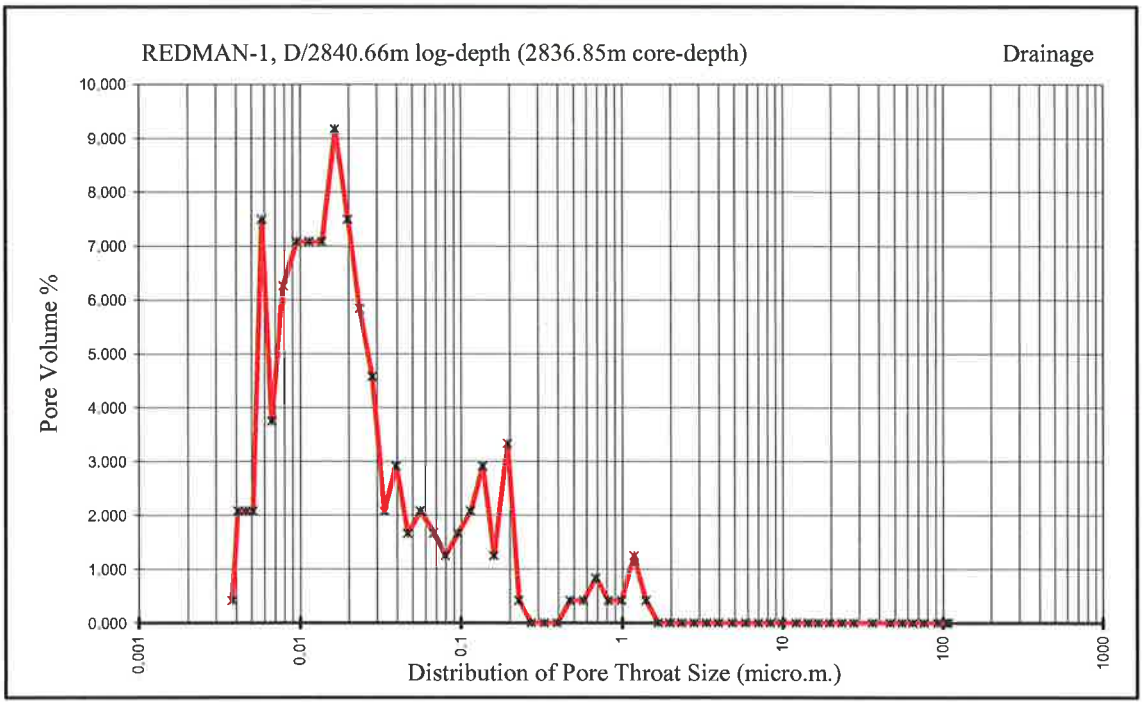
REDMAN-1, D/2840.66m log-depth (2836.85m core-depth)
Drainage
Pore Volume %
10.000
9.000
8.000
7.000
6.000
5.000
4.000
3.000
2.000
1.000
0.000
0.001
0.01
0.1
1
10
100
1000
Distribution of Pore Throat Size (micro.m.)

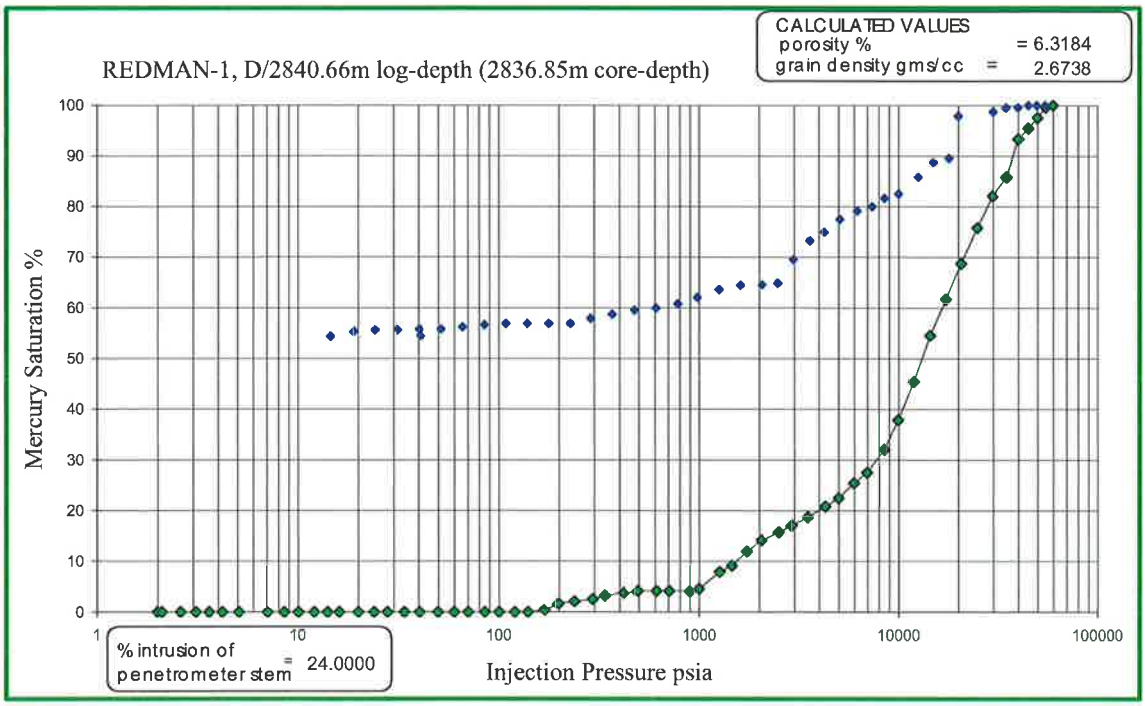
CALCULATED VALUES
porosity % = 6.3184
grain density gms/cc = 2.6738
REDMAN-1, D/2840.66m log-depth (2836.85m core-depth)
Mercury Saturation %
100
90
80
70
60
50
40
30
20
10
0
1
10
100
1000
10000
100000
% intrusion of penetrometer stem = 24.0000
Injection Pressure psia

Sample REDMAN-1, D/**2840.86**m log-dpeth (2837.05m core depth)

Sample Weight	4.7820
Pen. Weight:	63.3830
Assembly Weight:	248.6480
Hg Surface Tension:	485.0000
Pen. Volume:	15.2197
Stem Volume:	0.3800
Hg Density:	13.5335
Hg volume	-
Sample volume	-
Bulk density	2.5386
Skeletal volume	-
Grain density	2.7427
Porosity	7.4388
% Intrusion	37.0000

Intrusion	Data	Summary				
(From	Pressure	2	to	61000	psia)	
Total	Intrusion	Volume	=	0.0293	mL/g	
Total	Pore	Area	=	9.42	m^2/g	
Median	Pore	Diameter	(Volume)	=	0.0152	µm
Median	Pore	Diameter	(Area)	=	0.0071	µm
Average	Pore	Diameter	(4V/A)	=	0.0124	µm
Bulk	Density	=	2.5386	g/mL		
Apparent	(skeletal)	Density	=	2.7427	g/mL	
Porosity	=	7.4388	%			
Stem	Volume	Used	=	37	%	

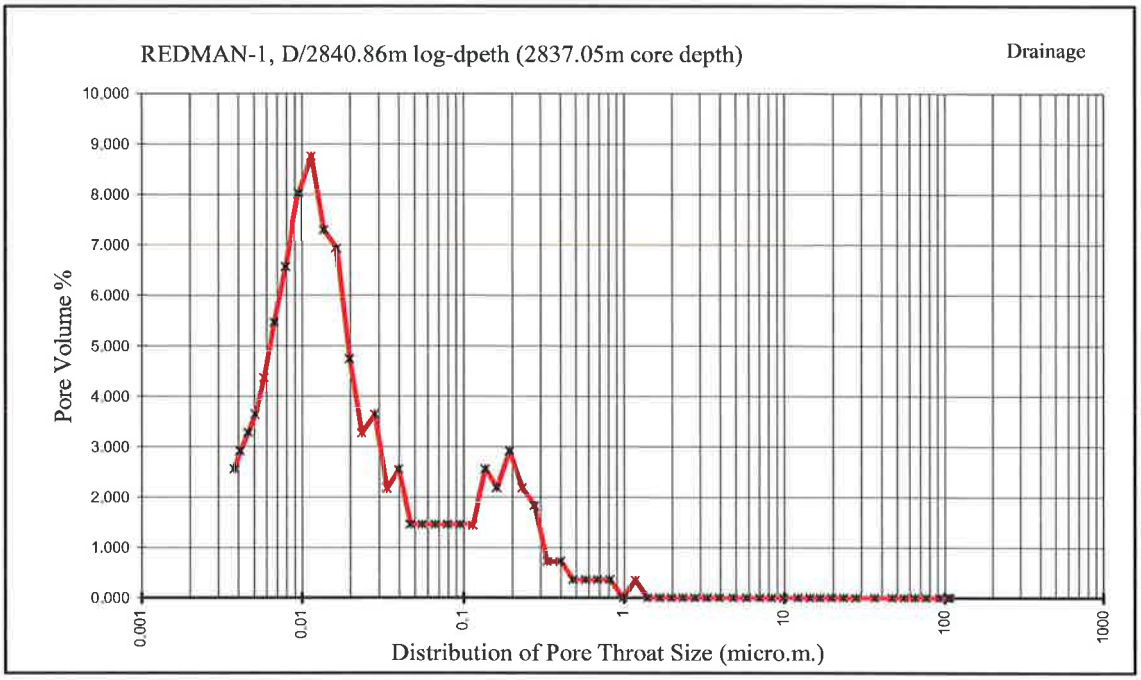
REDMAN-1, D/2840.86m log-dpeth (2837.05m core depth)
Drainage
Pore Volume %
10.000
9.000
8.000
7.000
6.000
5.000
4.000
3.000
2.000
1.000
0.000
0.001
0.01
0.1
1
10
100
1000
Distribution of Pore Throat Size (micro.m.)

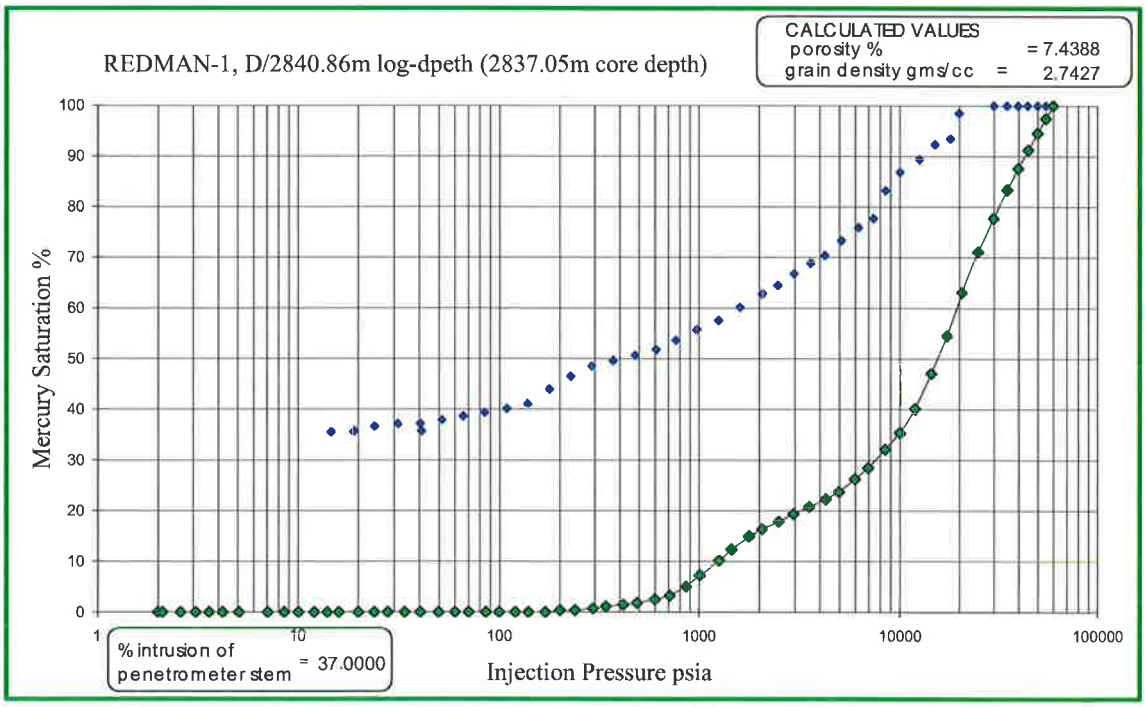
REDMAN-1, D/2840.86m log-dpeth (2837.05m core depth)
CALCULATED VALUES
porosity % = 7.4388
grain density gms/cc = 2.7427
Mercury Saturation %
100
90
80
70
60
50
40
30
20
10
0
1
10
100
1000
10000
100000
% intrusion of penetrometer stem = 37.0000
Injection Pressure psia

Sample REDMAN-1, D/**2841.21**m log-depth (2837.40m core-depth)

Sample Weight	5.6310
Pen. Weight:	63.6870
Assembly Weight:	246.2570
Hg Surface Tension:	485.0000
Pen. Volume:	15.2197
Stem Volume:	0.3800
Hg Density:	13.5335
Hg volume	-
Sample volume	-
Bulk density	2.6245
Skeletal volume	-
Grain density	2.7692
Porosity	5.2261
% Intrusion	30.0000

Intrusion	Data	Summary				
(From	Pressure	2	to	61000	psia)	
Total	Intrusion	Volume	=	0.0199	mL/g	
Total	Pore	Area	=	6.833	m^2/g	
Median	Pore	Diameter	(Volume)	=	0.0139	µm
Median	Pore	Diameter	(Area)	=	0.0076	µm
Average	Pore	Diameter	(4V/A)	=	0.0117	µm
Bulk	Density	=	2.6245	g/mL		
Apparent	(skeletal)	Density	=	2.7692	g/mL	
Porosity	=	5.2261	%			
Stem	Volume	Used	=	30	%	

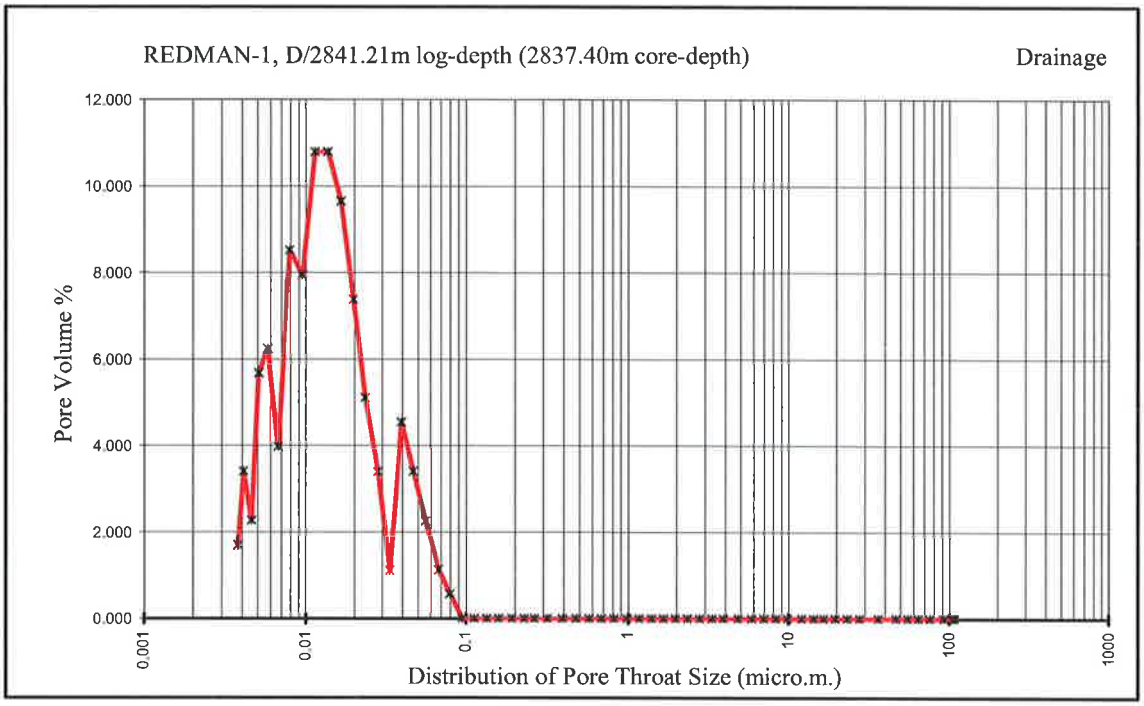
REDMAN-1, D/2841.21m log-depth (2837.40m core-depth)
Drainage
Pore Volume %
12.000
10.000
8.000
6.000
4.000
2.000
0.000
0.001
0.01
0.1
1
10
100
1000
Distribution of Pore Throat Size (micro.m.)

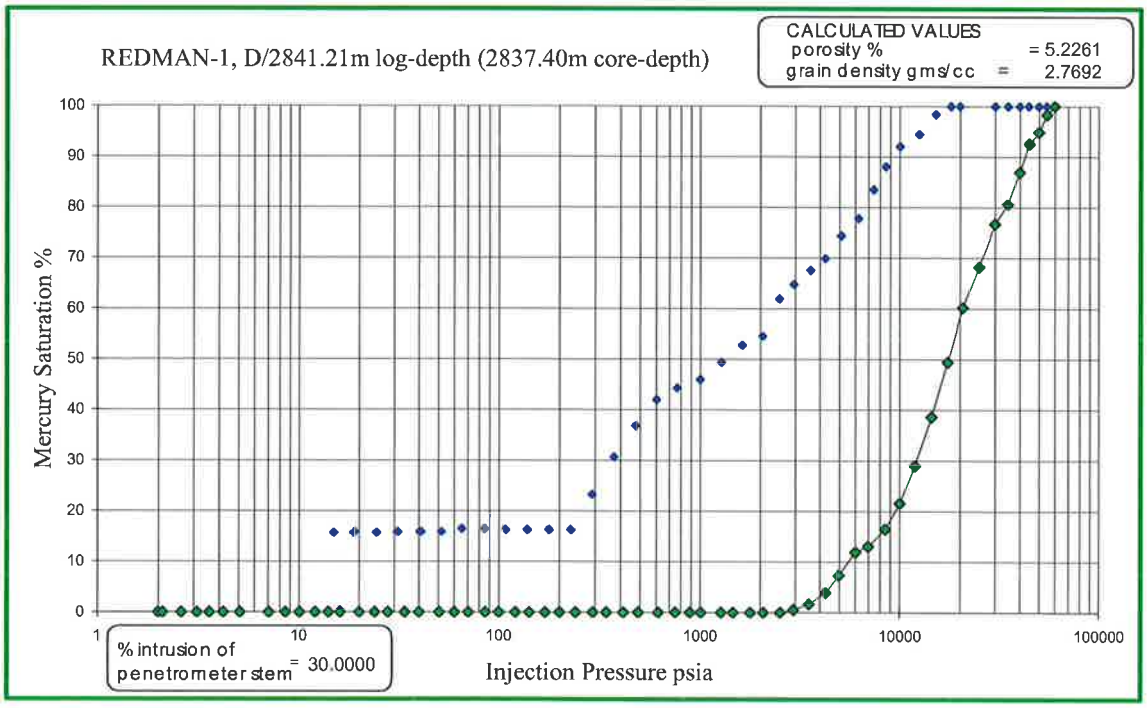
REDMAN-1, D/2841.21m log-depth (2837.40m core-depth)
CALCULATED VALUES
porosity % = 5.2261
grain density gms/cc = 2.7692
Mercury Saturation %
100
90
80
70
60
50
40
30
20
10
0
1
10
100
1000
10000
100000
% intrusion of penetrometer stem = 30.0000
Injection Pressure psia

Sample REDMAN-1 D/**2841.3**m log-depth (2837.49m core-depth)

Sample Weight	5.5640
Pen. Weight:	63.7290
Assembly Weight:	245.6430
Hg Surface Tension:	485.0000
Pen. Volume:	15.2197
Stem Volume:	0.3800
Hg Density:	13.5335
Hg volume	-
Sample volume	-
Bulk density	2.5417
Skeletal volume	-
Grain density	2.6989
Porosity	5.8226
% Intrusion	34.0000

Intrusion	Data	Summary				
(From	Pressure	2	to	61000	psia)	
Total	Intrusion	Volume	=	0.0229	mL/g	
Total	Pore	Area	=	12.741	m^2/g	
Median	Pore	Diameter	(Volume)	=	0.0066	µm
Median	Pore	Diameter	(Area)	=	0.0048	µm
Average	Pore	Diameter	(4V/A)	=	0.0072	µm
Bulk	Density	=	2.5417	g/mL		
Apparent	(skeletal)	Density	=	2.6989	g/mL	
Porosity	=	5.8226	%			
Stem	Volume	Used	=	34	%	

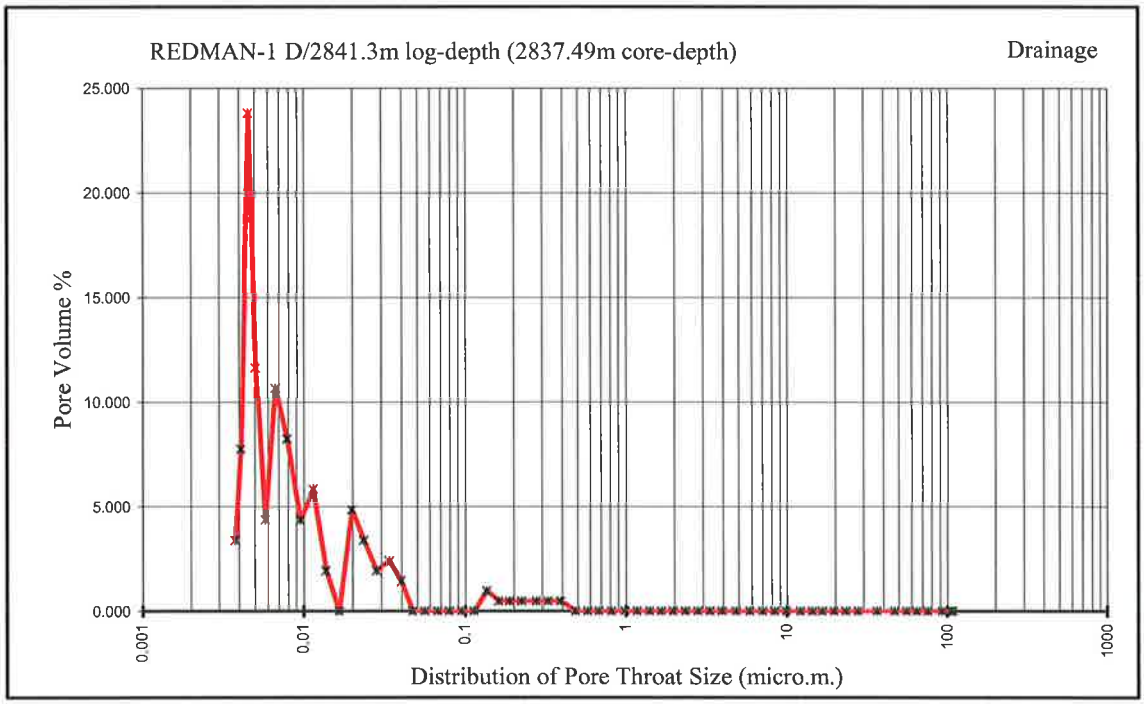
REDMAN-1 D/2841.3m log-depth (2837.49m core-depth)
Drainage
Pore Volume %
25.000
20.000
15.000
10.000
5.000
0.000
0.001
0.01
0.1
1
10
100
1000
Distribution of Pore Throat Size (micro.m.)

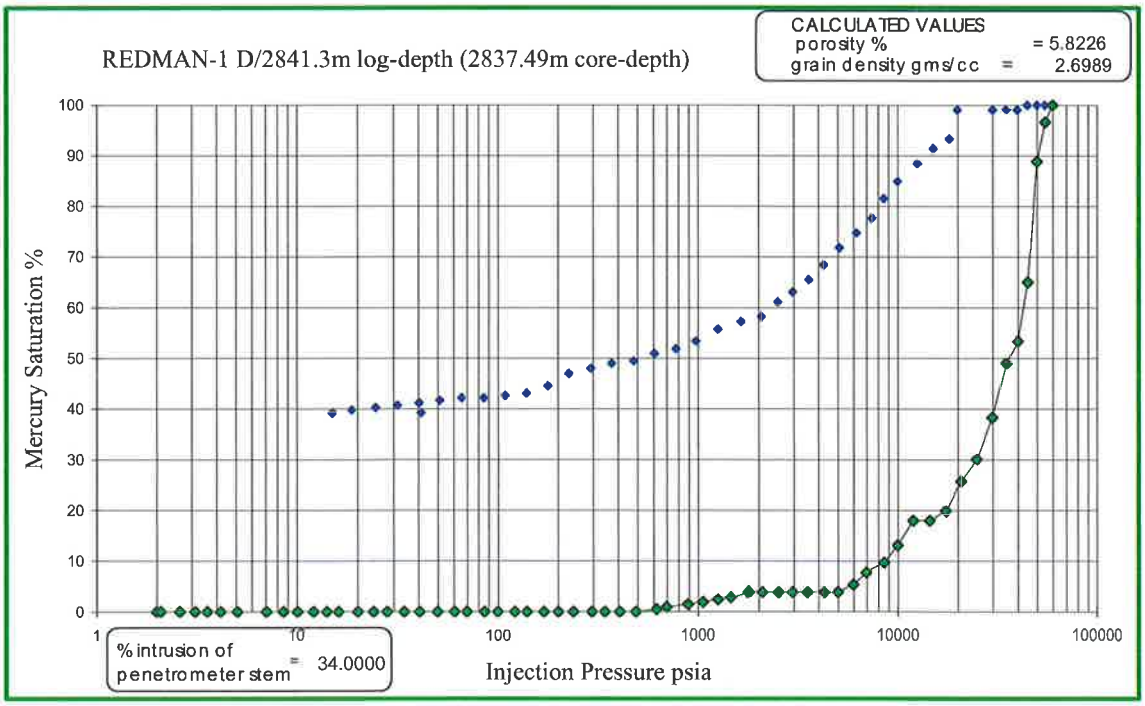
REDMAN-1 D/2841.3m log-depth (2837.49m core-depth)
CALCULATED VALUES
porosity % = 5.8226
grain density gms/cc = 2.6989
Mercury Saturation %
100
90
80
70
60
50
40
30
20
10
0
1
10
100
1000
10000
100000
% intrusion of penetrometer stem = 34.0000
Injection Pressure psia

Sample REDMAN-1 D/**2841.66**m log-depth (2837.85m core-depth)

Sample Weight	4.9210
Pen. Weight:	64.7960
Assembly Weight:	236.5550
Hg Surface Tension:	485.0000
Pen. Volume:	14.3206
Stem Volume:	0.3800
Hg Density:	13.5335
Hg volume	-
Sample volume	-
Bulk density	2.4694
Skeletal volume	-
Grain density	2.6163
Porosity	5.6157
% Intrusion	29.0000

Intrusion	Data	Summary				
(From	Pressure	2	to	61000	psia)	
Total	Intrusion	Volume	=	0.0227	mL/g	
Total	Pore	Area	=	11.945	m^2/g	
Median	Pore	Diameter	(Volume)	=	0.0075	µm
Median	Pore	Diameter	(Area)	=	0.0054	µm
Average	Pore	Diameter	(4V/A)	=	0.0076	µm
Bulk	Density	=	2.4694	g/mL		
Apparent	(skeletal)	Density	=	2.6163	g/mL	
Porosity	=	5.6157	%			
Stem	Volume	Used	=	29	%	

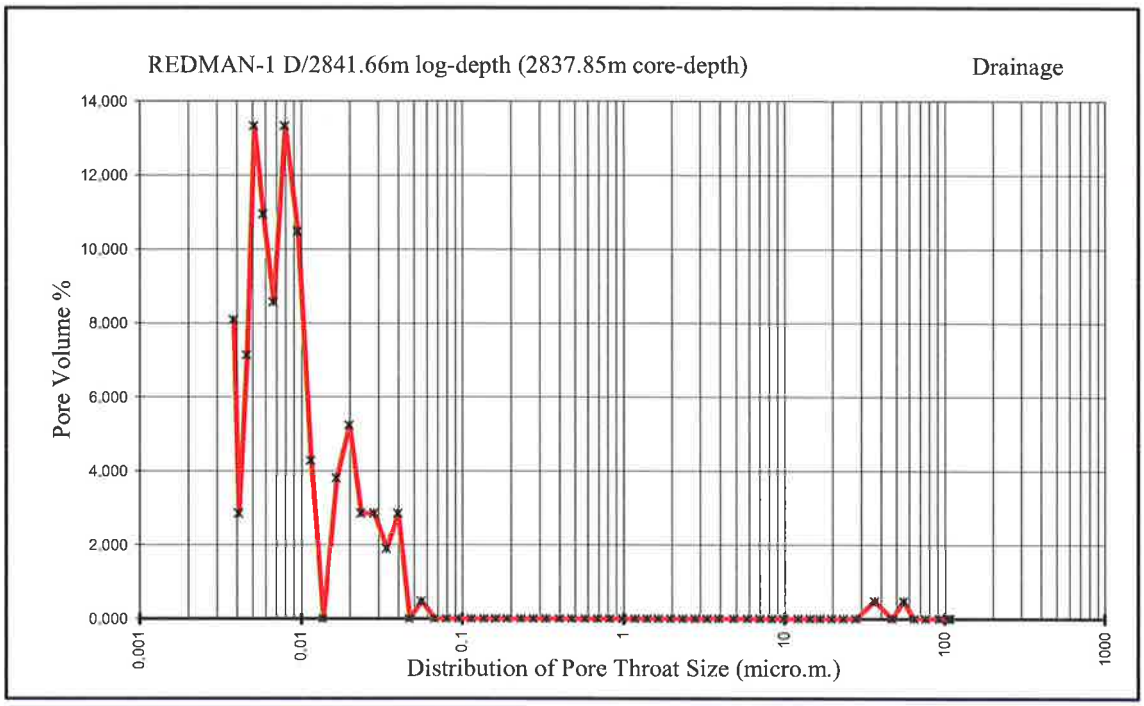
REDMAN-1 D/2841.66m log-depth (2837.85m core-depth)
Drainage
Pore Volume %
14,000
12,000
10,000
8,000
6,000
4,000
2,000
0,000
0,001
0,01
0,1
1
10
100
1000
Distribution of Pore Throat Size (micro.m.)

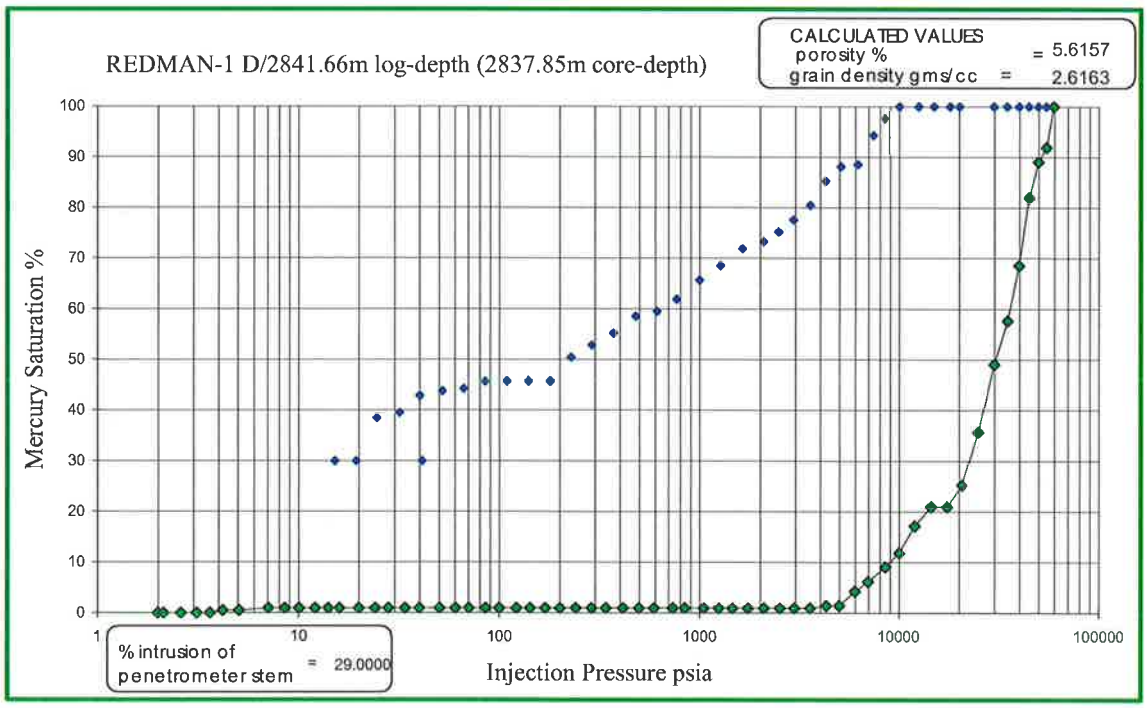
REDMAN-1 D/2841.66m log-depth (2837.85m core-depth)
CALCULATED VALUES
porosity % = 5.6157
grain density gms/cc = 2.6163
Mercury Saturation %
100
90
80
70
60
50
40
30
20
10
0
1
10
100
1000
10000
100000
% intrusion of penetrometer stem = 29.0000
Injection Pressure psia

Sample	REDMAN-1 D/**2841.99**m log-depth (2838.18m core-depth)

Sample Weight	4.3280
Pen. Weight:	63.6100
Assembly Weight:	250.8910
Hg Surface Tension:	485.0000
Pen. Volume:	15.2197
Stem Volume:	0.3800
Hg Density:	13.5335
Hg volume	-
Sample volume	-
Bulk density	2.5441
Skeletal volume	-
Grain density	2.6947
Porosity	5.5865
% Intrusion	25.0000

Intrusion	Data	Summary				
(From	Pressure	2	to	61000	psia)	
Total	Intrusion	Volume	=	0.022	mL/g	
Total	Pore	Area	=	9.69	m^2/g	
Median	Pore	Diameter	(Volume)	=	0.0101	µm
Median	Pore	Diameter	(Area)	=	0.0061	µm
Average	Pore	Diameter	(4V/A)	=	0.0091	µm
Bulk	Density	=	2.5441	g/mL		
Apparent	(skeletal)	Density	=	2.6947	g/mL	
Porosity	=	5.5865	%			
Stem	Volume	Used	=	25	%	

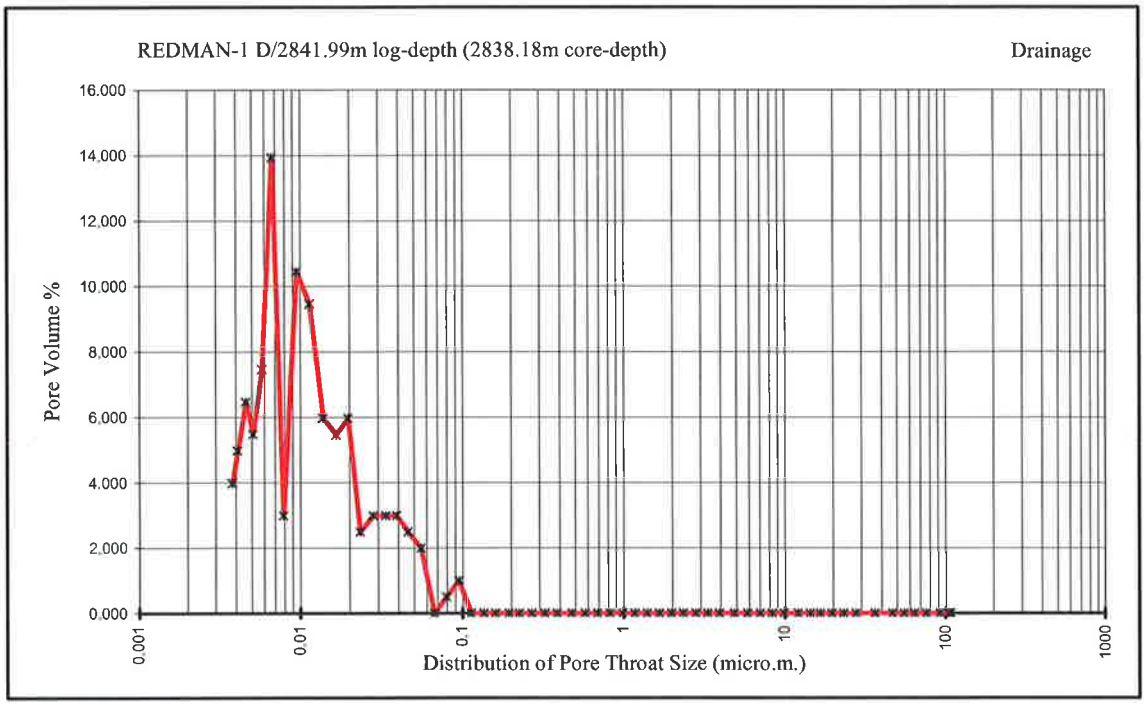
REDMAN-1 D/2841.99m log-depth (2838.18m core-depth)
Drainage
Pore Volume %
16.000
14.000
12.000
10.000
8.000
6.000
4.000
2.000
0.000
0.001
0.01
0.1
1
10
100
1000
Distribution of Pore Throat Size (micro.m.)

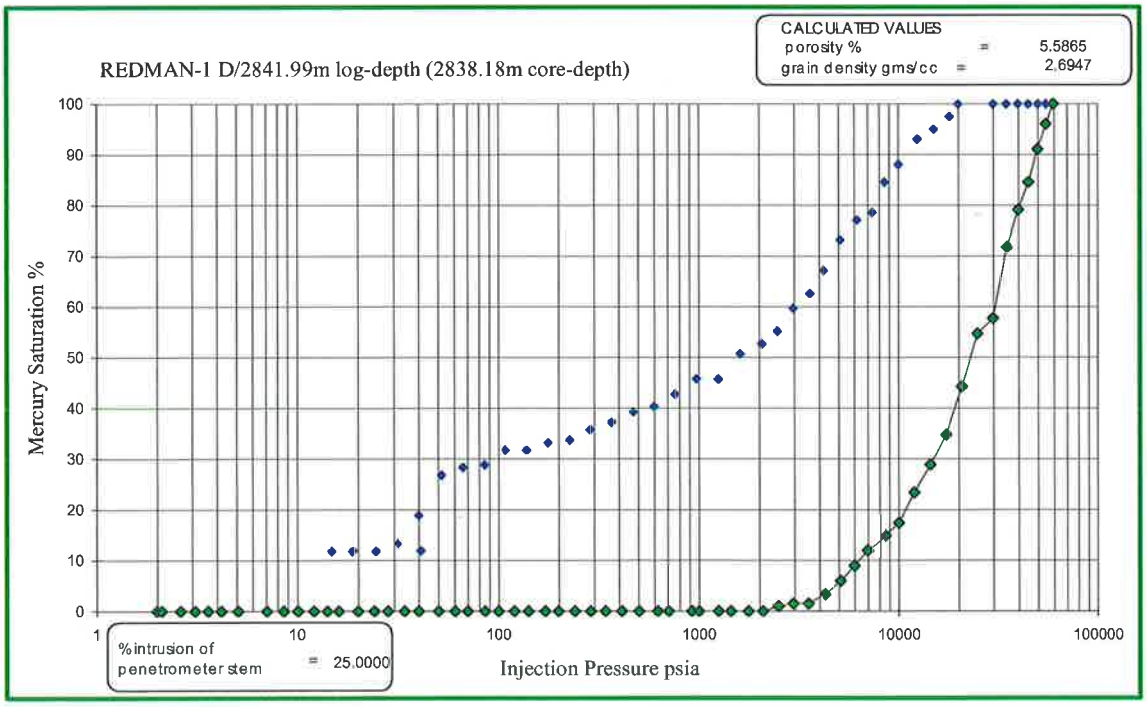
REDMAN-1 D/2841.99m log-depth (2838.18m core-depth)
CALCULATED VALUES
porosity % = 5.5865
grain density gms/cc = 2.6947
Mercury Saturation %
100
90
80
70
60
50
40
30
20
10
0
1
10
100
1000
10000
100000
% intrusion of penetrometer stem = 25.0000
Injection Pressure psia

Sample	REDMAN-1, D/**2843.08**m log-depth (2839.27m core-depth)
Sample Weight	2.6190
Pen. Weight:	62.0990
Assembly Weight:	98.7550
Hg Surface Tension:	485.0000
Pen. Volume:	3.5475
Stem Volume:	0.3920
Hg Density:	13.5335
Hg volume	-
Sample volume	-
Bulk density	2.5366
Skeletal volume	-
Grain density	2.8567
Porosity	11.2061
% Intrusion	30.0000

Intrusion	Data	Summary				
(From	Pressure	2	to	61000	psia)	
Total	Intrusion	Volume	=	0.0442	mL/g	
Total	Pore	Area	=	8.713	m^2/g	
Median	Pore	Diameter	(Volume)	=	0.0454	µm
Median	Pore	Diameter	(Area)	=	0.0096	µm
Average	Pore	Diameter	(4V/A)	=	0.0203	µm
Bulk	Density	=	2.5366	g/mL		
Apparent	(skeletal)	Density	=	2.8567	g/mL	
Porosity	=	11.2061	%			
Stem	Volume	Used	=	30	%	

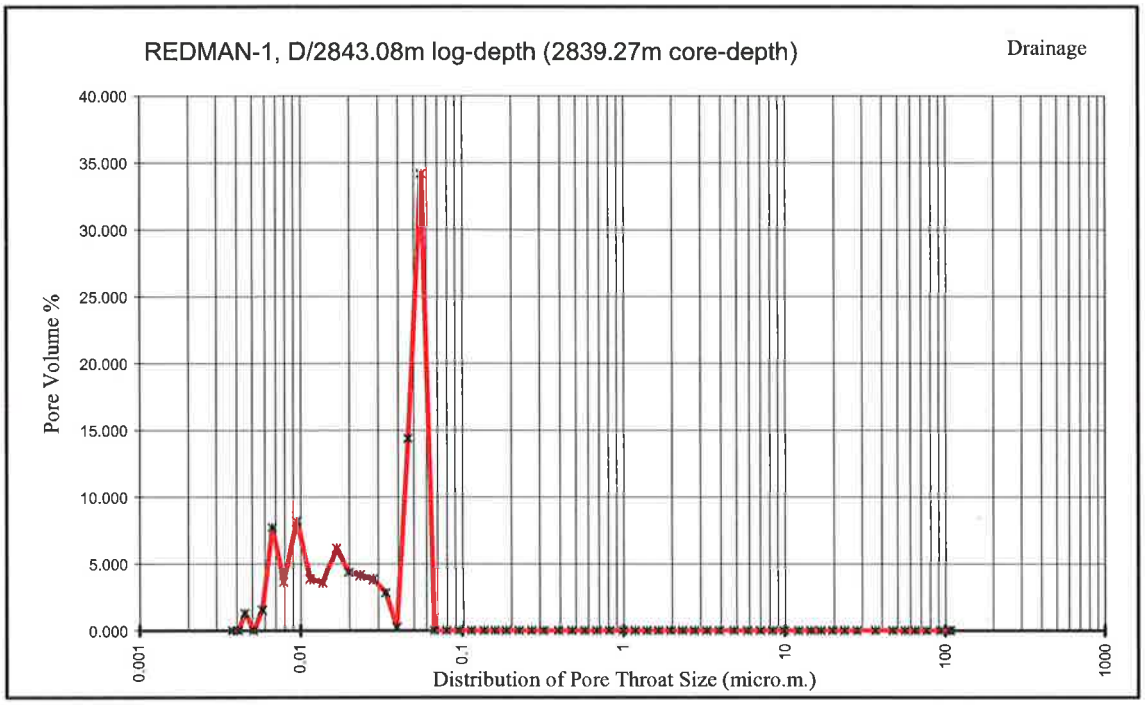
REDMAN-1, D/2843.08m log-depth (2839.27m core-depth)
Drainage
Pore Volume %
40.000
35.000
30.000
25.000
20.000
15.000
10.000
5.000
0.000
0.001
0.01
0.1
1
10
100
1000
Distribution of Pore Throat Size (micro.m.)

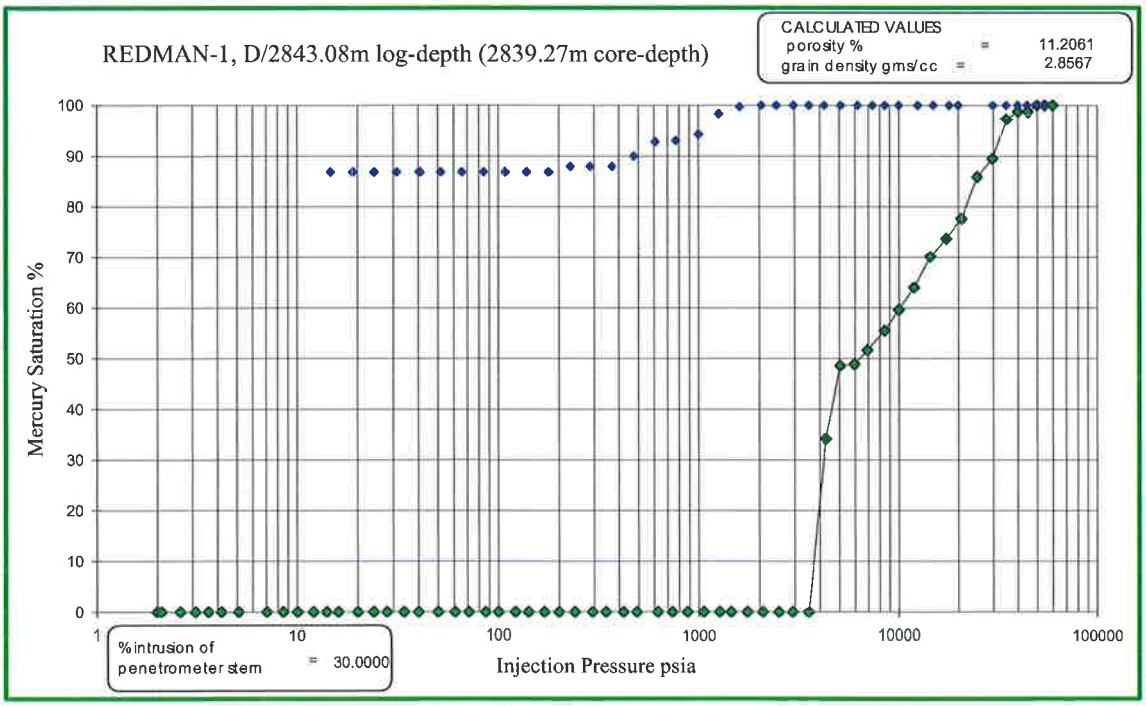
REDMAN-1, D/2843.08m log-depth (2839.27m core-depth)
CALCULATED VALUES
porosity % = 11.2061
grain density gms/cc = 2.8567
Mercury Saturation %
100
90
80
70
60
50
40
30
20
10
0
1
10
100
1000
10000
100000
Injection Pressure psia
%intrusion of penetrometer stem = 30.0000

Sample	REDMAN-1 D/**2843.42**m log-depth (2839.61m core-depth)

Sample Weight	5.2250
Pen. Weight:	63.4250
Assembly Weight:	246.8070
Hg Surface Tension:	485.0000
Pen. Volume:	15.2197
Stem Volume:	0.3800
Hg Density:	13.5335
Hg volume	-
Sample volume	-
Bulk density	2.5419
Skeletal volume	-
Grain density	2.7096
Porosity	6.1875
% Intrusion	33.0000

Intrusion	Data	Summary				
(From	Pressure	2	to	61000	psia)	
Total	Intrusion	Volume	=	0.0243	mL/g	
Total	Pore	Area	=	10.834	m^2/g	
Median	Pore	Diameter	(Volume)	=	0.0097	µm
Median	Pore	Diameter	(Area)	=	0.0064	µm
Average	Pore	Diameter	(4V/A)	=	0.009	µm
Bulk	Density	=	2.5419	g/mL		
Apparent	(skeletal)	Density	=	2.7096	g/mL	
Porosity	=	6.1875	%			
Stem	Volume	Used	=	33	%	

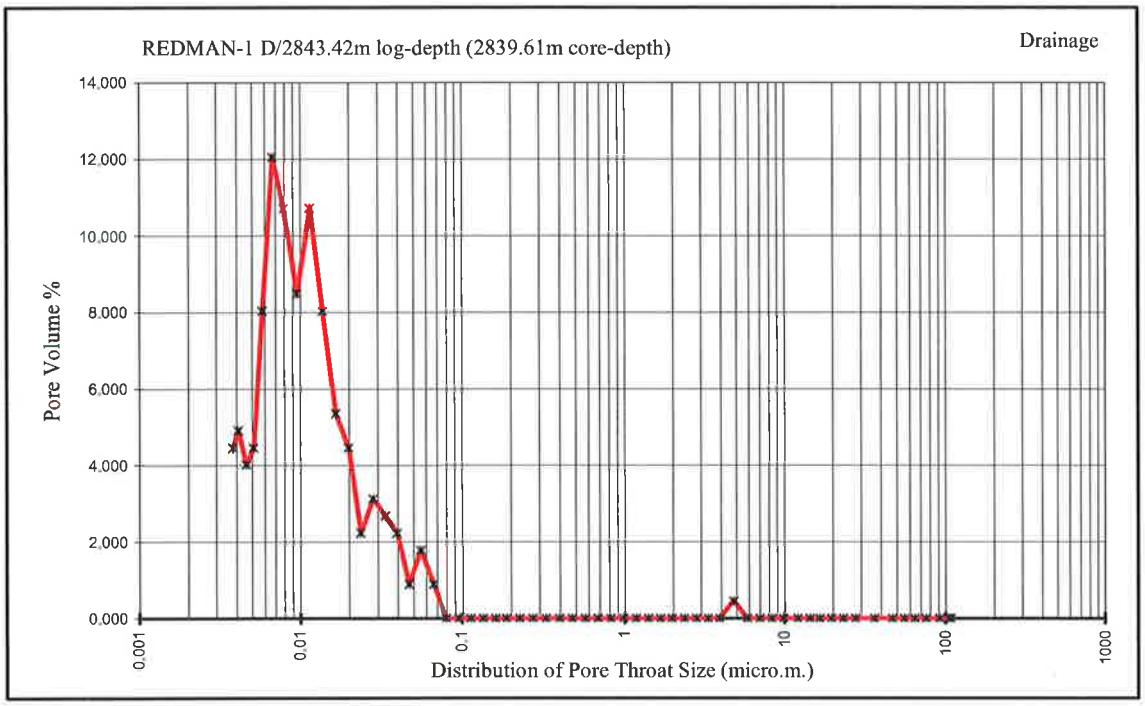
REDMAN-1 D/2843.42m log-depth (2839.61m core-depth)
Drainage
Pore Volume %
14.000
12.000
10.000
8.000
6.000
4.000
2.000
0.000
0.001
0.01
0.1
1
10
100
1000
Distribution of Pore Throat Size (micro.m.)

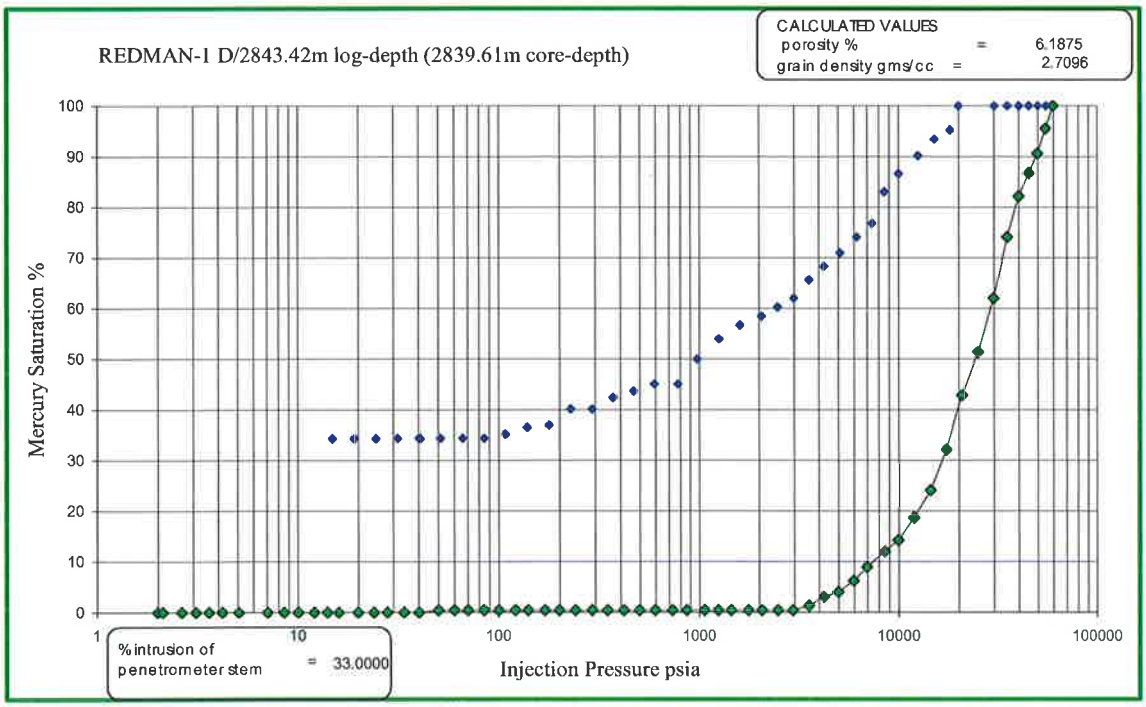
REDMAN-1 D/2843.42m log-depth (2839.61m core-depth)
CALCULATED VALUES
porosity % = 6.1875
grain density gms/cc = 2.7096
Mercury Saturation %
100
90
80
70
60
50
40
30
20
10
0
1
10
100
1000
10000
100000
Injection Pressure psia
% intrusion of penetrometer stem = 33.0000

Sample	REDMAN-1, D/**2843.61**m log-depth (2839.80m core-depth)
Date	12/15/2004
Sample Weight	5.0650
Pen. Weight:	63.5540
Assembly Weight:	246.0360
Hg Surface Tension:	485.0000
Pen. Volume:	15.2197
Stem Volume:	0.3800
Hg Density:	13.5335
Hg volume	-
Sample volume	-
Bulk density	2.4002
Skeletal volume	-
Grain density	2.5983
Porosity	7.6232
% Intrusion	42.0000

Intrusion	Data	Summary				
(From	Pressure	2	to	61000	psia)	
Total	Intrusion	Volume	=	0.0318	mL/g	
Total	Pore	Area	=	12.908	m^2/g	
Median	Pore	Diameter	(Volume)	=	0.0118	µm
Median	Pore	Diameter	(Area)	=	0.0053	µm
Average	Pore	Diameter	(4V/A)	=	0.0098	µm
Bulk	Density	=	2.4002	g/mL		
Apparent	(skeletal)	Density	=	2.5983	g/mL	
Porosity	=	7.6232	%			
Stem	Volume	Used	=	42	%	

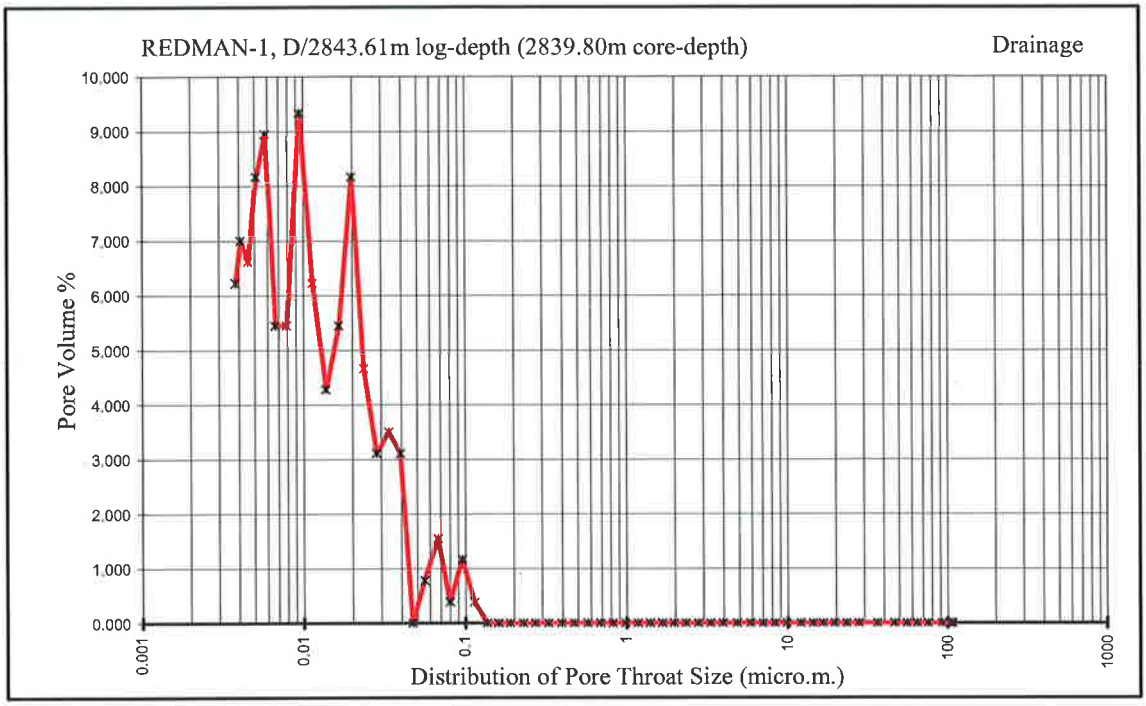
REDMAN-1, D/2843.61m log-depth (2839.80m core-depth)
Drainage
Pore Volume %
10.000
9.000
8.000
7.000
6.000
5.000
4.000
3.000
2.000
1.000
0.000
0.001
0.01
0.1
1
10
100
1000
Distribution of Pore Throat Size (micro.m.)

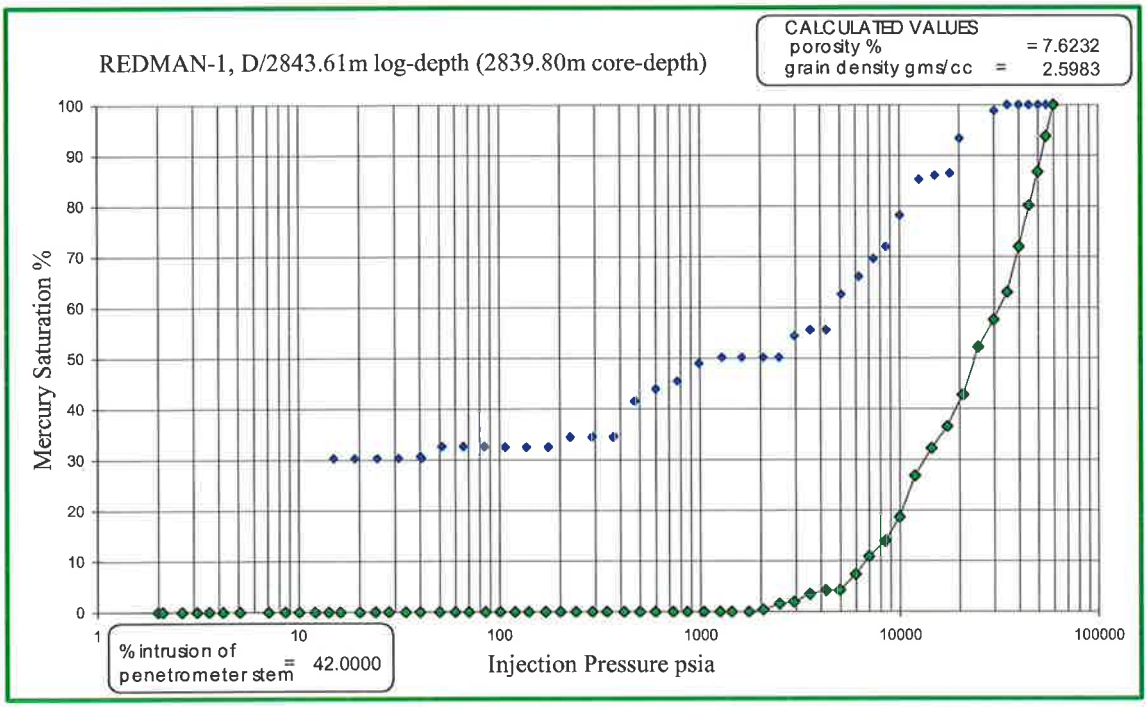
REDMAN-1, D/2843.61m log-depth (2839.80m core-depth)
CALCULATED VALUES
porosity % = 7.6232
grain density gms/cc = 2.5983
Mercury Saturation %
100
90
80
70
60
50
40
30
20
10
0
1
10
100
1000
10000
100000
% intrusion of penetrometer stem = 42.0000
Injection Pressure psia

Sample	REDMAN-1, D/**2844.08**m log-depth (2840.27m core-depth)
Date	12/15/2004
Sample Weight	5.6880
Pen. Weight:	63.5870
Assembly Weight:	244.2790
Hg Surface Tension:	485.0000
Pen. Volume:	15.2197
Stem Volume:	0.3800
Hg Density:	13.5335
Hg volume	-
Sample volume	-
Bulk density	2.4854
Skeletal volume	-
Grain density	2.6565
Porosity	6.4388
% Intrusion	39.0000

Intrusion	Data	Summary				
(From	Pressure	2	to	61000	psia)	
Total	Intrusion	Volume	=	0.0259	mL/g	
Total	Pore	Area	=	10.155	m^2/g	
Median	Pore	Diameter	(Volume)	=	0.0111	µm
Median	Pore	Diameter	(Area)	=	0.0065	µm
Average	Pore	Diameter	(4V/A)	=	0.0102	µm
Bulk	Density	=	2.4854	g/mL		
Apparent	(skeletal)	Density	=	2.6565	g/mL	
Porosity	=	6.4388	%			
Stem	Volume	Used	=	39	%	

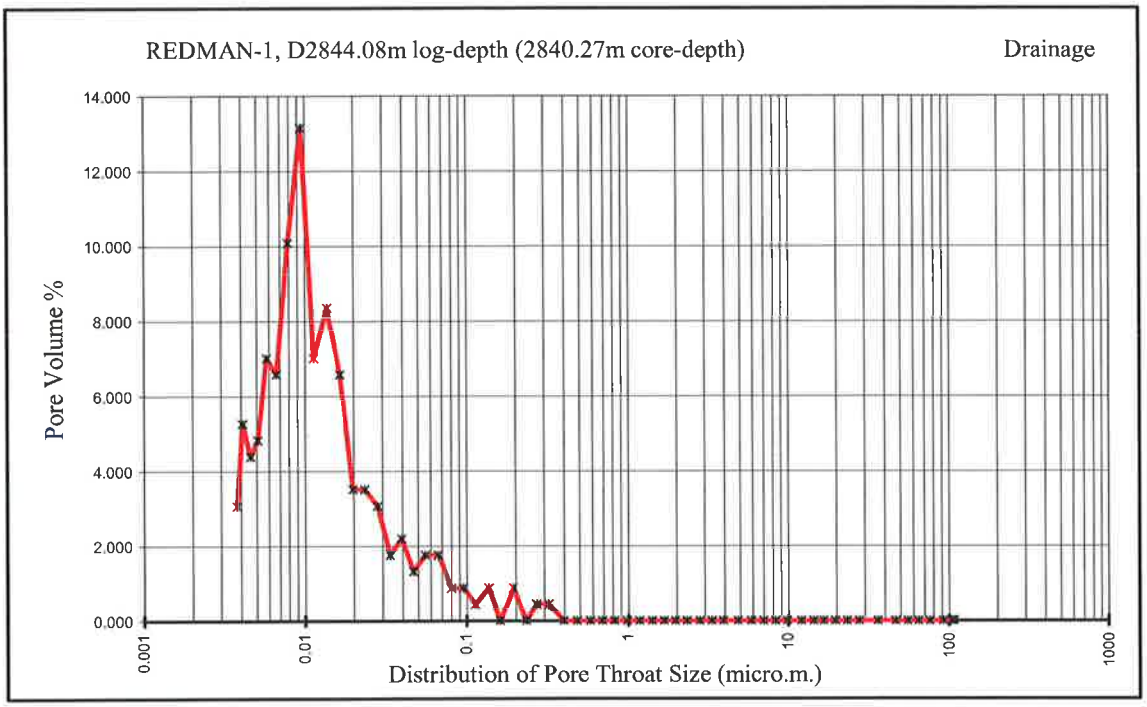
REDMAN-1, D2844.08m log-depth (2840.27m core-depth)
Drainage
Pore Volume %
14.000
12.000
10.000
8.000
6.000
4.000
2.000
0.000
0.001
0.01
0.1
1
10
100
1000
Distribution of Pore Throat Size (micro.m.)

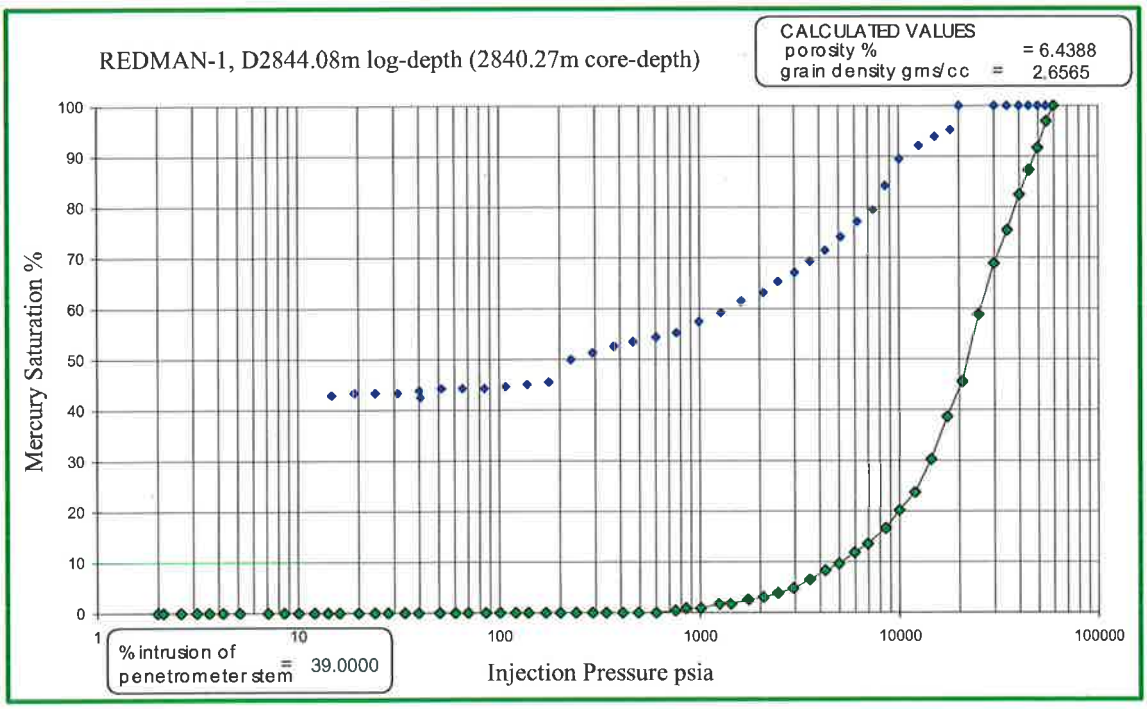
REDMAN-1, D2844.08m log-depth (2840.27m core-depth)
CALCULATED VALUES
porosity % = 6.4388
grain density gms/cc = 2.6565
Mercury Saturation %
100
90
80
70
60
50
40
30
20
10
0
1
10
100
1000
10000
100000
% intrusion of penetrometer stem = 39.0000
Injection Pressure psia

APPENDIX - B

NMR Data Results

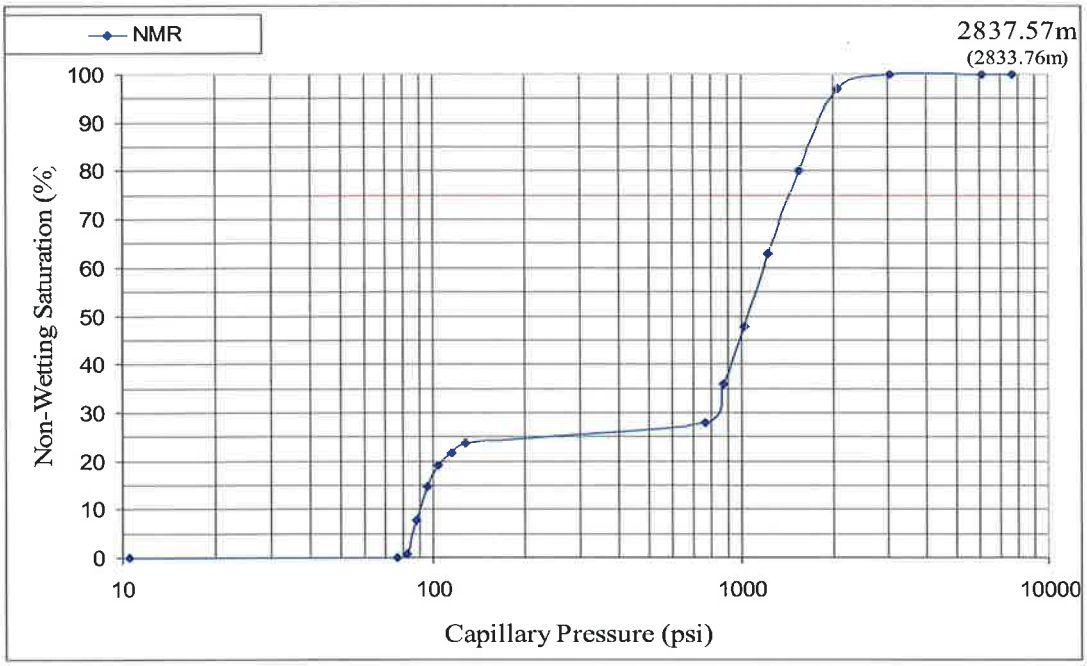

Capillary Pressure (psi)	Non-wetting Saturation (%)
0.767	0.000
0.794	0.000
0.823	0.019
0.855	0.040
0.889	0.041
0.926	0.041
0.967	0.041
7.667	0.042
8.032	0.042
8.433	0.043
8.877	0.043
9.370	0.044
9.922	0.044
10.542	0.044
76.667	0.045
82.143	0.886
88.462	7.748
95.833	14.681
104.545	19.204
115.000	21.590
127.778	23.678
766.667	27.831
876.190	35.792
1022.222	47.876
1226.667	63.166
1533.333	80.061
2044.444	96.835
3066.667	100.000
6133.333	100.000
7666.667	100.000

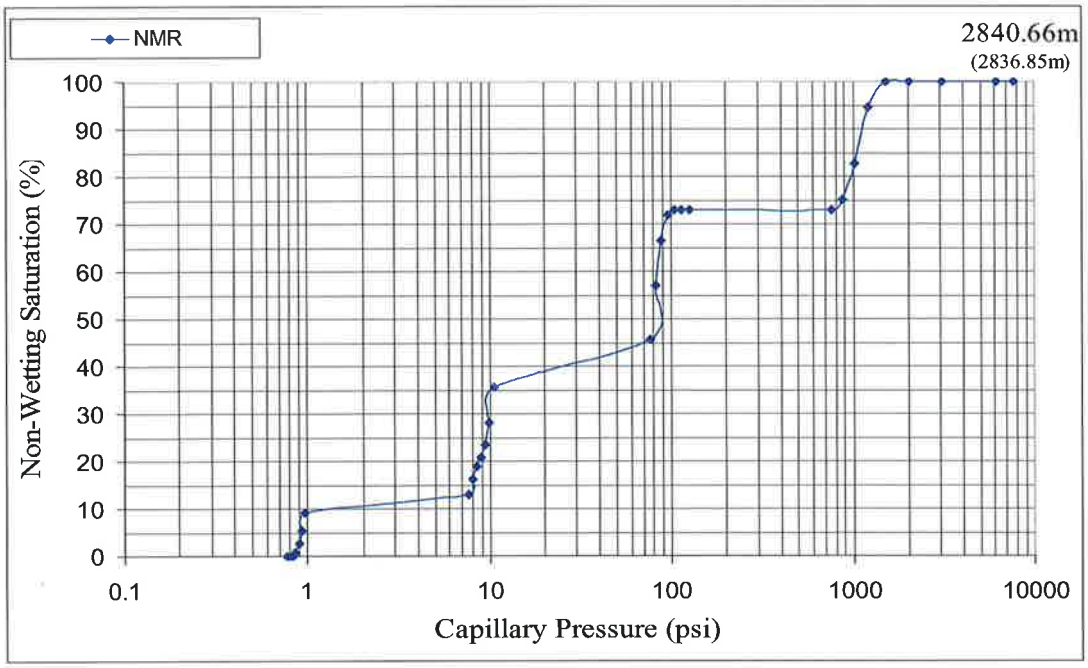

Capillary Pressure (psi)	Non-wetting Saturation (%)
0.767	0.000
0.794	0.000
0.823	0.001
0.855	0.784
0.889	2.570
0.926	5.483
0.967	9.150
7.667	12.968
8.032	16.301
8.433	18.816
8.877	20.854
9.370	23.485
9.922	28.075
10.542	35.548
76.667	45.705
82.143	56.934
88.462	66.570
95.833	72.016
104.545	72.879
115.000	73.008
127.778	73.009
766.667	73.009
876.190	75.078
1022.222	82.574
1226.667	94.586
1533.333	100.000
2044.444	100.000
3066.667	100.000
6133.333	100.000
7666.667	100.000

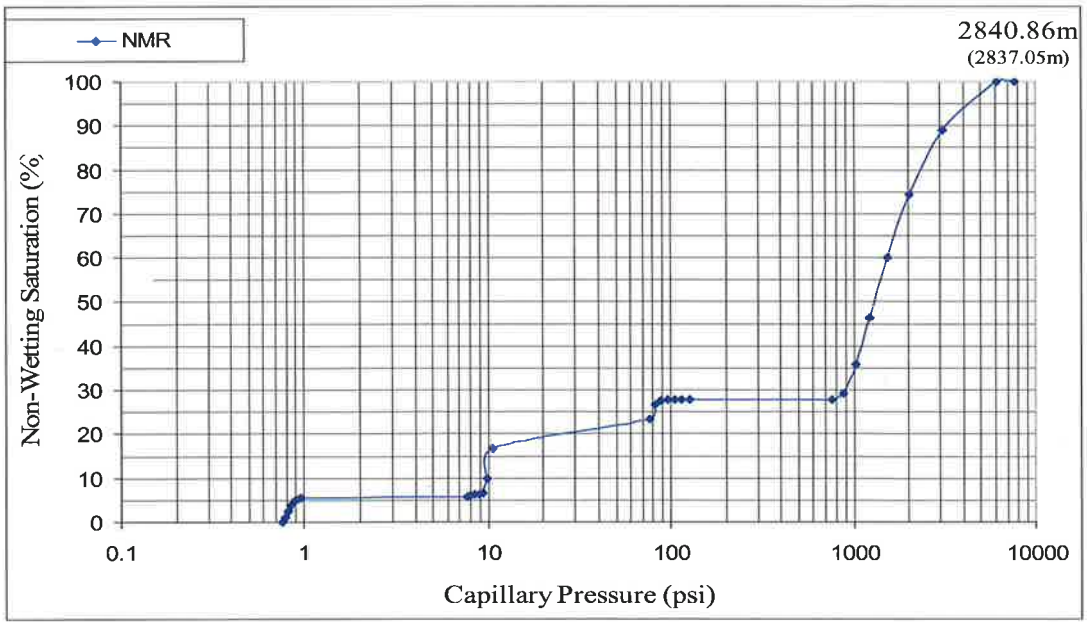

Capillary Pressure (psi)	Non-wetting Saturation (%)
0.767	0.000
0.794	1.134
0.823	2.534
0.855	3.992
0.889	4.903
0.926	5.178
0.967	5.500
7.667	5.812
8.032	6.058
8.433	6.223
8.877	6.362
9.370	6.591
9.922	9.800
10.542	16.738
76.667	23.347
82.143	26.651
88.462	27.491
95.833	27.913
104.545	27.914
115.000	27.914
127.778	27.914
766.667	27.915
876.190	29.237
1022.222	35.843
1226.667	46.609
1533.333	59.947
2044.444	74.398
3066.667	88.931
6133.333	100.000
7666.667	100.000

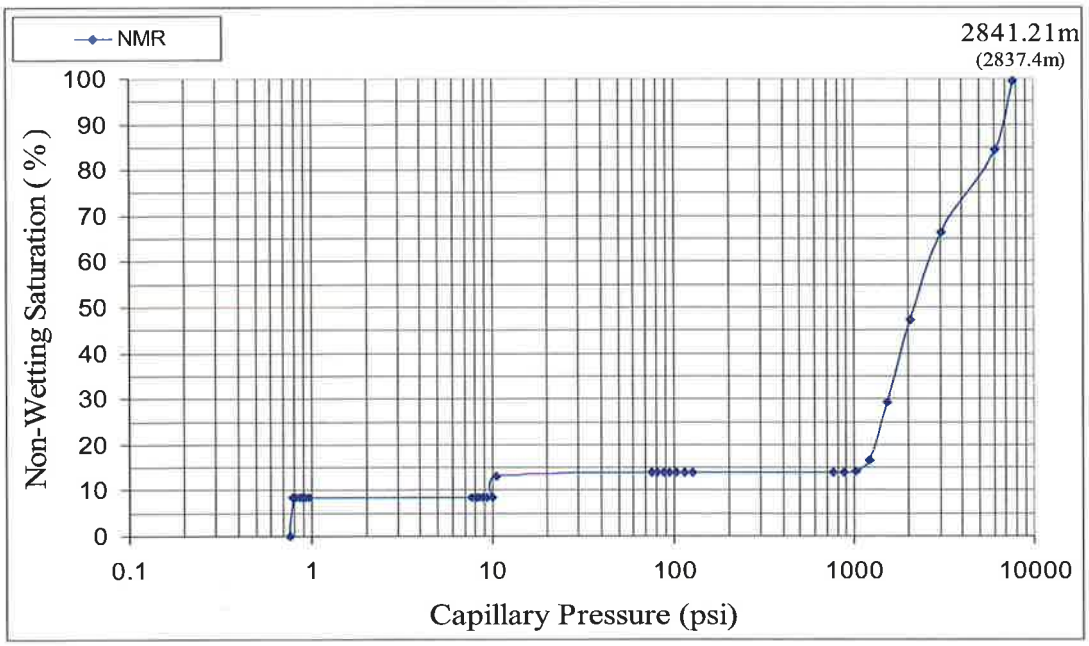

Capillary Pressure (psi)	Non-wetting Saturation (%)
0.767	0.000
0.794	8.519
0.823	8.519
0.855	8.520
0.889	8.520
0.926	8.521
0.967	8.521
7.667	8.522
8.032	8.522
8.433	8.523
8.877	8.523
9.370	8.524
9.922	8.524
10.542	13.036
76.667	13.814
82.143	13.814
88.462	13.815
95.833	13.815
104.545	13.816
115.000	13.816
127.778	13.817
766.667	13.817
876.190	13.818
1022.222	14.079
1226.667	16.652
1533.333	29.306
2044.444	47.178
3066.667	66.406
6133.333	84.348
7666.667	99.542

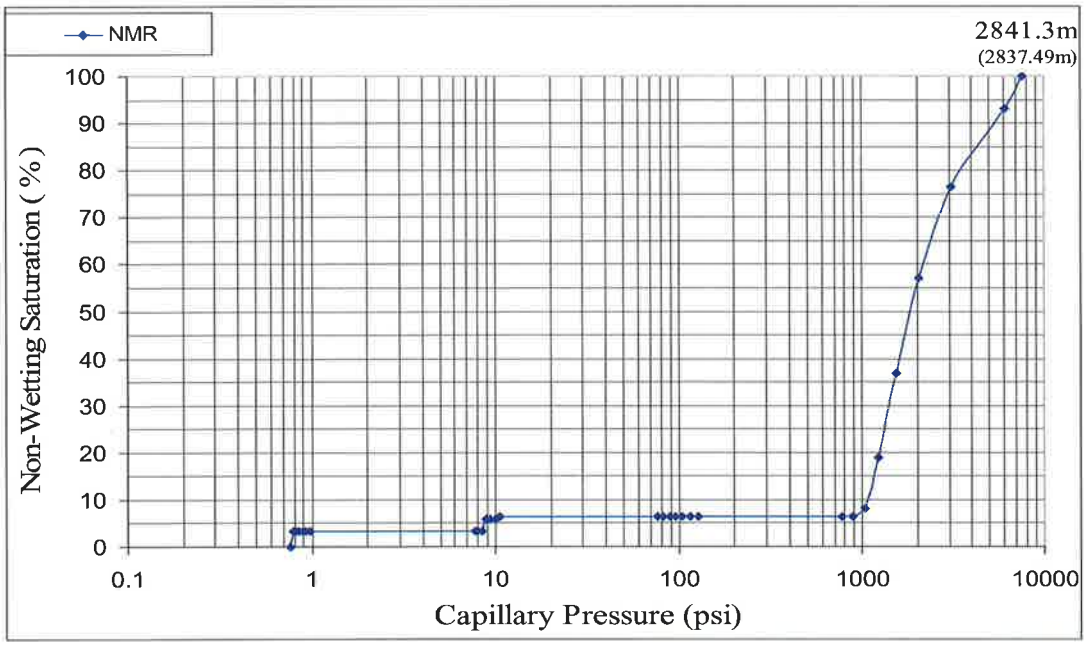

Capillary Pressure (psi)	Non-wetting Saturation (%)
0.767	0.000
0.794	3.401
0.823	3.402
0.855	3.402
0.889	3.403
0.926	3.403
0.967	3.404
7.667	3.404
8.032	3.405
8.433	3.405
8.877	5.928
9.370	5.928
9.922	5.929
10.542	6.474
76.667	6.475
82.143	6.476
88.462	6.476
95.833	6.477
104.545	6.477
115.000	6.478
127.778	6.478
766.667	6.479
876.190	6.479
1022.222	8.121
1226.667	19.050
1533.333	36.784
2044.444	57.073
3066.667	76.570
6133.333	93.074
7666.667	100.000

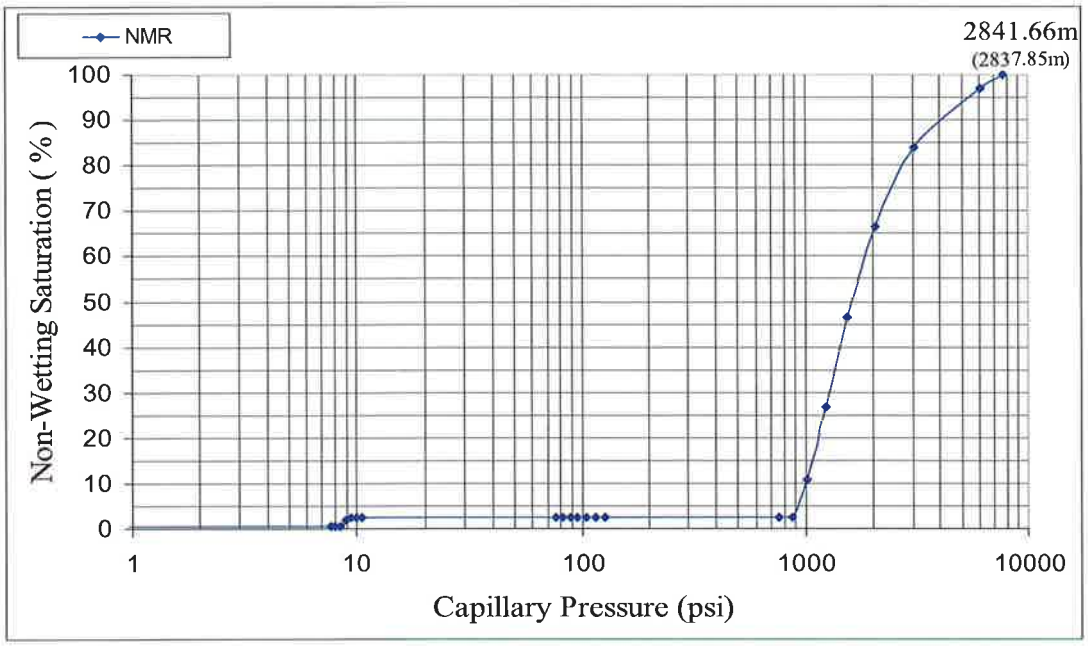

Capillary Pressure (psi)	Non-wetting Saturation (%)
0.767	0.000
0.794	0.557
0.823	0.558
0.855	0.558
0.889	0.559
0.926	0.559
0.967	0.560
7.667	0.561
8.032	0.561
8.433	0.562
8.877	1.965
9.370	2.549
9.922	2.549
10.542	2.550
76.667	2.550
82.143	2.551
88.462	2.552
95.833	2.552
104.545	2.553
115.000	2.553
127.778	2.554
766.667	2.554
876.190	2.555
1022.222	10.825
1226.667	26.772
1533.333	46.606
2044.444	66.600
3066.667	83.901
6133.333	96.884
7666.667	100.000

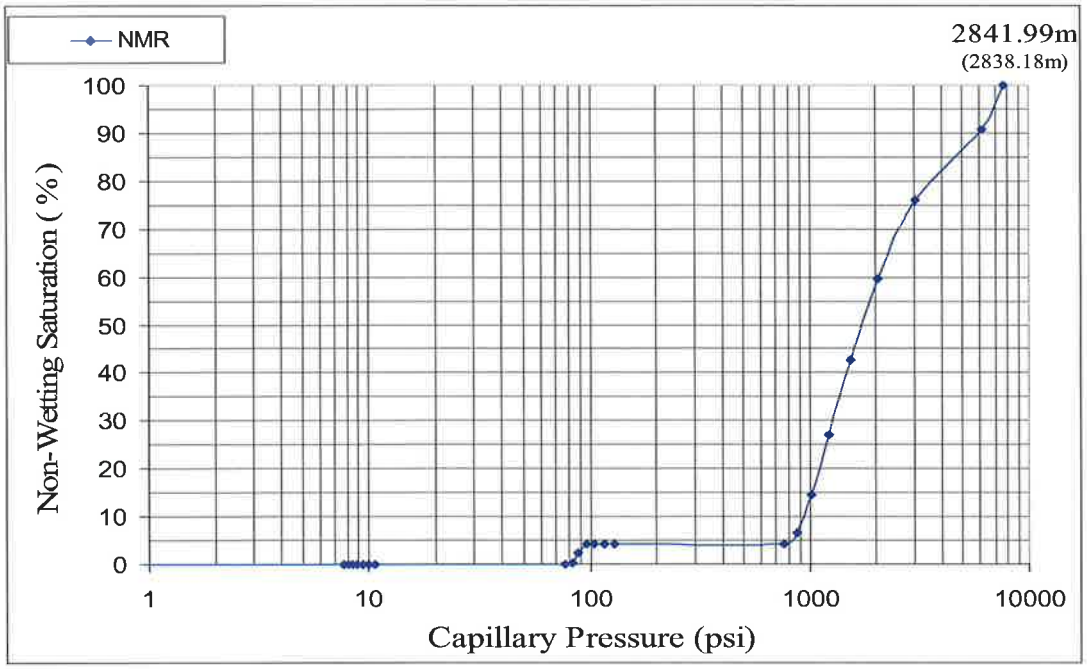

Capillary Pressure (psi)	Non-wetting Saturation (%)
0.767	0.000
0.794	0.074
0.823	0.074
0.855	0.075
0.889	0.075
0.926	0.076
0.967	0.076
7.667	0.076
8.032	0.077
8.433	0.077
8.877	0.077
9.370	0.078
9.922	0.084
10.542	0.084
76.667	0.085
82.143	0.156
88.462	2.273
95.833	4.286
104.545	4.287
115.000	4.287
127.778	4.287
766.667	4.288
876.190	6.581
1022.222	14.465
1226.667	27.081
1533.333	42.713
2044.444	59.518
3066.667	75.926
6133.333	90.772
7666.667	100.000

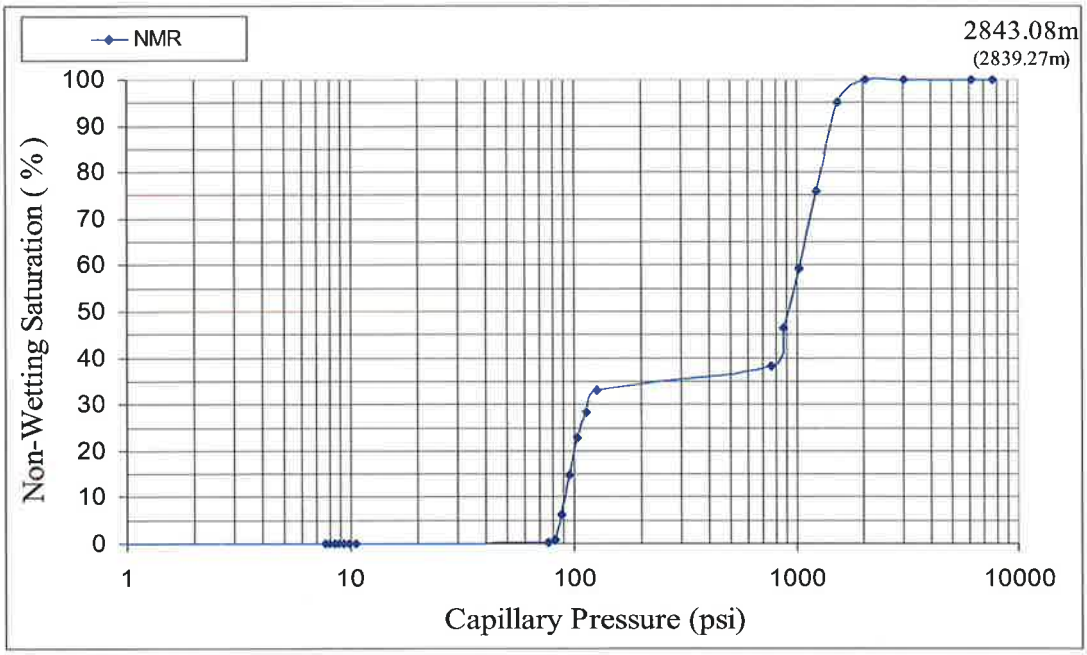

Capillary Pressure (psi)	Non-wetting Saturation (%)
0.767	0.000
0.794	0.001
0.823	0.002
0.855	0.003
0.889	0.004
0.926	0.005
0.967	0.006
7.667	0.007
8.032	0.008
8.433	0.009
8.877	0.010
9.370	0.012
9.922	0.013
10.542	0.085
76.667	0.167
82.143	0.724
88.462	6.221
95.833	14.867
104.545	22.847
115.000	28.471
127.778	32.966
766.667	38.256
876.190	46.529
1022.222	59.251
1226.667	75.909
1533.333	95.201
2044.444	100.000
3066.667	100.000
6133.333	100.000
7666.667	100.000

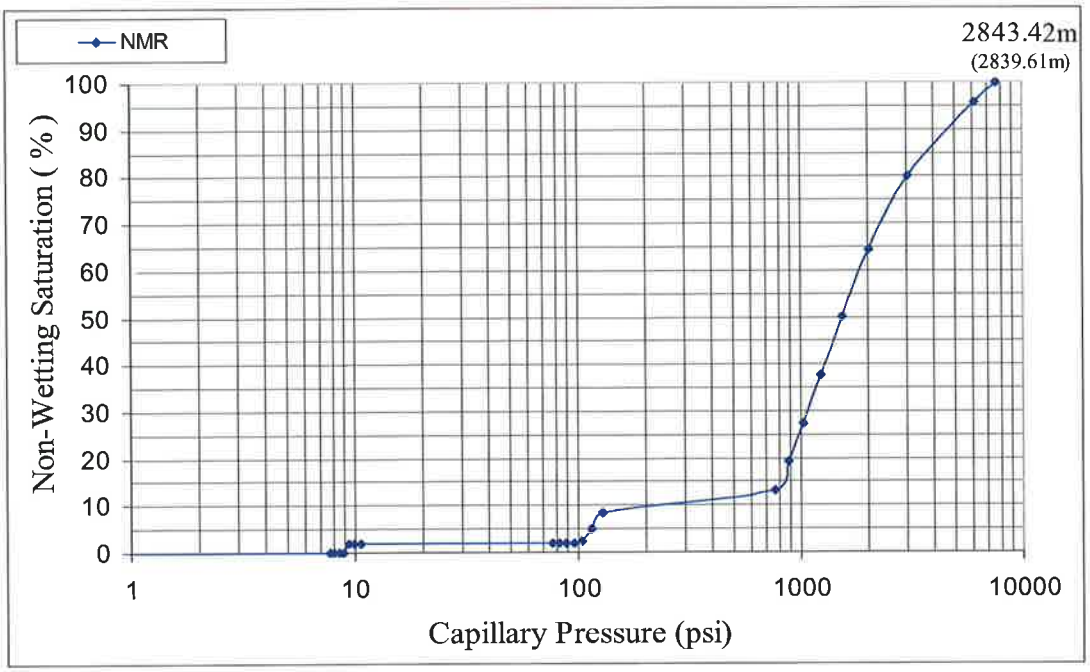

Capillary Pressure (psi)	Non-wetting Saturation (%)
0.767	0.000
0.794	0.000
0.823	0.001
0.855	0.001
0.889	0.002
0.926	0.002
0.967	0.003
7.667	0.003
8.032	0.004
8.433	0.004
8.877	0.005
9.370	1.868
9.922	1.950
10.542	1.950
76.667	1.951
82.143	1.951
88.462	1.952
95.833	2.017
104.545	2.591
115.000	5.024
127.778	8.539
766.667	13.195
876.190	19.385
1022.222	27.485
1226.667	37.719
1533.333	50.107
2044.444	64.398
3066.667	79.993
6133.333	95.922
7666.667	100.000

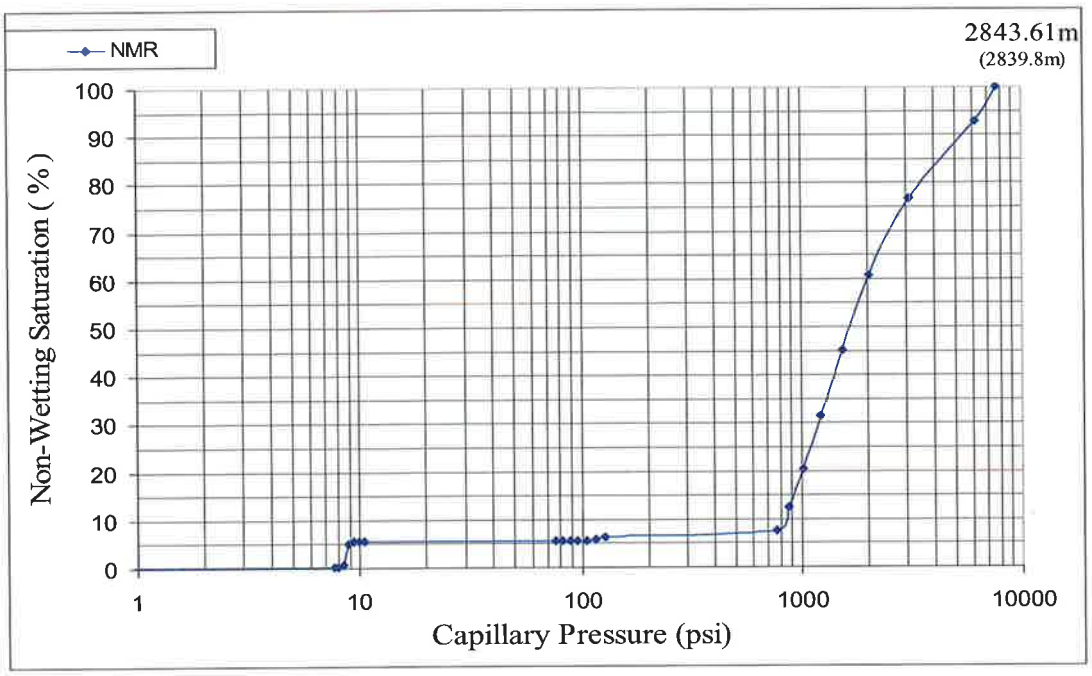

Capillary Pressure (psi)	Non-wetting Saturation (%)
0.767	0.000
0.794	0.306
0.823	0.306
0.855	0.307
0.889	0.307
0.926	0.308
0.967	0.308
7.667	0.309
8.032	0.309
8.433	0.686
8.877	5.128
9.370	5.581
9.922	5.581
10.542	5.582
76.667	5.582
82.143	5.583
88.462	5.583
95.833	5.584
104.545	5.584
115.000	5.848
127.778	6.275
766.667	7.577
876.190	12.397
1022.222	20.504
1226.667	31.587
1533.333	45.183
2044.444	60.613
3066.667	76.902
6133.333	92.814
7666.667	100.000

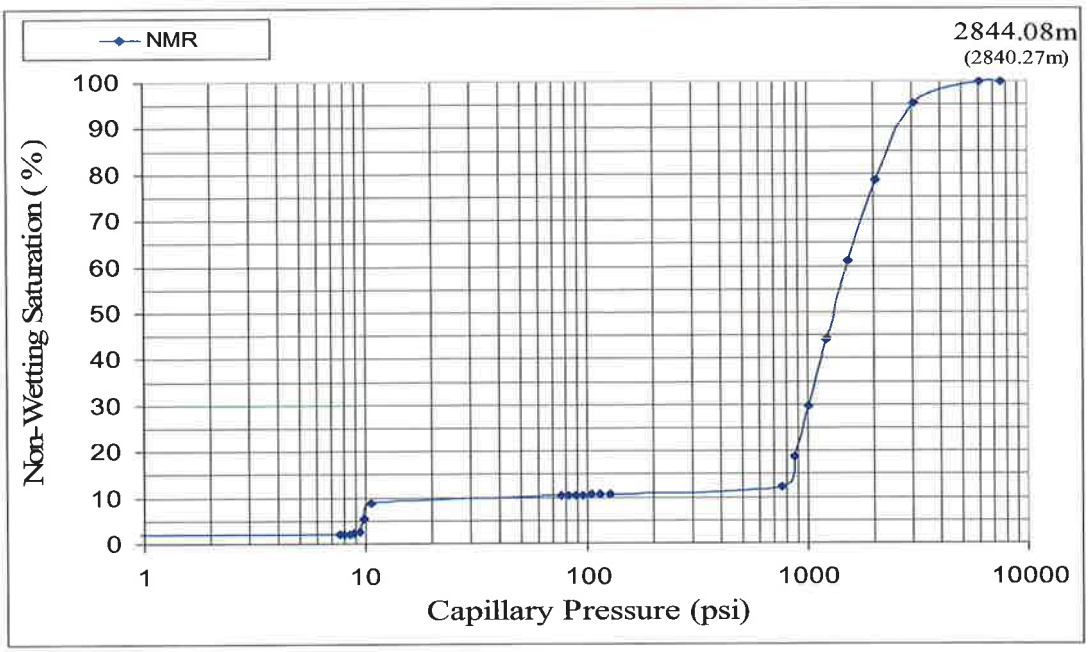

Capillary Pressure (psi)	Non-wetting Saturation (%)
0.767	0.000
0.794	1.102
0.823	1.820
0.855	1.976
0.889	1.976
0.926	1.977
0.967	1.978
7.667	1.978
8.032	1.979
8.433	1.979
8.877	2.254
9.370	2.676
9.922	5.540
10.542	8.847
76.667	10.409
82.143	10.410
88.462	10.441
95.833	10.529
104.545	10.595
115.000	10.637
127.778	10.754
766.667	12.349
876.190	18.728
1022.222	29.666
1226.667	44.250
1533.333	61.116
2044.444	78.690
3066.667	95.345
6133.333	100.000
7666.667	100.000

APPENDIX – C

XRD Analysis Results

Redman-1 XRD Bulk Analysis Results										
core-depth	log-depth	Quartz	Albite	Orthoclase	Mica	Chlorite	Smectite	Kaolin	Calcite	Pyrite
2833.76	2837.57	9	17	2	26	8	32	7	-	-
2836.85	2840.66	24	32	3	10	7	16	6	2	-
2837.05	2840.86	19	29	4	12	8	22	5	-	-
2837.4	2841.21	32	28	3	11	7	8	11	-	-
2837.49	2841.3	24	20	2	22	9	18	4	-	-
2837.85	2841.66	26	20	3	21	8	16	5	-	-
2838.18	2841.99	22	20	3	22	9	20	4	-	-
2839.27	2843.08	24	23	3	21	7	17	4	-	-
2839.61	2843.42	23	22	3	21	8	19	4	-	-
2839.8	2843.61	20	18	2	24	9	22	3	-	1
2840.27	2844.08	15	27	3	16	7	29	2	-	-

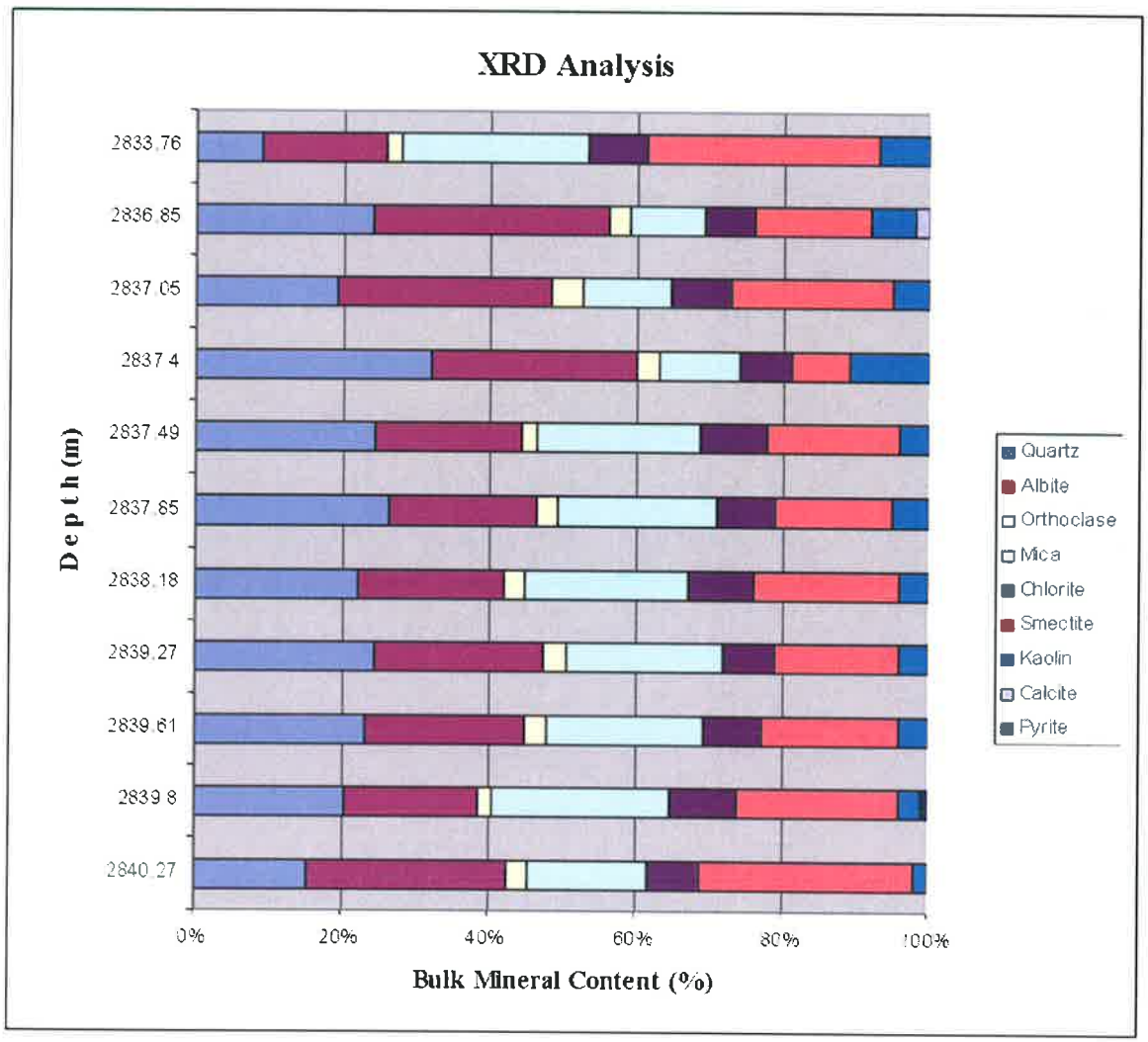

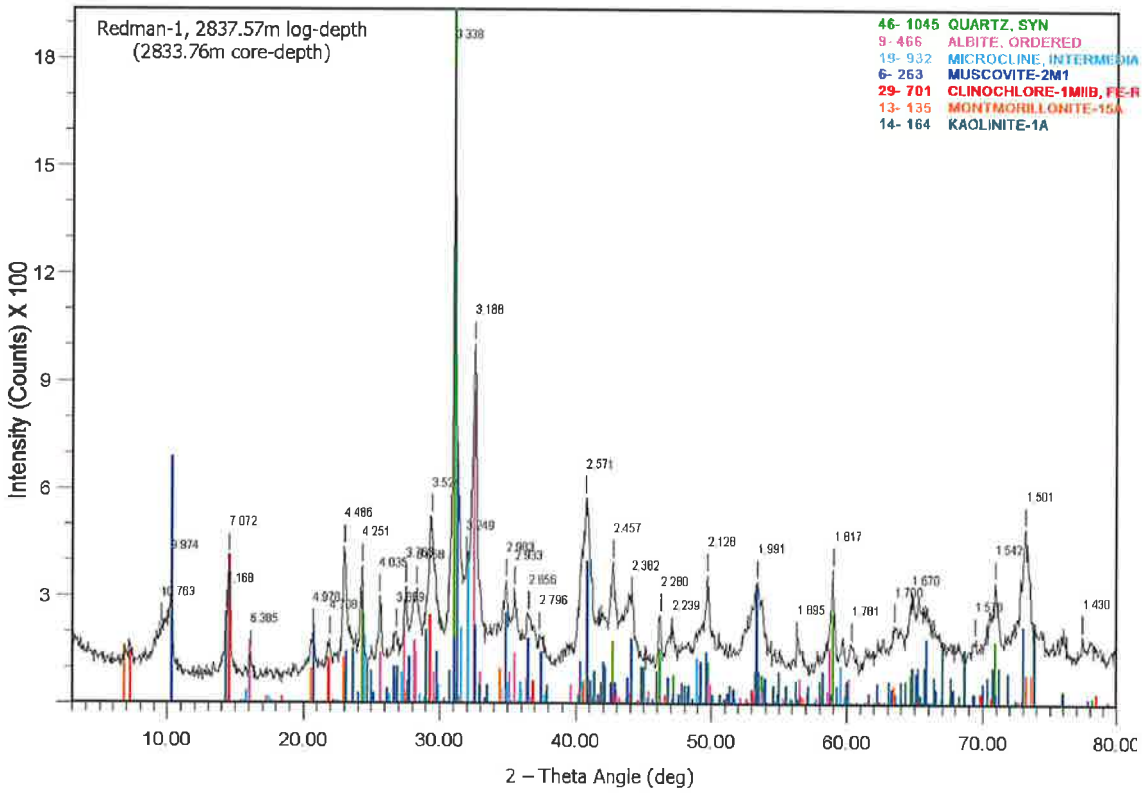
Redman-1, 2837.57m log-depth
(2833.76m core-depth)
46- 1045 QUARTZ, SYN
9- 466 ALBITE, ORDERED
19- 932 MICROCLINE, INTERMEDIA
6- 263 MUSCOVITE-2M1
29- 701 CLINOCHLORE-1MIIB, FE-R
13- 135 MONTMORILLONITE-15A
14- 164 KAOLINITE-1A
Intensity (Counts) X 100
2 – Theta Angle (deg)

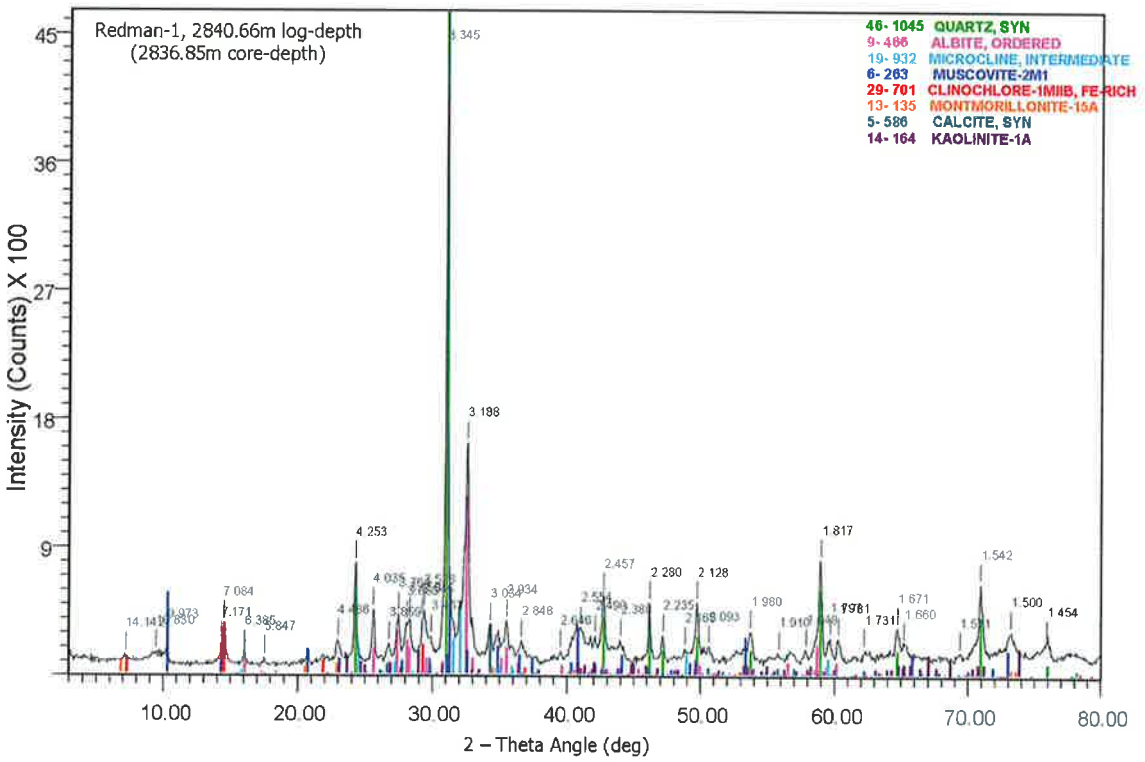
Redman-1, 2840.66m log-depth
(2836.85m core-depth)
46- 1045 QUARTZ, SYN
9- 466 ALBITE, ORDERED
19- 932 MICROCLINE, INTERMEDATE
6- 263 MUSCOVITE-2M1
29- 701 CLINOCHLORE-1MIIB, FE-RICH
13- 135 MONTMORILLONITE-15A
5- 586 CALCITE, SYN
14- 164 KAOLINITE-1A
Intensity (Counts) X 100
2 – Theta Angle (deg)

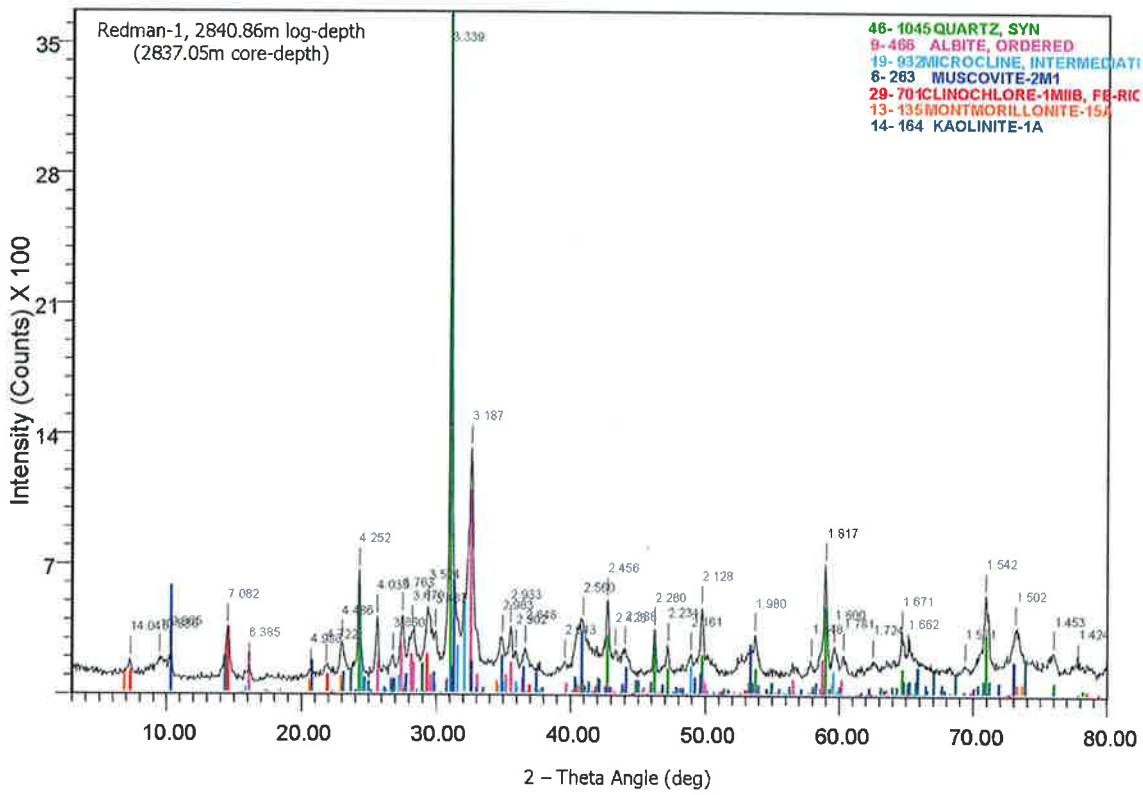
Redman-1, 2840.86m log-depth
(2837.05m core-depth)
46- 1045 QUARTZ, SYN
9- 466 ALBITE, ORDERED
19- 932 MICROCLINE, INTERMEDIATI
6- 263 MUSCOVITE-2M1
29- 701 CLINOCHLORE-1MIIB, FE-RIC
13- 135 MONTMORILLONITE-15A
14- 164 KAOLINITE-1A
Intensity (Counts) X 100
2 – Theta Angle (deg)

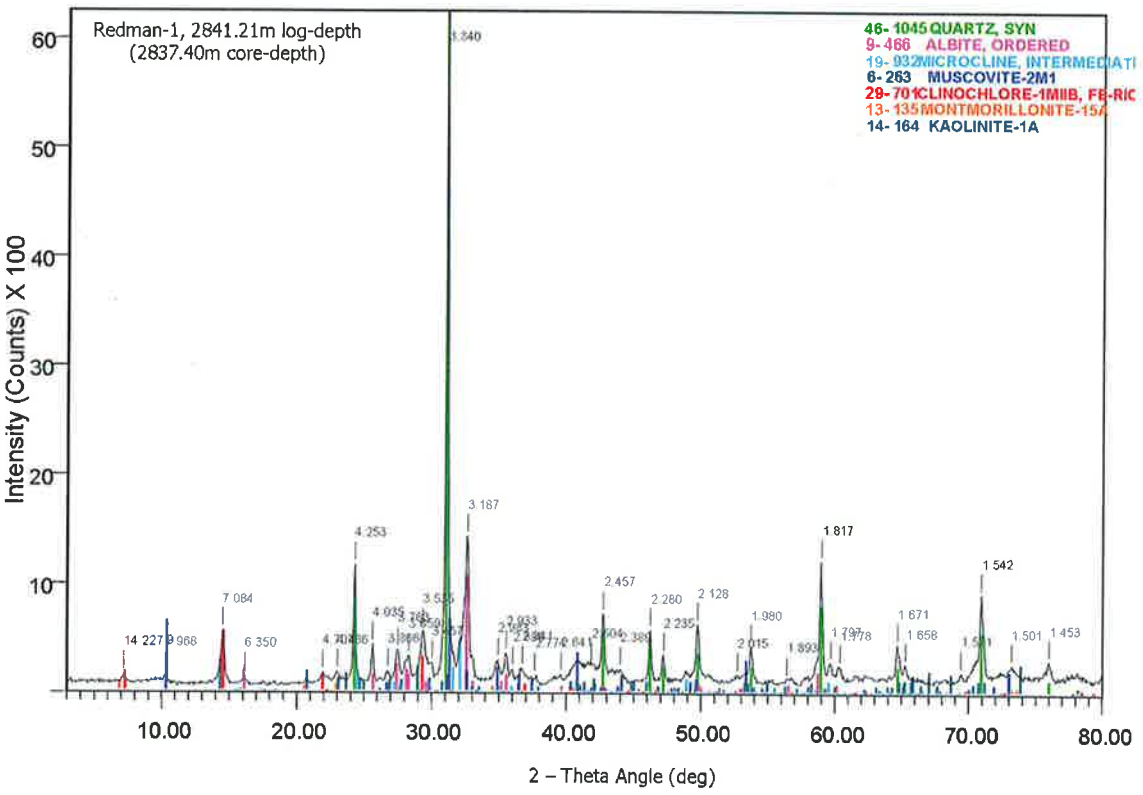
Redman-1, 2841.21m log-depth
(2837.40m core-depth)
46- 1045 QUARTZ, SYN
9- 466 ALBITE, ORDERED
19- 932 MICROCLINE, INTERMEDIATI
6- 263 MUSCOVITE-2M1
29- 701 CLINOCHLORE-1MIIB, FE-RIC
13- 135 MONTMORILLONITE-15A
14- 164 KAOLINITE-1A
Intensity (Counts) X 100
2 – Theta Angle (deg)

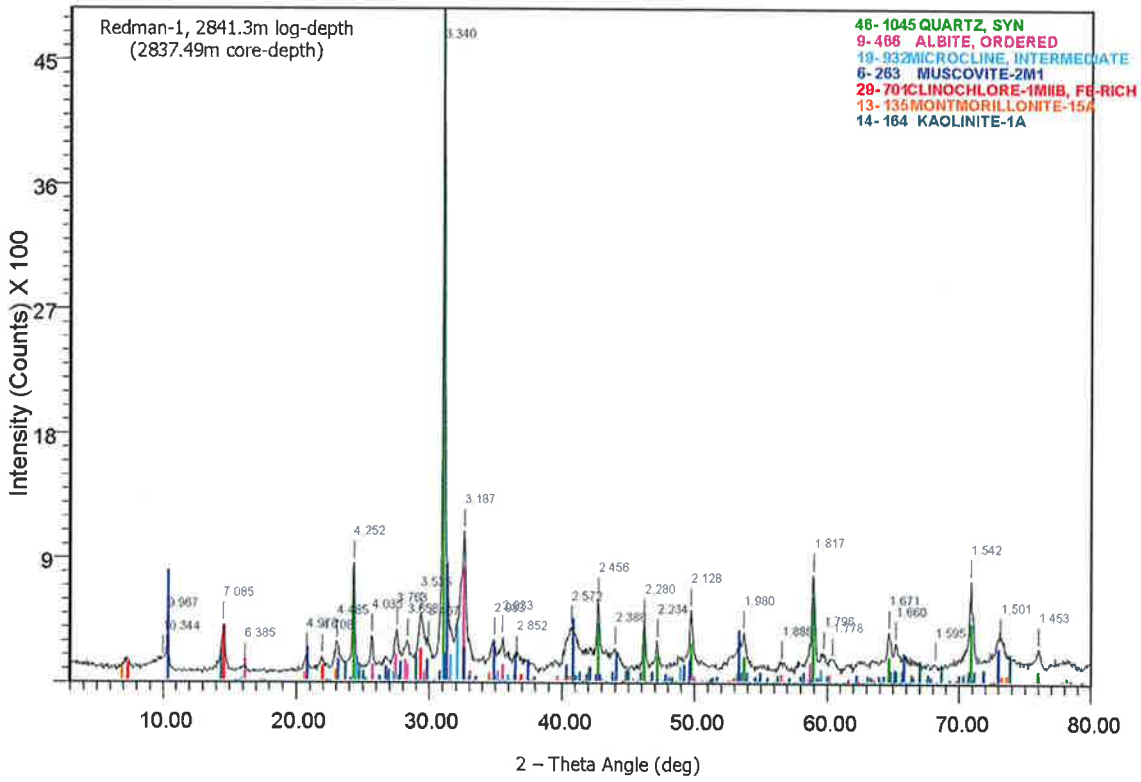
Redman-1, 2841.3m log-depth
(2837.49m core-depth)
46-1045 QUARTZ, SYN
9-466 ALBITE, ORDERED
19-932 MICROCLINE, INTERMEDIATE
6-263 MUSCOVITE-2M1
29-701 CLINOCHLORE-1MIIB, FE-RICH
13-135 MONTMORILLONITE-15A
14-164 KAOLINITE-1A
Intensity (Counts) X 100
2 – Theta Angle (deg)

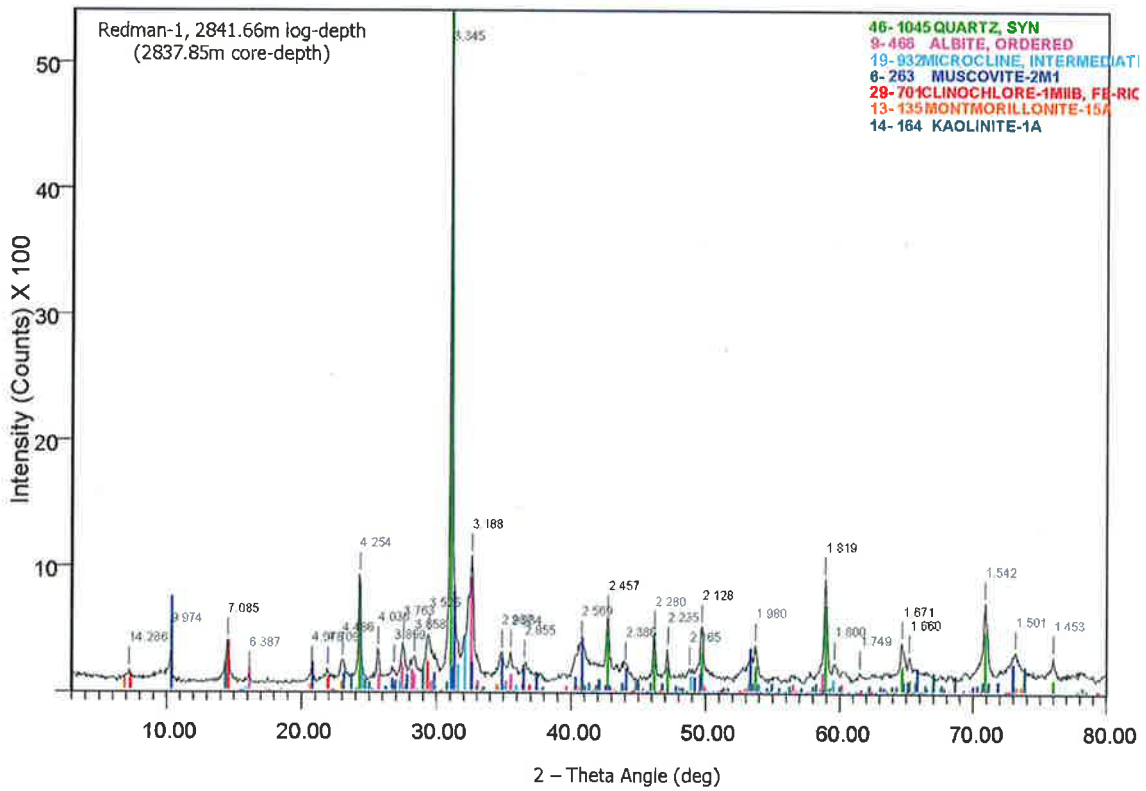
Redman-1, 2841.66m log-depth
(2837.85m core-depth)
46-1045 QUARTZ, SYN
9-466 ALBITE, ORDERED
19-932 MICROCLINE, INTERMEDIATE
6-263 MUSCOVITE-2M1
29-701 CLINOCHLORE-1MIIB, FE-RICH
13-135 MONTMORILLONITE-15A
14-164 KAOLINITE-1A
Intensity (Counts) X 100
2 – Theta Angle (deg)

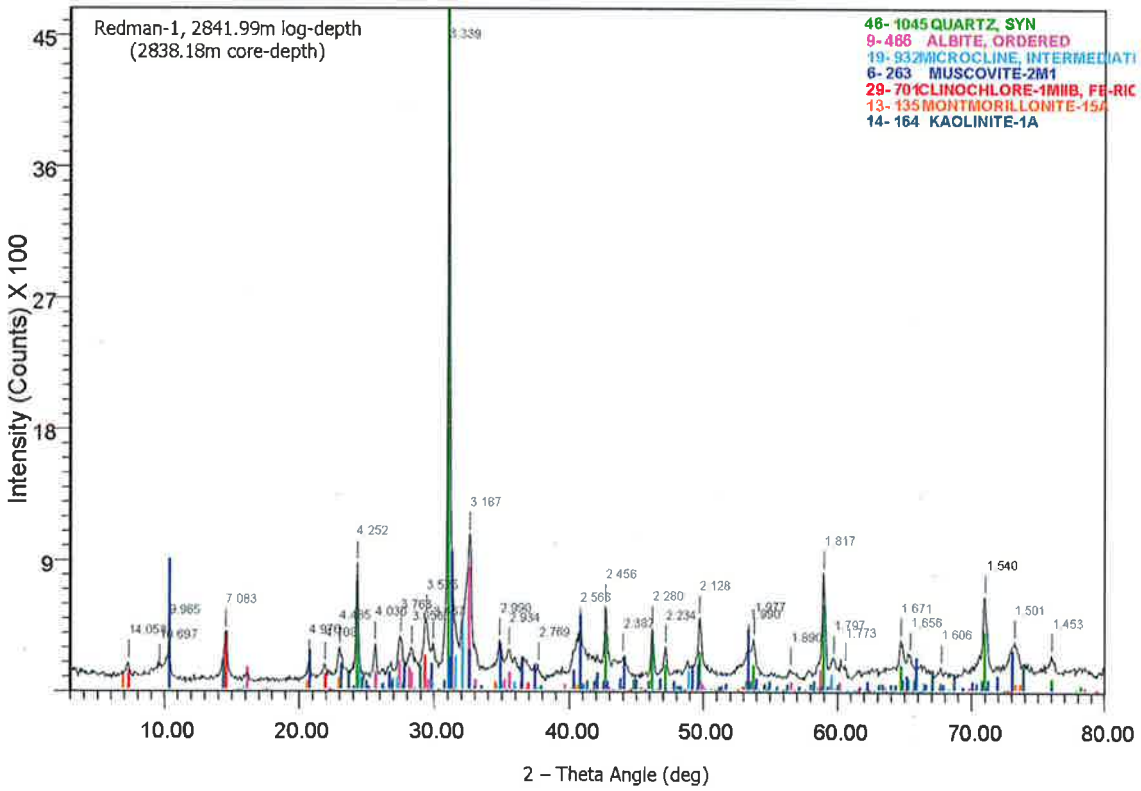
Redman-1, 2841.99m log-depth
(2838.18m core-depth)
46-1045 QUARTZ, SYN
9-466 ALBITE, ORDERED
19-932 MICROCLINE, INTERMEDIATE
6-263 MUSCOVITE-2M1
29-701 CLINOCHLORE-1MIIB, FE-RICH
13-135 MONTMORILLONITE-15A
14-164 KAOLINITE-1A
Intensity (Counts) X 100
2 – Theta Angle (deg)

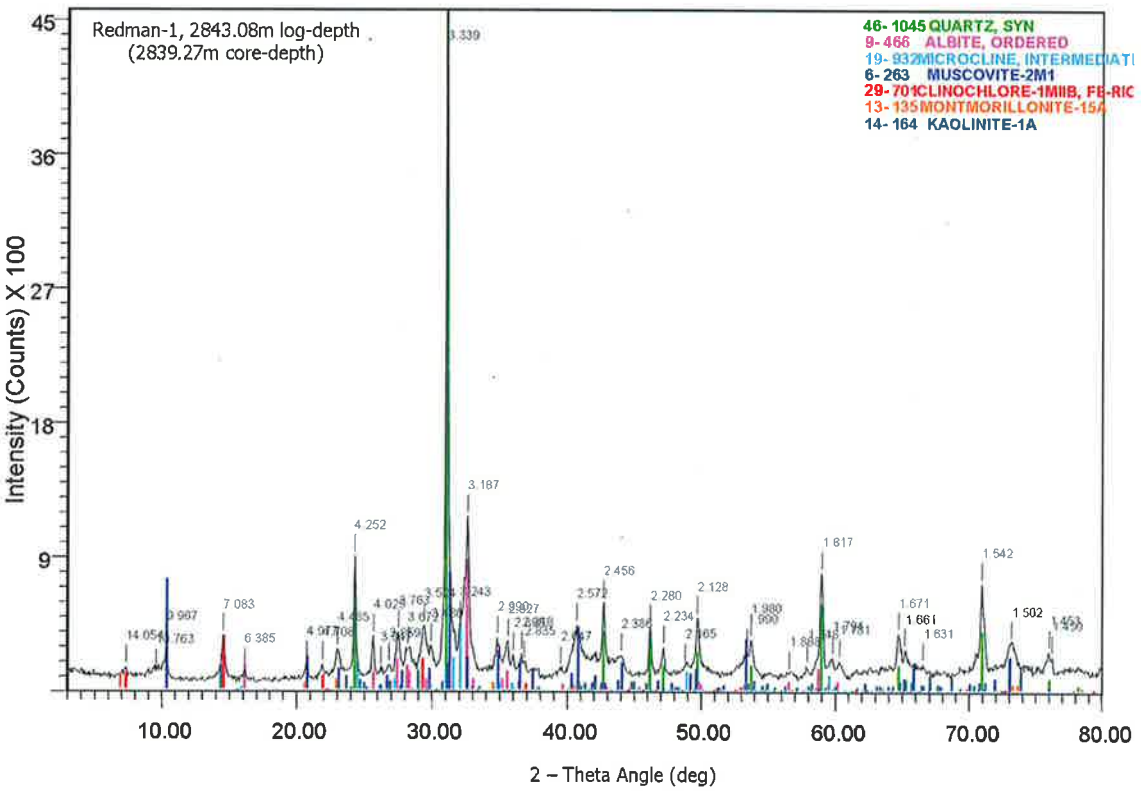
Redman-1, 2843.08m log-depth
(2839.27m core-depth)
46-1045 QUARTZ, SYN
9-466 ALBITE, ORDERED
19-932 MICROCLINE, INTERMEDIATE
6-263 MUSCOVITE-2M1
29-701 CLINOCHLORE-1MIIB, FE-RICH
13-135 MONTMORILLONITE-15A
14-164 KAOLINITE-1A
Intensity (Counts) X 100
2 – Theta Angle (deg)

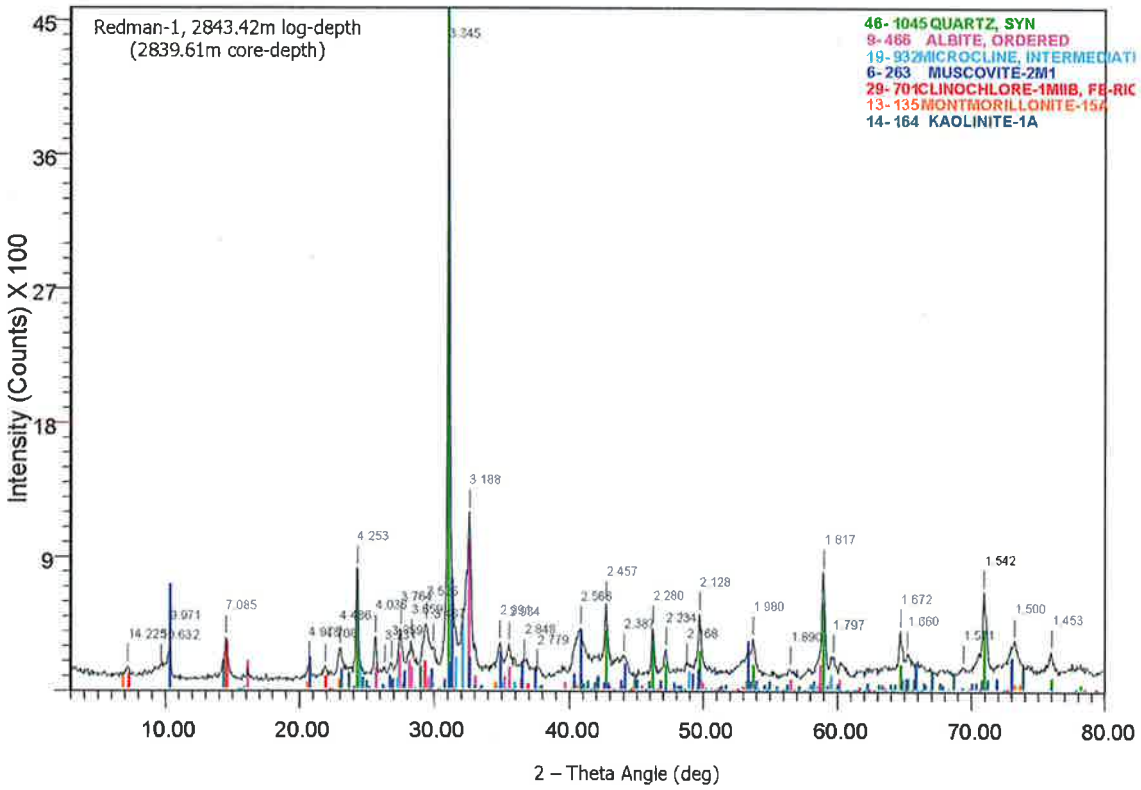
Redman-1, 2843.42m log-depth
(2839.61m core-depth)
46-1045 QUARTZ, SYN
9-466 ALBITE, ORDERED
19-932 MICROCLINE, INTERMEDIATI
6-263 MUSCOVITE-2M1
29-701 CLINOCHLORE-1MIIB, FE-RIC
13-135 MONTMORILLONITE-15A
14-164 KAOLINITE-1A
Intensity (Counts) X 100
2 – Theta Angle (deg)

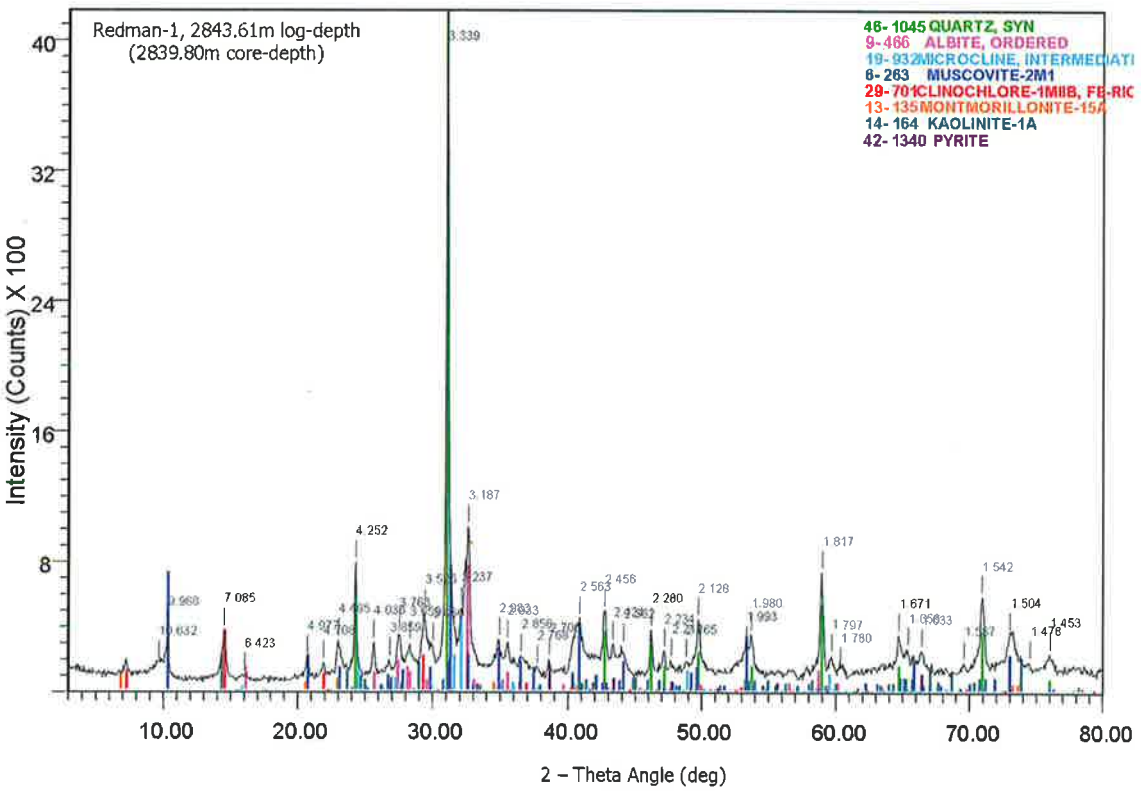
Redman-1, 2843.61m log-depth
(2839.80m core-depth)
46-1045 QUARTZ, SYN
9-466 ALBITE, ORDERED
19-932 MICROCLINE, INTERMEDIATI
6-263 MUSCOVITE-2M1
29-701 CLINOCHLORE-1MIIB, FE-RIC
13-135 MONTMORILLONITE-15A
14-164 KAOLINITE-1A
42-1340 PYRITE
Intensity (Counts) X 100
2 – Theta Angle (deg)

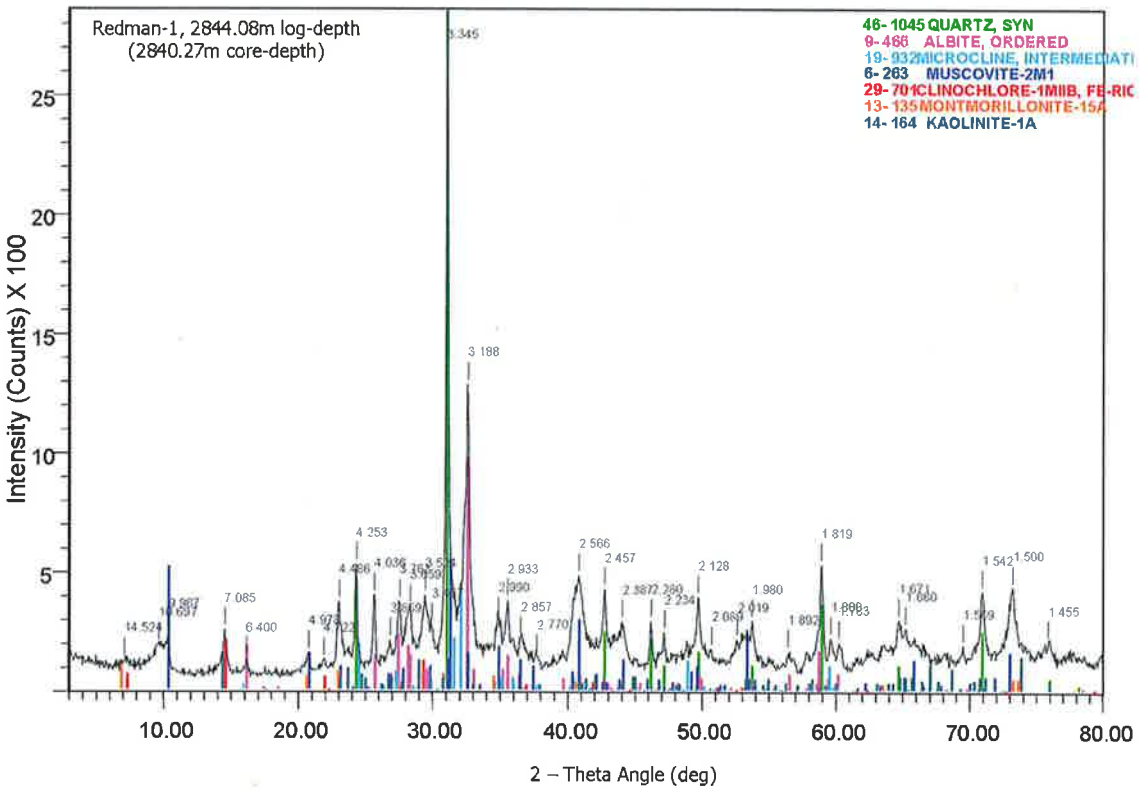
Redman-1, 2844.08m log-depth
(2840.27m core-depth)
46-1045 QUARTZ, SYN
9-466 ALBITE, ORDERED
19-932 MICROCLINE, INTERMEDIATE
6-263 MUSCOVITE-2M1
29-701 CLINOCHLORE-1MIIB, FE-RICH
13-135 MONTMORILLONITE-15A
14-164 KAOLINITE-1A
Intensity (Counts) X 100
2 – Theta Angle (deg)
10.00
20.00
30.00
40.00
50.00
60.00
70.00
80.00
5
10
15
20
25
3.345
3.188
4.253
7.085
6.400
14.524
2.933
2.857
2.770
2.566
2.457
2.128
1.980
1.819
1.542
1.500
1.455

APPENDIX – D

XRF Analysis, Point Counting & Porosity and Permeability Results

Redman-1 XRF Results for Main Minerals in Fine Grained Rock Samples												
Core-Depth	Log-Depth	SiO2	Al2O3	MgO	Fe2O3	CaO	Na2O	K2O	TiO2	P2O5	MnO	SO3
m	m	%	%	%	%	%	%	%	%	%	%	%
2833.76	2837.57	53.27	22.75	2.38	6.60	0.76	2.00	4.93	1.40	0.17	0.07	0.04
2836.85	2840.66	63.81	17.80	1.54	5.45	1.01	3.30	3.26	0.82	0.13	0.06	0.06
2837.05	2840.86	61.62	19.05	1.77	5.65	0.86	2.97	3.77	0.89	0.13	0.06	0.07
2837.40	2841.21	65.40	15.62	1.68	7.16	0.72	2.65	2.82	0.80	0.13	0.08	0.06
2837.49	2841.30	62.24	17.70	1.92	6.09	0.92	2.07	3.84	0.93	0.12	0.06	0.06
2837.85	2841.66	63.35	17.31	1.81	5.83	0.92	2.09	3.84	0.93	0.13	0.06	0.06
2838.18	2841.99	62.21	17.88	1.79	5.67	1.06	2.02	4.06	0.97	0.14	0.06	0.10
2839.27	2843.08	62.93	17.55	1.78	5.57	0.80	2.30	3.95	0.94	0.14	0.06	0.08
2839.61	2843.42	62.85	17.79	1.84	5.94	0.86	2.28	3.96	0.91	0.14	0.07	0.08
2839.80	2843.61	60.51	18.68	1.98	5.98	0.98	1.92	4.24	1.01	0.14	0.06	0.23
2840.27	2844.08	62.54	17.98	1.73	5.21	0.69	2.67	3.85	1.02	0.13	0.06	0.07

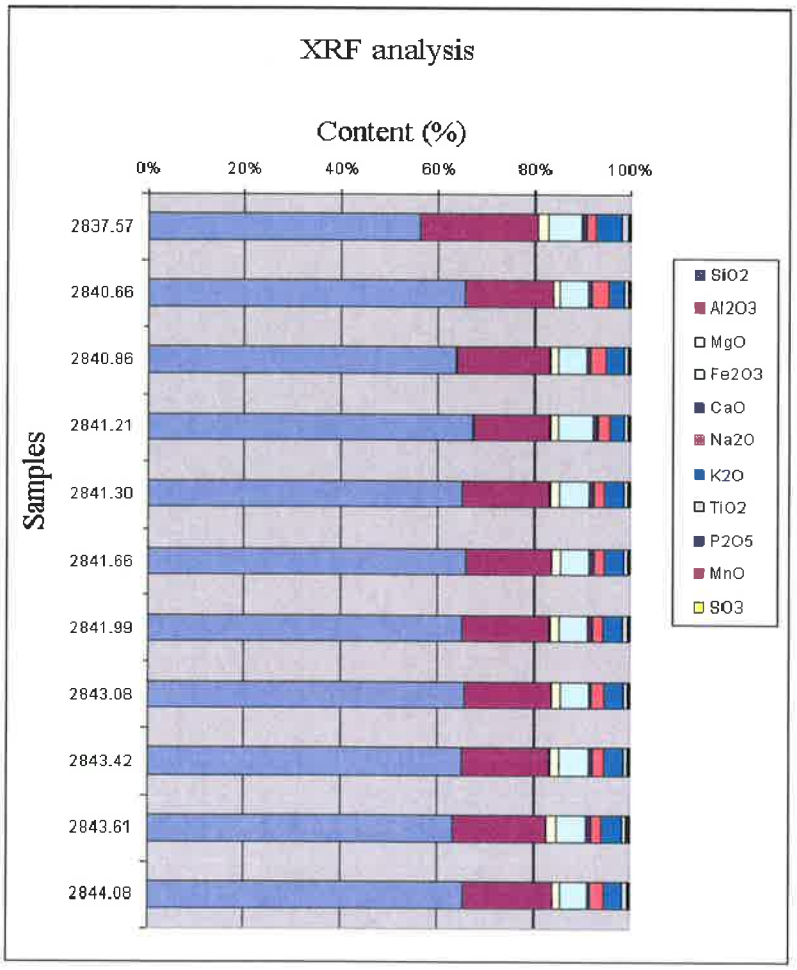

Point Counting Results for Sample 2840.86m (log-depth)			
Type No.	Mineral Types	Total No.	Percentage %
1	Quartz	62	20.67
2	Albite	69	23.00
3	Orthoclase	7	2.33
4	Biotite	36	12.00
5	Muscovite	10	3.33
6	Rock Fragments	37	12.33
7	Organic Matter	8	2.67
8	Clorite	15	5.00
9	Smectite	56	18.67
	Total =	300	

Point Counting Results for Sample 2841.99m (log-depth)			
Type No.	Mineral Types	Total No.	Percentage %
1	Quartz	56	18.67
2	Albite	64	21.33
3	Orthoclase	8	2.67
4	Biotite	33	11.00
5	Muscovite	19	6.33
6	Rock Fragments	13	4.33
7	Organic Matter	11	3.67
8	Clorite	23	7.67
9	Smectite	73	24.33
	Total =	300	

Point Counting Results for Sample 2844.08m (log-depth)			
Type No.	Mineral Types	Total No.	Percentage %
1	Quartz	59	19.67
2	Albite	41	13.67
3	Orthoclase	13	4.33
4	Biotite	22	7.33
5	Muscovite	14	4.67
6	Rock Fragments	13	4.33
7	Organic Matter	7	2.33
8	Clorite	14	4.67
9	Smectite	117	39.00
	Total =	300	

Porosity Results of Laboratory Measurement								
Well Name:	Redman # 1							
Recalibrate	P1	799.8	P2	433.1	V1 (Calc)	131.86696		
Sample No	Core-Depth	Log-Depth	P1	P2	Bulk Volume (cc)	Weight (g)	V3 (Calc)	Porosity (%)
1	2836.85	2840.66	799.8	564.5	58.90	149.54	54.97	3.76
2	2837.05	2840.86	799.9	565.8	58.20	149.08	54.56	1.91
3	2837.4	2841.21	799.8	518	41.86	106.21	71.74	4.66
4	2837.49	2841.3	800.2	558.4	54.80	142.24	57.10	0.46
5	2837.85	2841.66	800	573.7	60.18	155.27	52.02	0.91
Recalibrate	P1		800.5	P2	433.70	V1 (Calc)	132.01	
6	2838.18	2841.99	800.2	566.5	58.06	149.13	54.46	1.49
7	2839.61	2843.42	800.1	509.7	36.77	94.89	75.21	0.91
8	2839.8	2843.61	800.4	538.4	48.03	123.58	64.24	1.29
9	2840.27	2844.08	800.2	560	55.98	143.82	56.62	1.70

Permeability Results of Laboratory Measurement									
Well Name:	Redman # 1								
Sample No	Core-Depth	Log-Depth	Gauge Press	Plug Length	Plug Bulk	Air Viscosity	Qb (cc/s)	Permeability Ka (mD)	Klinkenberg Kl (mD)
	(m)	(m)	(Atm)	(cm)	Vol (cc)	(cp)			
1	2836.85	2840.66	5	51.12	58.90	0.018	0.22	35.49	29.90
2	2837.05	2840.86	5	51.96	58.20	0.018	1.25	210.83	197.64
3	2837.4	2841.21	5	37.31	41.86	0.018	0.418	50.54	43.49
4	2837.49	2841.3	5	53.78	54.80	0.018	1.09	209.18	196.00
5	2837.85	2841.66	1	51.92	60.18	0.018	0.21	171.02	158.32
6	2838.18	2841.99	1	50.61	58.06	0.018	0.15	120.31	109.05
7	2839.61	2843.42	5	36.13	36.77	0.018	0.38	49.05	42.13
8	2839.8	2843.61	1	47.38	48.03	0.018	0.59	501.33	495.04
9	2840.27	2844.08	5	50.53	55.98	0.018	0.12	19.90	16.19